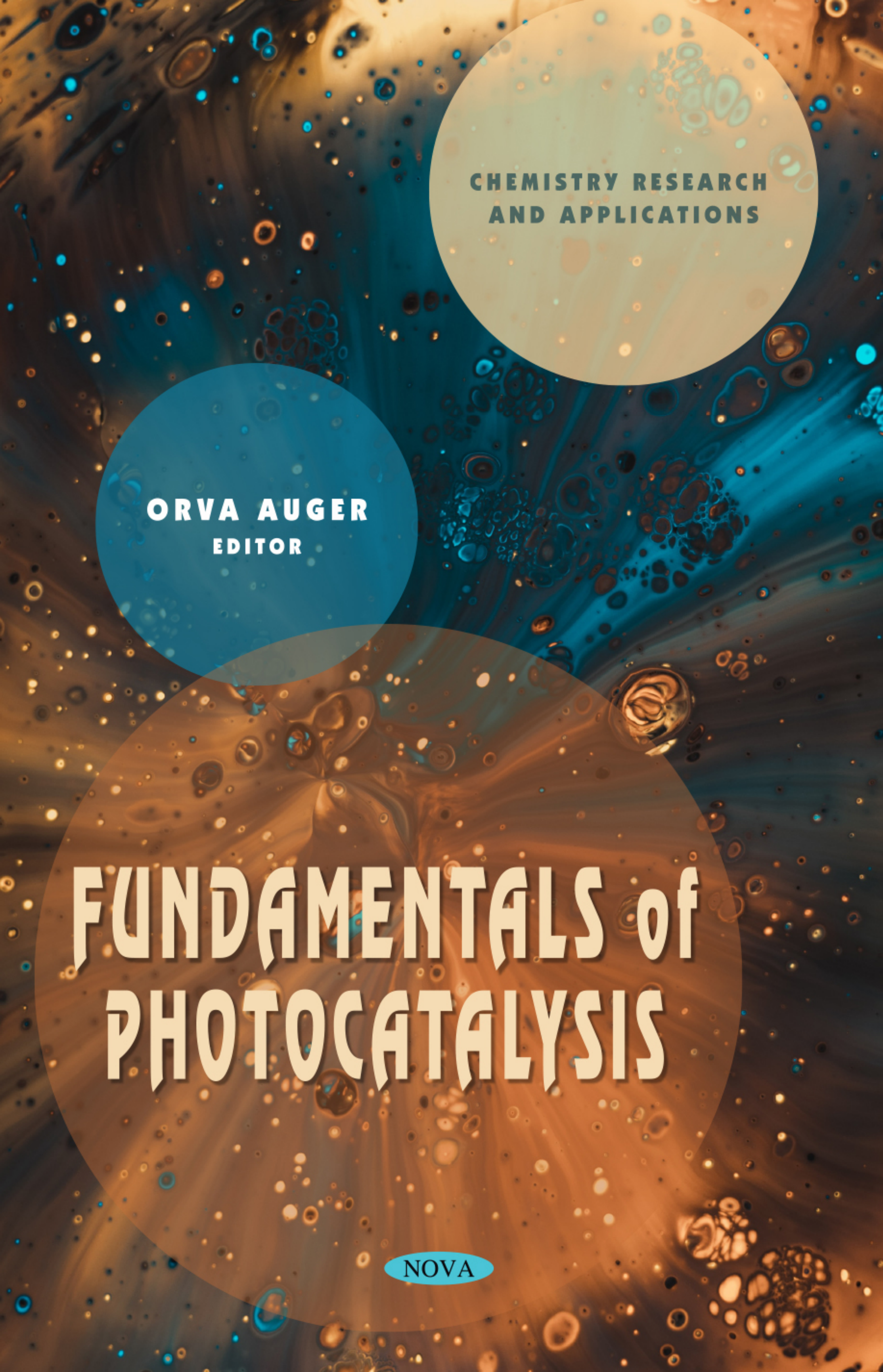

CHEMISTRY RESEARCH AND APPLICATIONS

ORVA AUGER
EDITOR

FUNDAMENTALS of PHOTOCATALYSIS

NOVA

CHEMISTRY RESEARCH AND APPLICATIONS

FUNDAMENTALS OF PHOTOCATALYSIS

CHEMISTRY RESEARCH AND APPLICATIONS

Additional books and e-books in this series can be found on Nova's website under the Series tab.

CHEMISTRY RESEARCH AND APPLICATIONS

FUNDAMENTALS OF PHOTOCATALYSIS

ORVA AUGER
EDITOR

nova
science publishers
New York

Copyright © 2022 by Nova Science Publishers, Inc.
DOI: https://doi.org/10.52305/FUZH8176

All rights reserved. No part of this book may be reproduced, stored in a retrieval system or transmitted in any form or by any means: electronic, electrostatic, magnetic, tape, mechanical photocopying, recording or otherwise without the written permission of the Publisher.

We have partnered with Copyright Clearance Center to make it easy for you to obtain permissions to reuse content from this publication. Simply navigate to this publication's page on Nova's website and locate the "Get Permission" button below the title description. This button is linked directly to the title's permission page on copyright.com. Alternatively, you can visit copyright.com and search by title, ISBN, or ISSN.

For further questions about using the service on copyright.com, please contact:
Copyright Clearance Center
Phone: +1-(978) 750-8400 Fax: +1-(978) 750-4470 E-mail: info@copyright.com.

NOTICE TO THE READER

The Publisher has taken reasonable care in the preparation of this book, but makes no expressed or implied warranty of any kind and assumes no responsibility for any errors or omissions. No liability is assumed for incidental or consequential damages in connection with or arising out of information contained in this book. The Publisher shall not be liable for any special, consequential, or exemplary damages resulting, in whole or in part, from the readers' use of, or reliance upon, this material. Any parts of this book based on government reports are so indicated and copyright is claimed for those parts to the extent applicable to compilations of such works.

Independent verification should be sought for any data, advice or recommendations contained in this book. In addition, no responsibility is assumed by the Publisher for any injury and/or damage to persons or property arising from any methods, products, instructions, ideas or otherwise contained in this publication.

This publication is designed to provide accurate and authoritative information with regard to the subject matter covered herein. It is sold with the clear understanding that the Publisher is not engaged in rendering legal or any other professional services. If legal or any other expert assistance is required, the services of a competent person should be sought. FROM A DECLARATION OF PARTICIPANTS JOINTLY ADOPTED BY A COMMITTEE OF THE AMERICAN BAR ASSOCIATION AND A COMMITTEE OF PUBLISHERS.

Additional color graphics may be available in the e-book version of this book.

Library of Congress Cataloging-in-Publication Data

ISBN: 978-1-68507-417-3 (e-book)

Published by Nova Science Publishers, Inc. † New York

Contents

PREFACE

In chemistry, photocatalysis refers to the acceleration of a photoreaction in the presence of a catalyst. Various aspects and applications of this process are described in the six chapters of this book. Chapter one addresses the reduction and oxidation of heavy metals by the photocatalytic process to produce less toxic forms, thus reducing pollution. Chapter two reviews some issues of photocatalytic reactions which may have been overlooked in other reports. Chapter three deals with the utilization of ZnO-CdO nanoblocks as adsorbent and efficient solar photocatalysts towards brilliant cresol blue degradation. Chapter four explains heterogeneous photocatalysis through the use of titanium and tungsten oxide nanostructures. Chapter five reports the fabrication and evaluation of TiO2 nanowires supported on graphene and sensitized with Ag in a unique hierarchical three-dimensional sandwich structure. Lastly, chapter six provides an overview of recent achievements in C-N bond formation reactions triggered by visible light-induced DDQ-photoredox catalysis.

Chapter 1 - Some potentially toxic elements are present in the environment in different states of oxidation, being their inorganic forms generally found in natural water. Thus, heavy metals contamination is currently considered a global problem, which stems from both natural and anthropogenic sources, such as wood industry, agricultural pesticides, mining and metallurgy activities. Drinking water contamination by heavy metals is even more alarming, given the harmful effects that it may cause to human health. In this context, the chapter aims to address the reduction/oxidation of heavy metals by the photocatalytic process, to produce less toxic forms to the environment. In particular, it will focus on the description of photocatalytic removal of elements such as selenium (Se), lead (Pb) and arsenic (As). In this context, parameters that influence the process will be described, e.g., photocatalyst type, pH, initial concentration of pollutant, radiation and additives. In addition, a topic on photoactivity in reuse will be addressed.

Chapter 2 - Some peculiar issues of photocatalytic reactions which may have been overlooked in many reports are reviewed. In the beginning, electron transfer (ET) initiated reactions at the solid surface, which is essential in photocatalysis, are classified to four types based on the extent of the interaction of the reactant with the solid surface. Those four ET reactions are reversible reactions, irreversible connected reactions, deposition, and dissolution. Most photocatalytic reactions are irreversible ET connected reactions and deposition of the products that strongly interact with the solid surface, while, in electrochemistry, reversible reaction for the reactants of weak interaction is mainly treated. Though the relationship between the reaction rate and the reaction energy has been discussed with the Marcus-Gerischer theory of electrochemistry, the acceptance of this theory for photocatalysis may cause difficulties because the frequency of the ET is limited by the photon absorption and the ET reaction rate is compete with the carrier recombination. Namely, the usage of the reorganization energy may need careful consideration for the kinetic analysis in semiconductor photocatalysis. The electric potential near the photocatalyst surface was visualized and it was realized that the potential gradient was localized near the surface holes, whereas it was expanded to the whole surface of the flat electrode in electrochemistry. Since the semiconductor photocatalysts are not wired to an electric source, the charges stored in the semiconductor particle can be evaluated. Then, a precise energy band position could be obtained and it may be different from the measurements by electrochemical methods, which was discussed in terms of the band alignments of anatase and rutile TiO_2 crystals. The analysis of the reaction kinetics for heterogeneous photocatalysis should be different from that for the homogeneous solution because a pair of the redox reactions take place in the same particle. Then, the novel method for applying the Langmuir-Hinshelwood equation was presented to describe the photocatalytic oxidation as a function of both the reactant concentration and the light intensity.

Chapter 3 - Here, ZnO-CdO nanoblocks (NBs) have been prepared by facile wet-chemical technique at low-temperature and characterized by UV–vis., FT-IR, XRD, FESEM, XPS, and XEDS etc. The NBs were used and applied for the selective detection of Fe(III) ions as an efficient adsorbent as well as active photo-catalytic degradation using Brilliant cresol blue (BCB). The detection efficiency of NBs phase was also investigated for a selective detection of Fe(III) by Inductively coupled plasma - optical emission spectrometry (ICP-OES). NBs were found the most selective towards Fe(III), where adsorption process was mainly monolayer on a homogeneous adsorbent surface. In photo-catalysis, almost 52.3% degradation with BCB dye was observed under solar irradiation with NBs.

Chapter 4 - Heterogeneous photocatalysis is well-known as an advanced oxidative process (POA's) due to its multiple applications, such as air purification, antibacterials, green energy, self-cleaning, water treatment and CO_2 reduction. Photocatalytic processes gained notoriety in 1972, with an innovative study by Fujishima and Honda. His work boosted the use of TiO_2 in photocatalytic processes. However, the wide bandgap (± 3.2 eV) of TiO_2 causes low efficiency to separate the charges and presents a low absorption capacity under solar irradiation. Doping or combining TiO_2 with metals or non-metals appears as an option to improve its photocatalytic performance as a semiconductor. The presence of the dopant adjusts the bandgap and the behaviour of the electron/hole pair what contributes to the better photocatalytic performance of TiO_2 when irradiated with sunlight in the UV-visible region. WO_3 is a transition metal widely used as a semiconductor and as a dopant due to its smaller bandgap, between 2.6-2.8 eV, which increases the radiation absorption capacity of this oxide in the visible region.

Chapter 5 - Graphene is of significance in photocatalysis because of its high electric charge carrier mobility and optical transparency, intrinsic large surface and capability of chemical functionalization. Increasing surface area is known to increase the photocatalytic efficiency. One dimension (1-D) TiO_2 nanowires (TNW) is of recent interest because the structure is less prone to agglomeration when compared to TiO_2 nanoparticles. The fabrication and evaluation of TNWs supported on graphene and sensitized with Ag in a unique hierarchical three-dimensional (3-D) sandwich structure is reported in this study. The Ag/TNW/graphene (Ag/TNWs/G) 3-D photocatalyst demonstrated that the surface plasmon resonance (SPR) effect caused by Ag nanoparticles resulted in strong and broad absorption bands for the photocatalyst over the ultraviolet and visible region. The TNWs and graphene in the 3-D Ag/TNWs/G composite increased the specific surface area (SSA) by a factor of approximately 5.4 when compared to commercial TiO_2 nanoparticles (P25). The high SSA contributed to increasing the adsorption of pollutants. The photocatalyst sandwich was able to decompose methylene blue (MB), a model pollutant, efficiently using visible-light. The MB degradation rate was approximately 32-fold greater than for P25 and approximately 2-fold greater than for TNWs/G. Coupling the characteristics of graphene with the SPR properties of Ag nanoparticles in the 3-D hierarchical sandwich could be a promising strategy for preparing other noble metal and carbon based TiO_2 nanotube composite photocatalysts for various application

Chapter 6 - In recent years, photoredox catalysis employing 2,3-dichloro-5,6-dicyano-1,4-benzoquinone (DDQ) has come to the limelight in organic chemistry as an effective strategy for the activation of small molecules. In a general sense, these approaches rely on the capacity of dyes to transform visible light into chemical energy by engaging in single-electron transfer processes with organic substrates. This chapter provides an overview of recent achievements in C-N bond formation reactions trigger by visible light-induced DDQ-photoredox catalysis, which mainly discusses proposed reactions mechanisms as well as substrate scope and limitations.

In: Fundamentals of Photocatalysis
Editor: Orva Auger
ISBN: 978-1-68507-374-9

Chapter 1

OXIDATION AND REDUCTION OF HEAVY METALS BY PHOTOCATALYTIC PROCESS

G. G. Lenzi[1,*], PhD, L. N. B. Almeida[2], PhD,
T. G. Josué[1], MD, M. E. K. Fuziki[2], PhD,
L. M. S. Colpini[3], PhD, R. Brackmann[4], PhD
and A. M. Tusset[5], PhD
[1]Departament of Chemical Engineering, Federal University of Technology Paraná, Ponta Grossa, Brazil
[2]Departament of Chemical Engineering, State University of Maringá, Maringá, Brazil
[3]Federal University of Paraná, Advanced Campus of Jandaia do Sul, Jandaia do Sul, Brazil
[4]Departament of Chemical, Federal University of Technology Paraná, Pato Branco, Brazil
[5]Departament of Engineering, Federal University of Technology Paraná, Ponta Grossa, Brazil

---

[*] Corresponding Author's E-mail: gianeg@utfpr.edu.br.

ABSTRACT

Some potentially toxic elements are present in the environment in different states of oxidation, being their inorganic forms generally found in natural water. Thus, heavy metals contamination is currently considered a global problem, which stems from both natural and anthropogenic sources, such as wood industry, agricultural pesticides, mining and metallurgy activities. Drinking water contamination by heavy metals is even more alarming, given the harmful effects that it may cause to human health. In this context, the chapter aims to address the reduction/oxidation of heavy metals by the photocatalytic process, to produce less toxic forms to the environment. In particular, it will focus on the description of photocatalytic removal of elements such as selenium (Se), lead (Pb) and arsenic (As). In this context, parameters that influence the process will be described, e.g., photocatalyst type, pH, initial concentration of pollutant, radiation and additives. In addition, a topic on photoactivity in reuse will be addressed.

Keywords: heterogeneous photocatalysis, photocatalysts reuse, water treatment

INTRODUCTION

The human life quality is directly dependent water resources, with regard to their availability and quality of water. In this sense, actions that promote better management, preservation and quality control of these resources are extremely important. The presence of potentially toxic substances in water intended for human consumption is responsible for a series of serious diseases, which can reach high mortality rates. In this context, it is necessary to establish maximum parameters for the concentration of various compounds, being essential the quality control so that the resources destined for human consumption meet the established limits. However, many of the compounds potentially toxic to human health cannot be efficiently removed by conventional treatments, normally used in water treatment plants. In most cases, these compounds are present in low concentrations, however, due to their potential toxicity, the legislation establishes that the maximum limit is even lower, making it necessary to remove them so that the water can be used.

However, the removal of elements such as selenium (Se), lead (Pb), barium (Ba) and arsenic (As) is not a simple task and generally, due to the established limits, they require sophisticated and costly removal processes, which often results in the unfeasibility of the treatment. Thus, alternative systems, which reduce cost and enable the efficient removal of potentially toxic elements from water, allowing their safe use for human consumption, are being widely studied. Alternative treatments to remove these contaminants can effectively increase the availability of water resources. Simple and low-cost water treatment systems can be easily used, both small and large plants, facilitating access to drinking water in different regions of the world. In this context, heterogeneous photocatalysis has gained ground as a technology that allows removing or at least converting these elements into less toxic forms, contributing to improve water quality. It consists of the use of a photocatalyst, usually a semiconductor, which, when exposed to light radiation, is capable of promoting oxidation/reduction reactions that can be used to remove pollutants. It is a process relatively simple in its operational requirements, which due to its heterogeneous nature allows the recovery and reuse of the photocatalyst, reducing costs.

In this sense, this chapter aims to describe the photocatalytic process in the oxidation/reduction of heavy metals. In particular, describing how operational aspects influence the process.

PHOTOCATALYTIC PROCESS FOR OXIDATION AND REDUCTION OF HEAVY METALS

Heterogeneous photocatalysis had its origins in 1972, when Fujishima and Honda used electrodes with titanium dioxide to carry out experiments on the photo-oxidation of water. This experiment demonstrated that it was possible to break the bonds of water molecules using a semiconductor activated by sunlight, and from these results, severam works began to be developed in this area of research (Kumar and Devi 2011). However, it was not until the 1980's that researches identified photocatalysis as a promising technology for effluents treatment (WANG, YANG, and HE 2011).

Since then, several researches have been dedicated to the understanding of photocatalytic processes (Linsebigler, Lu, and Yates 1995). The areas of application of photocatalysis have been expanded over the years, ranging from water treatment to removal of dyes (C. H. Nguyen, Fu, and Juang 2018), pollutants of emerging concern (Arfanis et al. 2017; Bernabeu et al. 2011) and heavy metals (Fontana, Chaves, et al. 2018), passing through air purification processes (Mamaghani, Haghighat, and Lee 2018), hydrogen production (Mamaghani, Haghighat, and Lee 2018), and going to polymer synthesis and promotion of organic reactions (Corrigan et al. 2016), removal of odors (Nishikawa and Takahara 2001), photocatalytic ceramics (self-cleaning tiles) (Singh, Sharma, and Vaish 2021) and others.

The photocatalytic process starts when the photocatalyst is activated by the absorption of photons with an energy greater than that of the material's band gap[1]. When this occurs, an electron (e^-) from the valence band (BV) is promoted to the conduction band (BC) and a gap (h^+) is formed in the valence band. The reducing character of the electron promoted to the conduction band (BC) and the oxidizing character of the gap created in the valence band (BV) cause the organic and inorganic substrates adsorbed on the catalyst surface to undergo redox-type reactions, promoting transformations physicochemical in the substrate (Gouvêa et al. 2000). The simplified and general mechanism for this process is illustrated in Figure 1. It is noteworthy that it is possible to use both natural (solar) and artificial (lamps) radiation to promote photocatalysis.

---

[1] Band gap a diferença de energia entre a banda de valência e a banda de condução.

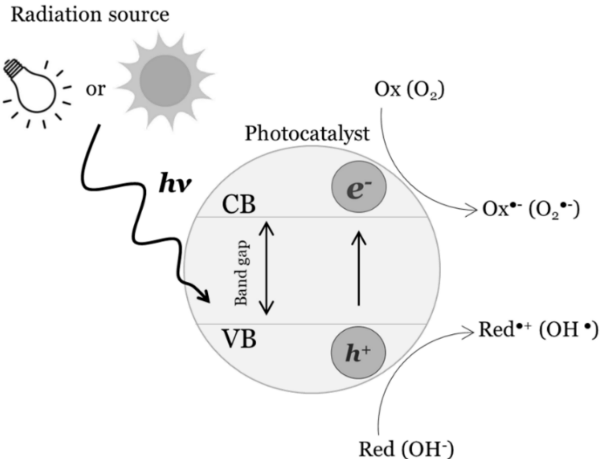

Figure 1. Simplified representation of the photocatalysis process.

Thus, it is possible to take advantage of the photo-generated electrons and holes that migrate to the photocatalyst surface to oxidize or reduce pollutants that are present in the aqueous medium. This may happen either by the direct transfer of electrons between the oxide and the adsorbed contaminant, or by the action of highly reactive radicals that are formed as a result of interaction between the electrons/holes of the photocatalyst and other substrates present in the medium (Bertinetti et al. 2016; Bora and Mewada 2017; Prado et al. 2008). When a water molecule, for example, is exposed to the photocatalyst in its excited state, it can react with the electron/hole pair on the surface. The holes show very positive potentials, in the range of +2.0 to +3.5 V, depending on the semiconductor and the pH (Nogueira and Jardim 1998), being, therefore, capable of generating hydroxyl radicals ($OH^{\bullet}$) from of adsorbed water molecules. Due to this ability to generate these radicals, heterogeneous photocatalysis is considered an Advanced Oxidative Process (AOP). AOPs have in common the fact that they produce highly reactive radicals, such as hydroxyl radicals, which act as oxidizing agents in the degradation of organic pollutants (De la Cruz et al. 2012; Byrne, Subramanian, and Pillai 2018; Farrokhi, Feizpour, and Asaadzadeh 2019; Bora and Mewada 2017).

the complete mineralization of the contaminant. When the pollutant is a metal ion, on the other hand, the only solution left is to reduce or oxidize it into a less toxic and/or easier to remove form. In the case of lead in an aqueous medium, for example, it is possible to promote its photocatalytic reduction from Pb(II) to the elementary form Pb(0), which is deposited on the photocatalyst surface, being easily removed in a later stage of the process (Chen and Ray 2001). As for arsenic, on the other hand, a route commonly used is the photocatalytic oxidation of As(III) to As(IV), which, despite also being soluble in aqueous media, is known for its lower toxicity and mobility, being more easily removed by adsorption, precipitation or ionic exchange (Fontana, Lenzi, et al. 2018).

Many elements, by the way, can undergo either photocatalytic oxidation or reduction, depending on the conditions employed in the process. A good example of this is Pb(II) (Murruni, Leyva, and Litter 2007). Therefore, it is common to use compounds that act preventing the recombination of the e^- /h^+ pairs while favoring the occurrence of one photocatalytic pathway over another. To favor the photo-oxidation reaction, for example, it is common to use so-called *electron scavengers*, which are species that capture photogenerated electrons, preventing their recombination with holes, which are then free to participate in oxidation reactions. A good example of electron scavengers is oxygen. In order to promote photocatalytic reduction, in turn, it is necessary to employ compounds classified as *hole scavengers*, which act as electron donors for the formed holes, allowing the photogenerated electrons to be available to promote reduction reactions (Murruni, Leyva, and Litter 2007; Chen and Ray 2001). The use of hole scavengers is widespread to promote photoreduction of polluting metals, including examples such as formic acid and EDTA. Again, the contribution of these organic additives to the photocatalytic process can occur in two ways: direct or indirect. In the first case, the electrons from the organic compound are transferred directly to the formed holes, promoting higher rates of reduction, while in the second case, the gaps are consumed through the formation of hydroxyl radicals, which, in turn, react with the organic compounds present in the medium, leading to not so fast reduction rates (Chen and Ray 2001; Prairie et al. 1993).

Furthermore, photocatalysis process is highly dependent on the properties of the photocatalyst. Semiconductors, usually oxides, are the materials most commonly used as photocatalysts, due to their interenting electronic characteristics. Compared to insulating materials (which have a very large gap energy that prevents the electrons transfer between VB and CB) and conductive materials (in which VB and CB are superimposed allowing the free movement of electrons), semiconductors material have an energy gap small enough to allow excitation by light radiation and the formation of e^-/h+ pairs (Figure 2) (Karthikeyan et al. 2020). Besides the energy difference between the VB and CB (known as band gap energy, *Eg*), the photocatalyst efficiency is also affected by the absolute potentials of the bands (E_{VB} and E_{CB}, also known as the position of the bands), and by the photo-generated e^- and h^+ dynamics, i.e., their mobility and duration (lifetime) in the photocatalyst (H. L. Tan, Abdi, and Ng 2019).

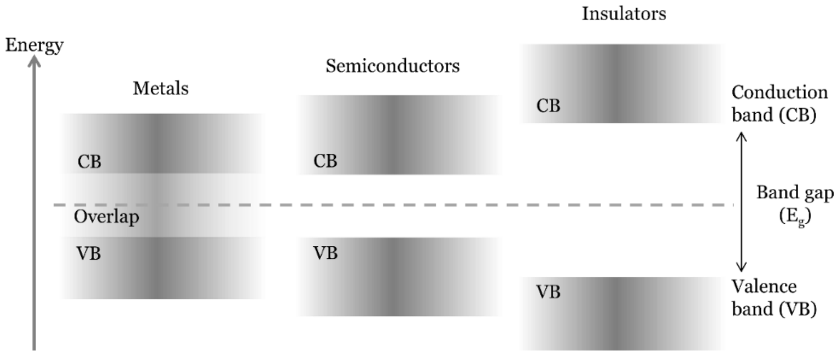

Figure 2. Diagram of the bands and band gap of metals, semiconductorsand insulators (Karthikeyan et al. 2020).

the species in question, while for photo-oxidizing a species, the potential the valence band (E_{VB}) must be more positive than the oxidation potential of the element (Kabra, Chaudhary, and Sawhney 2008). If this criterion is not met, the reduction/oxidation becomes thermodynamically unfavorable.

The conduction and valence bands of a photocatalyst are not always constant, and may vary depending on the pH of the medium (Chen and Ray 2001; Mishra et al. 2007). In the case of titanium dioxide, the variation in band potentials can be described according to Equations (1) and (2) (Chen and Ray 2001):

$$E_{BC}(V) = -0.05 - 0.059\ \mathrm{pH}\ (25°\mathrm{C}) \tag{1}$$

$$E_{VC}(V) = 3.15 - 0.059\ \mathrm{pH}\ (25°\mathrm{C}) \tag{2}$$

As a result, photocatalytic reduction of metallic ions by TiO_2 tends to be favored at higher pH, a condition in which photocatalyst's E_{CB} becomes more negative. For some metallic cations such as Cd(II) and Cr(III), on the other hand, photocatalytic reduction by TiO_2 becomes unfeasible, since their reduction potentials are more negative than the photogenerated electrons potentials (E_{CB}) (Chen and Ray 2001). In addition, it is also necessary to consider that the pH of the medium can also affect the reduction potential of some metallic ions, such as Cr(VI) (Chen and Ray 2001), and change the surface charges of the photocatalyst, which ends up affecting the electrostatic interaction between the ions and the solid surface, affecting the adsorption process (Mishra et al. 2007).

In addition, to being photocatalytically active, meeting the electronic requirements mentioned above, it is desirable that the semiconductor photocatalyst is also chemically and biologically inert, stable, and easy to obtain and use, with efficient catalytic activity, low cost, not presenting toxicity to the environment or human beings. Several catalysts (semiconductors) are used/studied for photocatalytic processes. However, not all semiconductors can be used in photocatalytic processes, as they do not satisfy the conditions of photoactivity (activation through radiation) and photostability (maintaining the physicochemical characteristics in the presence of light). This can be seen in the case of Cadmium sulfide (CdS), which can absorb radiation up to 510 nm, but suffers photocorrosion when it receives the incidence of ultraviolet (UV) radiation and generates Cd^{2+} ions, making its use in decontamination processes impossible (Teixeira and Jardim 2004). On the other hand, semiconductors such as titanium dioxide (TiO_2), niobium pentoxide (Nb_2O_5) and zinc oxide (ZnO) have stood out as catalysts in photocatalytic processes, mainly due to their photoactivity characteristics, stability and for not presenting toxicity.

Thus, the photocatalysis process applied to the removal of heavy metals can be influenced by numerous factors. Therefore, in the next topics, we will address specific aspects of the process for some of the main elements found in aqueous media.

PHOTOCATALYTIC REDUCTION PROCESSES

Lead Reduction

Lead (Pb) is a heavy metal (atomic number 82, Group 14 of periodic table), which represents 13 mg kg^{-1} of the earth's crust composition. It is predominantly found in the Pb(II) (or Pb^{2+}) oxidation state when in its inorganic form, and less frequently as Pb(IV). Most of Pb(II) salts are difficult to dissolve in water, but there are exceptions such as lead nitrate and chlorate (Skerfving and Bergdahl 2015; WHO 2011). Exposure to lead can cause acute effects in humans such as headaches, encephalopathy, tremors, hallucinations, memory loss and kidney damage renais (WHO 2011). Severe inorganic lead poisoning can also cause seizures, ataxia and coma, and studies also indicate harmful effects of lead on cognitive functions (Skerfving and Bergdahl 2015). In face of so many risks to human health, there is great concern in remedying lead contamination of water. Conventional methods for lead removal include precipitation (either in the form of carbonate, hydroxide or after being chelated by compounds such as EDTA), electrolysis and chemical oxidation, all of which have the disadvantage of being costly processes (Murruni, Leyva, and Litter 2007).

High cost is a problem common to several conventional treatment methods for heavy metals removal, which can also suffer from the generation of other contaminating wastes, which limits its application on a larger scale (Srivastava and Majumder 2008).

Table 1. Some photocatalytic processes applied to lead removal described in the literature

Photocatalyst	**Operational conditions**	**Removal/ Main results**	**Year**	**Ref.**
Pt-TiO_2 (rutile)	Mercury vapor lamp (500 W), C_i=0.001 mol L^{-1} of Pb^{2+}, pH=3.4 (not adjusted).	91% (60 min) Suspension became brown.	1986	(Tanaka, Harada, and Murata 1986)
TiO_2 (P-25)	Xe lamp (1500W), pH <4	Brown suspension, photo-oxidation	1992	(Torres and Cervera-March 1992)
TiO_2 (P-25, 2 g L^{-1})	Mercury vapor lamp (125 W), C_i=0.6 mM of Pb^{2+}, Natural solution pH, T=303 K, N_2 purge.	27.2% (65 min) photoreduction	2001	(Chen and Ray 2001)
Si-TiO_2 (1.5 g L^{-1})	UV Lamp (125 W), C_i=100 ppm of Pb^{2+}, pH= 3.5, sodium formate (200 ppm), air at atmosphetic pressure	99.4% (30 min) photoreduction	2007	(Mishra et al. 2007)
Pt-TiO_2 (1.0 g L^{-1})	Black light UV Lamp (15 W), C_i=0.5 mM, pH=3, no hole scavengers, bublled with O_3	93% (290 min) photo-oxidation	2007	(Murruni, Leyva, and Litter 2007)
TiO_2 (2.0 g L^{-1})	Solar light, C_i=20 mg L^{-1} of Pb^{2+}, pH=4, citric acid (140 ppm)	Around 65% of photodeposition	2007	(Kabra, Chaudhary, and Sawhney 2007)
TiO_2 (0.1 g L^{-1})	UV lamp (125W), C_i=20 mg L^{-1} of Pb^{2+}, pH=4.2 citric acid (3.86 10^{-4} mol L^{-1}),	100% (90 min)	2017	(Peter et al. 2017)

This has enabled the expansion of new technologies such as heterogeneous photocatalysis. The photocatalytic reduction of lead has been studied for decades, with a wide variety of works in the area with encouraging results (Table 1).

Several parameters have already proven to be relevant for lead photocatalysis, such as: photocatalyst type and its CB and VB potentials (Kabra, Chaudhary, and Sawhney 2008); photocatalyst modification by elements, such as Pt (Murruni, Leyva, and Litter 2007); initial pH (Kabra, Chaudhary, and Sawhney 2007); the presence or not, type and concentration of organic electron donors (Murruni et al. 2008; Mishra et al. 2007; Peter et al. 2017); radiation source (Mishra et al. 2007); and N_2, O_2 or O_3 bubbling into solution (Chen and Ray 2001; Murruni, Leyva, and Litter 2007).

Photoreduction of Lead and the Use of Organic Electron Donors

Studies about lead photocatalysis indicated that it is possible to either reduce or oxidize Pb(II) ions in an aqueous medium, depending on the conditions used during the photocatalytic process. The main advantage of the reduction pathway is the possibility of recovering lead in its elemental form (Pb^0) (Chen and Ray 2001). One of the determining factors for favoring photoreduction is the use of hole scavengers (electron donors), which act by inducing the reduction of Pb(II) ions and preventing the e^-/h^+ pairs recombination (Chen and Ray 2001). For this purpose, it is possible to use different organic compounds, such as alcohols (e.g., methanol, ethanol and propanol), carboxylic acids (e.g., formic acid, citric acid and succinic acid), sodium formate, EDTA, among others (Murruni et al. 2008; Chen and Ray 2001; Mishra et al. 2007).

In this regard, Murruni et al. (2008) developed a study on the effects of different organic compounds used as electron donors in lead reduction. Among the compounds studied (methanol, ethanol and propanol, formic acid and citric acid) formic acid stood out for its good results and for having the advantage of producing non-toxic species as by-products (Murruni et al. 2008). According to them, carboxylic acids such as formic acid and citric acid act differently from alcohols in the reduction process, as they have greater adsorption capacity and even complexation with the photocatalyst surface, which would favor their performance as hole scavengers. Meanwhile, alcohols act mainly consuming $HO^\bullet$ radicals (Murruni et al. 2008).

Mishra et al. (2007) also studied the action of hole scavengers in lead photocatalytic reduction, and observed that the addition of these compounds led to a considerable increase in the element removal. The order of efficiency determined experimentally was: sodium formate > methanol > formic acid > succinic acid. According to the authors, the better performance of sodium formate compared to formic acid is due to the fact that the latter reduces the pH when it is added to the suspension, which would harm the photocatalytic process (Mishra et al. 2007). Kabra et al. (2008), in turn, used citric acid as hole scavengers, and noted that this compound favored both adsorption and deposition of lead on the surface of the photocatalyst (Kabra, Chaudhary, and Sawhney 2008). Peter et al. (2017) also used citric acid as an electron donor to promote lead reduction, obtaining good results (Peter et al. 2017). According to what Murruni et al. (2008), citric acid presents, in addition to its action as an electron donor, a stabilizing effect for Pb(0) atoms, which prevents its reoxidation when exposed to the atmosphere (Murruni et al. 2008).

In fact, the possibility of reoxidation can be quite problematic for the lead photocatalytic reduction. As reported by Murruni et al. (2008), the radiation used during the process can induce reoxidation, due to the depletion of the electron donor, which leads to an increase in the concentration of lead in the solution after long periods of illumination. The authors noted that, although variations in formic acid concentrations did not have a significant impact on Pb removal rates, the use of very low concentrations of this acid (0.005M) resulted in an increase in lead concentration after 120 min of irradiation (Murruni et al. 2008). Furthermore, lead oxidation can also be induced by the presence of dissolved oxygen in the reaction medium (Tanaka, Harada, and Murata 1986), since it acts as an electron scavenger[2], being reduced preferentially instead of Pb(II), due to its reduction potential (Chen and Ray 2001). Thus, for the reduction to be favored, some authors, such as Chen and Ray (2001) and Murruni et al. (2007), recommend the use of an N_2 purge (Chen and

---

[2] *Electron scavenger*: substance that acts by suppressing the e^-/h^+ pair recombination by reacting/capturing the photogenerated electrons, allowing the respective holes to be free to promote oxidation reactions. Ex: O_2 (Chen and Ray 2001).

Ray 2001; Murruni et al. 2008). Despite this, Mishra et al. (2007) also report having promoted lead reduction without complete oxygen removal, as they photocatalytically reduced Pb(II) in the presence of air at atmospheric pressure (Mishra et al. 2007).

The pH Effect

Another important factor to consider in the lead photoreduction process is the pH of the medium during the process, as the pH can affect both the surface properties of the photocatalyst (surface charges) and also shift the potential of the conduction band (Mishra et al. 2007). As for surface charges, lead adsorption tend to be less favorable at pH lower than the photocatalyst PCZ, because in this condition the solid surface is positively charged, which hinders the electrostatic interaction between the surface and the metallic cations. In this sense, Mishra et al. experimentally observed a decrease in the percentage of Pb(II) adsorption when the initial pH of the solution was reduced from 3.5 to 2.6 (Mishra et al. 2007).

Still, some works indicate acidic pH values as being the best for lead photoreduction. Kabra et al. (2007), for example, observed that lead adsorption in TiO_2 photocatalyst was better at acidic pHs, with greater removal at pH=4 (64.9%), and lead photodeposition by solar photocatalysis followed the same trend (Kabra, Chaudhary, and Sawhney 2007). Some studies report a decrease in the pH value of the suspension as the concentration of Pb(II) decreased in the suspension(Murruni, Leyva, and Litter 2007), both in the photocatalysis, photolysis and adsorption processes (Peter et al. 2017). Due to this phenomenon, Murruni et al. (2007) performed periodic additions of NaOH to the suspension in order to maintain the pH equal to 3 (Murruni, Leyva, and Litter 2007). At basic pH, on the other hand, it is necessary to take into account the possibility of lead precipitation due to its conversion into hydroxide at very high pH values, normally around 10(Kabra, Chaudhary, and Sawhney 2007). Kabra et al. (2008), for example, studied the effects of pH on the removal of metallic ions, such as Pb(II), and added citric acid to the reaction medium as an additive to simulate the organic component of an industrial effluent. At pHs lower than 8, the authors observed the complexation of Pb2+ ions with citric acid, while at pH 10 lead was almost completely converted to its hydroxide (Kabra, Chaudhary, and Sawhney 2008).

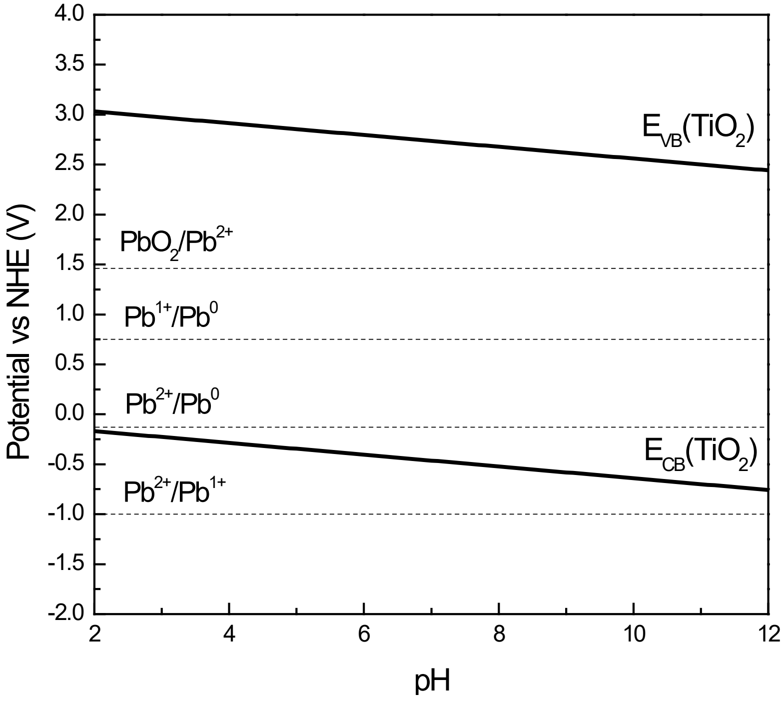

Figure 3. Redox potentials of Pb species (Torres and Cervera-March 1992; Kabra, Chaudhary, and Sawhney 2008; Murruni, Leyva, and Litter 2007) and CB and VB potentials for TiO_2, calculated according to Eq. (1) and (2) (Chen and Ray 2001).

As previously mentioned, the pH of the medium can also change the potential of the valence and conduction bands of photocatalysts such as TiO2 (Chen and Ray 2001), which ends up affecting the lead reduction process (See Equations 1 and 2 in the Introduction). As a result, the probability of lead reduction by photocatalysis with TiO2 decreases in conditions of very low pH, due to the low driving force (Chen and Ray 2001), as can be seen in Figure 3.

Lead Photoreduction Mechanism

According to Peter et al. (2017), Pb(II) photoreduction mechanism starts when lead ions present in the solution (Pb^{2+}, $PbOH^+$ and Pb_2OH^{3+}, depending on pH) diffuse from the bulk solution to the photocatalyst surface, passing through the film diffusion around the particle, to be dehydratated and adsorbed on the catalyst surface. Then, CB photogenerated electrons can reduce adsorbed Pb^{2+} ions to form Pb^0, which remains deposited on the photocatalytic surface. The VB holes, on the other hand, can promote the oxidation of other adsorbed species, such as citric acid (Peter et al. 2017). It is also worth to remember that the adsorption of metallic ions, such as lead, on the photocatalyst surface is influenced both by the zero charge point (PCZ) of the oxide and by the type of hole scavenger used in the process (Mishra et al. 2007) (see previous discussion).

As shown in Figure 3, by considering that Pb^{2+} reduction occurs through two consecutive monoelectronic transfer steps ($E_{(Pb^{2+}/Pb^{1+})} = -1.0$ V and $E_{(Pb^{1+}/Pb^{0})} = 0.75$ V), it turns out that the first stage is thermodynamically unfavorable, due to its highly negative reduction potential [16]. Being the reduction via one-electron transfer not feasible, Rajh et al. (1996) proposed that lead reduction could occur via a two-electron transfer process, which presents a less negative redox potential (Rajh et al. 1996). This would be possible, for example, by the photocatalytic surface modification by compounds such as cysteine, enabling the accumulation of electrons which can be simultaneously transferred to reduce lead ions (Rajh et al. 1996; Thurnauer et al. 1997). In this case, the pH increase would favor the reduction of lead, by increasing the driving force of the two-electron transfer (Figure 3).

Another possible way to reduce Pb2+ is the addition of metals such as Pt to the photocatalyst, which allows shifting the potential of photogenerated electrons to more negative values (Murruni, Leyva, and Litter 2007). As proposed by Murruni et al. (2007), Pt is able to capture electrons and then transfer them to Pb^{2+}, transforming them from divalent to monovalent form. From that point onwards, the reduction to the elementary state can easily occur (Murruni, Leyva, and Litter 2007). It is necessary to consider, however, that photgenerated hole and $HO^{\bullet -}$ radicals can easily reoxidize the Pb(0) and Pb(I) species, harming the reduction process. For this reason the addition of an electron donors is so advantageous, as it preferentially reacts with the $HO^{\bullet -}$ radicals and holes, preventing lead reoxidation, while producing highly reducing radicals ($R^{\bullet -}$), which contribute Pb(II) reduction (Murruni et al. 2008).

Different Photocatalysts Applied to Lead Photoreduction and Photocatalyst Reuse

Among the catalysts applied to lead photoreduction, there is a predominance of TiO_2-based photocatalysts (Tanaka, Harada, and Murata 1986; Torres and Cervera-March 1992; Chen and Ray 2001; Kabra, Chaudhary, and Sawhney 2007; Peter et al. 2017), but several studies have been carried out regarding the improvement of titanium-based catalysts and also the development of new catalysts. The addition of metals such as Pt to TiO_2, for example, can contribute to shift the CB potential to more negative values, favoring the reduction of Pb^{2+} ions (Murruni, Leyva, and Litter 2007). It is also possible to promote modifications on the TiO_2 surface by using compounds such as cysteine, which, according to Rajh et al. (Rajh et al. 1996) allows the occurrence of a multi-electronic transfer to promote the reduction of lead. Another possibility, as proposed by, You at al. (You et al. 2018), is the combiantion of oxides (like p-type Bi_2O_3 with n-type TiO_2) in order to produce a composite with separate reaction sites, which contribute to a better efficiency of the photocatalytic process, in addition to favoring the reduction of Pb(II) simultaneously with the oxidation of organic pollutants. The 4%Bi2O3-TiO2 composite particles produced by the authors showed stability and presented a significant decrease in the efficiency of lead reduction only after 5 times of recycling (You et al. 2018). Another advantageous approach is the application of photocatalysts immobilized in alginate-based beads (Majidnia and Fulazzaky 2016), some of which are even magnetic (Kanakaraju et al. 2019), which greatly favors the the photocatalyst separation and recyclyng at the end of the process. Kanakaraju et al. (Kanakaraju et al. 2019) observed that TiO_2/Alg/FeNPs magnetic beads preserved its photocatalytic activity without great decrease for Pb(II) removal even after three cycles of reuse.

Selenium Reduction

Selenium is a metalloid (atomic number 34, Group 16), naturally found in nature, in soil, rocks and even in some foods, required by the human body in very small quantities (trace element) (Torres-Vega et al. 2012; Prabhu and Lei 2016; L. C. Tan et al. 2016). Even though it is not part of the group of metals in the periodic table, selenium can be considered a heavy metal in some definitions (Duffus 2002), in view of the damage it can cause to environment and to living organisms if ingested in large concentrations (Hwang et al. 2011; Zhou et al. 2017; Vinceti et al. 2018; 2010; 2016; Lemly 2018). In humans, chronic selenium poisoning (selenosis) has as main symptoms irritation, fatigue, hair and nail loss, nervous system problems, and others (Prabhu and Lei 2016; Torres-Vega et al. 2012).

Despite the existence of a natural selenium cycle, human activities, especially industrial activity, have affected the concentration of this element in certain places around the globe. The main sources of selenium pollution are mining, agriculture and the burning of fossil fuels, like coal (Cordoba and Staicu 2018; Lemly 2004). A study carried out in China, in a region close to three coal-based power plants, registered an increase in selenium leves in the soil (2.37 mg kg^{-1} on the surface) and in water (between 0.002 and 0.29 mg L^{-1}), which resulted in increased Se concentration in rice produced in the region (HUANG et al. 2009). In aquatic environments, selenium contamination can be potentially dangerous, due to the risks it poses to aquatic life (Lemly 2018) and its ability to bioaccumulate in the food chain (Lemly 2004).

Selenium can be found in both organic and inorganic forms, the latter being considered more toxic (Prabhu and Lei 2016). In aqueous medium, it is commonly present in inorganic forms as selenite (Se(IV) or SeO32-)

and selenate (Se(VI) or SeO42-) oxyanions[3] (Figure 4), which may or may not be protonated, depending on the pH (V. N. H. Nguyen, Beydoun, and Amal 2005).

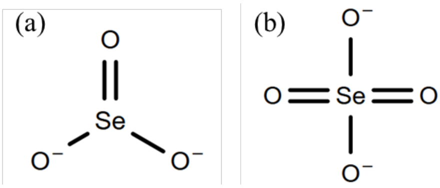

Figure 4. Selenite (a) and selenate (b) oxyanions.
Source: Royal Society of Chemistry (2019) (Royal Society of Chemistry 2019).

Selenium remediation can be perfomed by different techiniques, such as adsorption, bioremediation, coagulation-floculation, electrocoagulation, reduction and electrochemical reduction methods, among others. Reduction methodologies, such as heterogeneous photocatalysis, allow to reduce the ionic forms of selenium to elemental selenium, thus reducing its mobility and the risk of exposure to selenium, and allowing its removal from the aqueous medium (V. N. H. Nguyen, Beydoun, and Amal 2005; He et al. 2018; L. C. Tan et al. 2016).

Studies regarding the photocatalytic removal of selenium indicated that reduction can be performed by using TiO_2-based photocatalysts, under acidic pH conditions and with the addition of hole scavengers, mainly formic acid (Table 2).

Tan et al. (Timothy T.Y. Tan et al. 2002), for example, were able to photoreduce Se(IV) and Se(VI) to elemental selenium using TiO_2 (Degussa P25, 80% anatase and 20% rutile) as photocatalyst, at pH equal to 2.6 and using N_2 purge. At the end of the process, the authors observed a change in the color of the suspension, which changed from white to an orange-pink tone, due to the deposition of selenium on the surface of the photocatalyst (Timothy T.Y. Tan et al. 2002).

---

[3] Oxyanions: ionic form consisting of a central atom bonded to oxygen atoms It includes anions such as selenite, selenate, chromate, nitrate, nitrite, chlorite, among others (Zhao, Zhang, and Zhang 2020).

Table 2. Some photocatalytic processes applied to selenium removal described in the literature

Photocatalyst	**Operational conditions**	**Removal / Main results**	**Year**	**Ref.**
TiO_2 (P25, 1.1 g L^{-1})	Mercury lamp (200 W) 20 ppm Se(VI) pH=2.6 Formic acid (100ppm) N_2 purging	100% (60 min)	2002	(Timothy T.Y. Tan et al. 2002)
TiO_2 (P25, 1.1 g L^{-1})	Mercury lamp (200 W) 20 ppm Se(VI) pH=2.6 Formic acid (100ppm) N_2 purging	91.6% (60 min)	2003	(Timothy T.Y Tan, Beydoun, and Amal 2003)
TiO_2 (P25, 1.1 g L^{-1})	Mercury lamp (200 W) 20 ppm Se(IV)/Se(VI) pH=3.0 Formic acid (300ppmC) N_2 purging	In 120 min: Se(IV): 90.1% Se(VI): 86.2%	2003	(T. Tan, Beydoun, and Amal 2003)
Ag-TiO2 (0.5 g L-1)	Mercury lamp (200 W) 0.254 mM Se(VI) pH=3.0 Formic acid (25 mMC) N2 purging	24.8% (120 min)	2003	(T. Tan, Beydoun, and Amal 2003)
TiO2 (PC-500)	Mercury lamp (200 W) 20 ppm Se(VI) pH=3.5 Formic acid N2 purging	95.7% (140 min)	2005	(V. N. H. Nguyen et al. 2005)
TiO2 (P25, 1.5 g L-1)	Mercury lamp (200 W) pH=3.5 20 ppm Se(IV)/Se(VI) Formic acid (300 ppmC) N2 purging	In 120 min: Se(IV): 94.5% Se(VI): 59.5%	2005	(V. N. H. Nguyen, Beydoun, and Amal 2005)
Zr-TiO2 (1.0 g L-1)	Mercury lamp (125 W) pH = 3.0 100 ppm Se(IV) Formic acid or EDTA	After 15 min: 76% (Formic acid) 81% (EDTA)	2011	(Aman et al. 2011)
Fe/TiO2 (1.0 g L-1)	Mercury vapor lamp (250 W) pH=3.3 500 µg L-1 Se ions 50 µL of Formic acid 85% to 500 mL of solution	98.9% (15 min)	2021	(Fuziki et al. 2020)
TiO2/CoFe2O4 (0.1 g L-1)	Mercury vapor lamp (250 W) pH=3.0 500 µg L-1 Se ions 50 µL of Formic acid 85% to 250 mL of solution	99% (2 min)	2021	(Fuziki et al. 2021)

A similar color change has also been reported in other works (Timothy T.Y Tan, Beydoun, and Amal 2003; Fuziki et al. 2021).

Photoreduction of Selenite and Selenate: The Role of Organic Electron Donors

Tan, Beydoun and Amal (T. Tan, Beydoun, and Amal 2003) studied the effect of six organic compounds (methanol, ethanol, acetic acid, salicylic acid, formic acid and sucrose) as electron donors for selenium photoreduction. Among then, only three were able to promote the photoreduction, which were, in decreasing order of efficiency: formic acid > methanol > ethanol. Regarding the pH effect, when methanol or ethanol were used as hole scavengers, the reduction of selenium was maximum at the lowest tested pH (2.2), while in the case of formic acid, the maximum removal was achieved at pH equal to 3.5 and 4.0 for Se(VI) and Se(IV), respectively (T. Tan, Beydoun, and Amal 2003).

Based on these results, Tan, Beydoun and Amal (T. Tan, Beydoun, and Amal 2003) concluded that methanol and ethanol act differently from formic acid in selenium photocatalysis. Adsorption tests performed by the authors showed that, among the studied organic compounds, only formic acid can be adsorbed by the photocatalyst in the presence of selenite and selenate ions. For the other electron donors, selenium ions were preferentially adsorbed, leading to an insignificant adsorption of the organic additives. Based on this, the authors concluded that, possibly, methanol and ethanol favor the photoreduction of selenium by reacting with the hydroxyl radicals generated by photocatalysis. Thus, the maximum reduction of selenium occurred at the lowest pH, a condition that favors selenite and selenate adsorption, due to the electrostatic interactions between these anions and the positively charged surface of the photocatalyst (T. Tan, Beydoun, and Amal 2003).

As for formic acid, its better performance as an additive in the photoreduction of selenium would be justified by its ease in being mineralized and by its action as a hole scavenger, both directly, when adsorbed on the surface of the photocatalyst, and indirectly, when reacting with the hydroxyl radicals formed during photocatalysis (T. Tan, Beydoun, and Amal 2003). Therefore, the efficiency of the process depends on the simultaneous adsorption of formate ions and selenite and/or selenate. Based on this principle, Tan, Beydoun and Amal (Timothy T.Y Tan, Beydoun, and Amal 2003) found as ideal adsorption ratio 3 mol of formate ions to 1 mol of Se(VI) ions.

In the comparison made by Aman et al. [51], among different hole scavengers used in simultaneous Cu(II) and Se(IV) reduction, formic acid and EDTA showed the best results, with formic acid being more efficient for the removal of pure Se(IV), while EDTA had more effective action in the simultaneous reduction of both metals.

The pH Effect

From the point of view of selenite and selenate ions only, their adsorption is favored at low pH, a condition in which the photocatalyst surface is positively charged, providing a better electrostatic interaction with the oxyanions (Timothy T.Y. Tan et al. 2002). Given the importance of adsorption for the efficiency of photocatalysis, it is expected maximum photoreduction of selenium to be observed at the lowest pH values, which, however, is not verified experimentally. Tan, Beydoun and Amal (Timothy T.Y Tan, Beydoun, and Amal 2003), for example, tested pHs between 2 and 6.4, obtaining the higher reaction rate at pH around 4. Fuziki et al. (Fuziki et al. 2021) also obtained better photoreduction results at intermediate pH between 2 and 5.

According to Tan et al. (Timothy T.Y Tan, Beydoun, and Amal 2003), this behavior is caused by the competitive adsorption of selenium and formate ions. Formic acid acts as a hole scavenger during photocatalysis, preventing the recombination of e^-/h^+ pair and facilitating the photoreduction of selenium, which makes it important to assure the proper adsorption of formate ions on the catalyst surface. While Se(IV) and Se(VI) are more adsorbed at low pH, formic acid adsorption is favored by pH increasing to values close to 5. The optimal pH condition for photoreduction, therefore, is achieved when both selenite and formate ions are adsorbed in an adequate proportion. Tan et al. (Timothy T.Y Tan, Beydoun, and Amal 2003) concluded that the best removal results are obtained when formate and selenate are adsorbed in the catalyst surface at stoichiometric ratio close to 3:1. Such condition can be achieved by varying either the concentrations of the reagents (selenium and formic acid) or the pH of the solution. Tan, Beydoun and Amal (Timothy T.Y Tan, Beydoun, and Amal 2003) experimentally determined that the optimum pH for Se(VI) would be close to 3.5 for a concentration of 300 ppmC of formic acid and 20 ppm of Se(VI).

Selenium Photoreduction Mechanism

Based on the reduction potentials of selenite (SeO_3^{2-}/Se, 0.90 V) and selenate (SeO_4^{2-}/Se, 1.06 V) (Zhao, Zhang, and Zhang 2020), compared to the CB potential of TiO_2 in acidic conditions (-0.3 V) (V. N. H. Nguyen, Beydoun, and Amal 2005), it is thermodynamically possible to reduce selenium anionic species to Se^0 by the action of the CB photogenerated electrons. Furthermore, the radicals formed by the hole scavengers oxidation also have potentials capable of promoting the reduction of selenium ions (T. Tan, Beydoun, and Amal 2003). Nguyen, Beydoun and Amal (V. N. H. Nguyen, Beydoun, and Amal 2005) experimentally observed that selenate and selenite photoreduction to elemental selenium resulted in both the formation of Se^0 deposits on the photocatalyst surface and the formation of discrete Se^0 particles dispersed in the medium. The authors proposed that the mechanism of selenite photoreduction can occur both by the direct reduction promoted by the electrons generated by the photocatalyst (leading to the formation of deposits) and by the reaction between the SeO_3^{2-} and the Se^{-2} ions produced by the reduction of Se^0 (resulting in discrete particles formation) (V. N. H. Nguyen, Beydoun, and Amal 2005). This is schematically represented in Figure 5.

The formation of Se^{-2} can also provide important information about how the selenium reduction process takes place. Some works report that the formation of H_2Se (a toxic gas) only starts when the selenium ions are almost totally consumed (Timothy T.Y. Tan et al. 2002; Timothy T.Y Tan, Beydoun, and Amal 2003).

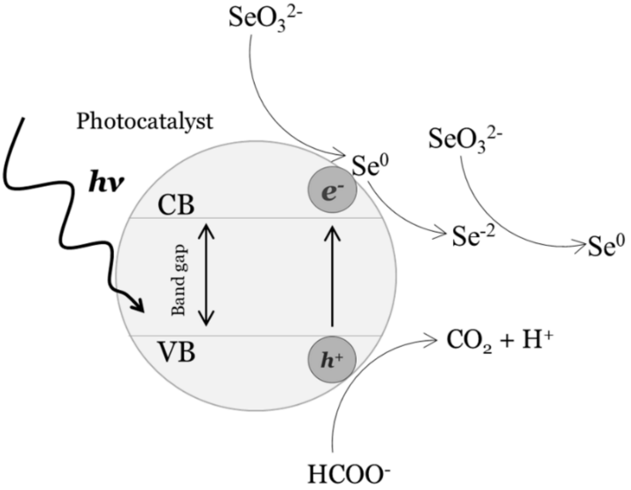

Figure 5. Selenite reduction mechanism according to (V. N. H. Nguyen, Beydoun, and Amal 2005).

Interestingly, the formation of H_2Se was observed by Tan et al. (2003) while Se(VI) ions were still present in the solution when using Ag-TiO_2 catalyst (T.T.Y Tan et al. 2003). This led the authors to conclude that, in the TiO_2 catalyst, the generated electrons are continuously transferred to the Se^0 particles deposited on its surface, from where they can also be transferred to ionic species present in the medium. However, this transfer of electrons from TiO_2 to Se^0 continues even after the ions are exhausted from the suspension, which causes electrons to accumulate in the Se particles. This charge accumulation, in turn, allows the Se to self-reduce to H_2Se. In Ag-TiO_2 particles, in turn, the presence of silver considerably accelerates the electrons transfer from TiO_2 to Se, which makes the carges accumulation on the selenium particles (and consequently self-reduction) possible even before the complete consumption of the selenium ions (T.T.Y Tan et al. 2003).

In fact, the reduction from Se^0 to Se^{-2} can hardly occur by the action of TiO_2 alone, since the Se^0/H_2Se redox potential is considerably negative (-0.6 V) (Holmes et al. 2021). According to Ngyuen et al. (V. N. H. Nguyen, Beydoun, and Amal 2005), once Se^0 deposits are formed, it is possible to reduce Se^0 to Se^{-2}, due to the more negative potential of CB of Se particles

(V. N. H. Nguyen, Beydoun, and Amal 2005). More recently, Holmes et al. (Holmes et al. 2021) studied the selective reduction of Se(VI) ions in a complex aqueous matrix containing nitrate and sulfate, and also focused on the study of the mechanism of selenium reduction. The author proposed that selenate reduction to Se^0 is promoted by direct action of photogenerated electrons present in semiconductor (TiO_2) CB, while the reduction of Se^0 to Se^{-2} (formation of H_2Se) occurs by the action of photogenerated electrons in Se CB and by the action of $CO_2^{\bullet-}$ radicals (Holmes et al. 2021).

Application and Reuse of Photocalalysts on Selenium Photoreduction

As it can be seen in Table 2, most research about selenium photoreduction made use of TiO_2-based photocatalyst, mainly Degussa P25 (Timothy T.Y. Tan et al. 2002; Timothy T.Y Tan, Beydoun, and Amal 2003; T. Tan, Beydoun, and Amal 2003; V. N. H. Nguyen, Beydoun, and Amal 2005). Such catalysts mainly contain the anatase form of TiO_2 (Degussa P25 is composed of 70% of anatase and 30% of rutile (Timothy T.Y Tan, Beydoun, and Amal 2003)), suggesting that this polymorphic phase favors the photoreduction of selenium. This was confirmed by Fuziki et al. (Fuziki et al. 2021), who observed a drastic decrease in Se(IV) reduction efficiency when photocatalysts with high rutile-TiO_2 contents were used.

Tan et al. (2003) studied the effect silver nanoparticles on TiO_2 for selenium removal, and the results demonstrated that both pure TiO_2 and Ag-TiO_2 were able to efficiently photoreduce selenium. The biggest difference between them concerns the formation of H_2Se, which occurred simultaneously with the reduction of Se(VI) in the case of the Ag-TiO_2 catalyst, but only occurred after all the consumption of Se(VI) for bare TiO_2 (T. Tan, Beydoun, and Amal 2003).

Aman et al. (Aman et al. 2011), in turn, used titanium dioxide and other binary oxides (mixed oxides of titania/silica and titania/zirconia) in the simultaneous reduction of Cu(II) and Se(IV) by photocatalysis. Using formic acid as a hole scavenger, the authors were able to achieve removal percentages of around 90% in 22 minutes of photocatalysis, for a solution with an initial concentration of 50 ppm of Se(IV), with TiO_2 as a photocatalyst at a pH equal to 3 (Aman et al. 2011).

Another possibility is the application of magnetic photocatalysts to the photoreduction of selenium. This type of catalyst has as its main advantage the possibility of easy separation of the suspended particles after the end of the photocatalytic process. In this sense, Fe/TiO_2 (Fuziki et al. 2020) and $TiO_2/CoFe_2O_4$ (Fuziki et al. 2021) catalysts were studied in the reduction of selenium, and good removal results, over 98% removal, were obtained as well as interesting magnetic properties. For this type of material, it is also important to consider the photostability of the catalyst in view of its reuse. In a study about the reuse of Fe/TiO_2 magnetic photocatalysts in the photoreduction of selenium ions, Fuziki et al. (2020) observed a reduction in the efficiency of the photocatalyst only in the fourth photocatalytic cycle, going from about 98% removal in the first cycle to approximately 60% at the end of the fourth cycle (Fuziki et al. 2020). The catalyst $TiO_2/CoFe_2O_4$ satisfactorily preserved its photocatalytic activity even after 5 photocatalytic cycles, decreasing from about 99% in the first cycle to 96.5% at the end of the fifth cycle (Fuziki et al. 2021).

PHOTOCATALYTIC OXIDATION PROCESSES

Arsenium Oxidation

Arsenic (As) is a metalloid (atomic number 33, belonging to Group 5A), whose oxidation states vary between -3, 0, +3 and +5. It is found naturally in the earth's crust, mainly in the form of sulphides, given the great affinity of As for sulphur, and also as arsenate or metallic arsenides. In water, it is predominantly found in the form of arsenite [As(III)] and arsenate [As(V)] ions (Figure 6), commonly existing in natural waters as $As(OH)_3$ (pKa=9.2) and H_3AsO_4 (pKa = 2.22, 6.98, 11.53), respectively

(WHO 2017; National Research Council (U.S.). 1999; T. V. Nguyen et al. 2008; Guan et al. 2012).

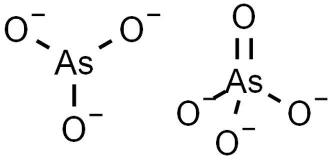

Figure 6. Arsenite (As(III), left) and arsenate (As(V),right) ions.
Source: Royal Society of Chemistry (2019) (Royal Society of Chemistry 2019).

Arsenite and arsenate present different mobility and toxicity levels. In aqueous medium, As(III) ions tend to be more mobile than the As(V) ions, while As(V) presents higher affinity for adsorption on mineral surfaces, particularly on those containing Fe(III) (WHO 2017; National Research Council (U.S.). 1999; T. V. Nguyen et al. 2008; Guan et al. 2012). Regarding the toxicity, arsenite is considered to be more toxic than the pentavalent form. Thus, one of the strategies for removing arsenic from the aqueous medium consists of As(III) oxidation to As(V), which is easier to remove from water, either by adsorption, precipitation or ion exchange (Fontana, Lenzi, et al. 2018).

Heterogeneous photocatalysis is an efficient methodology capable of promoting arsenic oxidation, as already demonstrated by some works in the field (Table 3).

Studies have shown that it is also possible to reduce As(V) to As(III) through photocatalysis by using electron donors or hole scavengers (Samad et al. 2018). Levy et al. (2012) were even able to produce As(0) and AsH_3 by photoreduction of As(III) and As(V), using methanol as an electron donor. The authors emphasize, however, that despite the advantages of recovering arsenic in the As(0) form, photoreduction involves the formation of AsH_3, one of the most toxic forms of arsenic (Levy et al. 2012). For this reason, it is preferable to promote the photocatalytic oxidation of arsenic.

Nguyen et al. (T. V. Nguyen et al. 2008) observed experimentaly how quickly As(III) is oxidized to As(V), having obtained about 98% of As(III) removal from an initial concentration solution of 500µg L^{-1} of arsenite, using a catalyst concentration of 0.5 g L^{-1} at pH=6.7 (T. V. Nguyen et al. 2008).

Table 3. Some photocatalytic processes applied to arsenic removal described in the literature

Photocatalyst	Operational conditions	Removal / Main results	Year	Ref.
TiO_2 P25 (0.1 g L^{-1})	Mercury vapor lamp (125 W) 200 µM de As(III) pH = 3 – 9 (no relevance) Air equilibrated	Oxidation 100% (15 min)	2005	(Dutta et al. 2005)
TiO_2 P25 (0.01 g L^{-1})	UV lamp (11 W) 100 µg L^{-1} de As(III) pH = 6.7	80% (10 min) 95% (240 min)	2008	(T. V. Nguyen et al. 2008)
TiO_2 Commercial (0.1 g L^{-1})	Mercury vapor lamp (250 W) 200 µg L^{-1} de As(III) pH = 7 Air bubling	97% (60 min) 90% (20 min photolysis) 72% (contínuous flow photolysis, 5 ml min^{-1})	2018	(Fontana, Lenzi, et al. 2018)

Dutta et al. (Dutta et al. 2005) studied the photocatalytic oxidation of As(III) and obtained satisfactory results, with final As concentrations lower than the limit determined by the WHO. According to the authors, photo-oxidation occurs quickly, in a matter of minutes, following zero-order kinetics. It was possible to identify, from the results, the important role played by hydroxyl radicals in the As(III) photo-oxidation mechanism, forming As(V), which is removed from the medium by adsorption on the TiO_2 surface.

Dutta et al. (Dutta et al. 2005) also studied the effect of some operational conditions on As(III) oxidation. They compared the use of N_2, O_2 and air in photocatalytic tests, observing that in absence of O_2 (N_2 purging), the oxidation rate decreased considerably. However, the use of pure O_2 did not show a significant improvement in relation to air, so authors concluded that the use of atmospheric air was sufficient to promote As(III) oxidation. Wang et al. (Z. Wang, Murugananthan, and Zhang 2019) identified $O_2^{\bullet -}$ radicals as being the main active species in As(III) oxidation. In photocatalytic tests using G-C_2N_4 as photocatalyst and in the presence of O_2 in abundance there was a significant increase in the reaction rate. In N_2 atmosphere, on the other hand, the authors noticed that As(III) oxidation decreased from 100% to 67%.

As for the effect of pH, within the range studied (pH=3 to pH=9), Dutta et al. (Dutta et al. 2005) did not detect a strong impact of this factor on As removal (Dutta et al. 2005). Fontana et al. (Fontana, Lenzi, et al. 2018), also tested different pH values for arsenic oxidation (3, 7 and 9) and did not observed significant effect of this parameter on As(III) oxidation after 15 min of photocatalysis. According to Fontana et al. (Fontana, Lenzi, et al. 2018), As(III) species are in the neutral form in pH between 3 and 9, so that no significant differences in electrostatic attraction between Ad(III) and the photocatalyst surface were observed.

Besides that, when studying the photo-oxidation of arsenic, using different forms of TiO_2 and comparing the photocatalysis and photolysis processes, Fontana et al. (Fontana, Lenzi, et al. 2018) did not observe significant differences in removal with (97% removal) and without the presence of the catalyst (90% removal), nor impact of different structures (Fontana, Lenzi, et al. 2018). Yu et al. (Yu et al. 2013), on the other hand, did not observed a significant reduction in As(III) concentration when only UV radiation was applied without catalyst.

Fontana et al. (Fontana, Lenzi, et al. 2018) have also studied the effect of different aqueous matrices (ultrapure water, river water, well water and tap water) on arsenite oxidation, not observing any significant change. Ma and Tu (2011) performed an interesting study on the adsorption of As(III) and As(V) on TiO_2, and found that the constituent phase of titanium dioxide (anatase or rutile) affects the adsorption process (Ma and Tu 2011). The relevance of this study lies in the key role played by adsorption in the heterogeneous photocatalysis process, as well as by the removal of As(V) by adsorption on TiO_2, pointed out by Dutta et al. (Dutta et al. 2005).

Some works have already described the use of magnetic photocatalysts in arsenite oxidation, with a predominance of iron oxide-based composites, such as Fe_3O_4@TiO_2 used in As(III) oxidation followed by adsorption

(Deng et al. 2019), or even the TiO_2 composite/PTh/γ-Fe2O3 (Liu et al. 2021) and the particles with core-shell structure Fe_3O_4@PpPDA @TiO_2 (Y. Wang et al. 2020), both used in the oxidation and adsorption of As(III).

REFERENCES

Aman, Noor, T. Mishra, J. Hait, and R. K. Jana. 2011. “Simultaneous Photoreductive Removal of Copper (II) and Selenium (IV) under Visible Light over Spherical Binary Oxide Photocatalyst.” *Journal of Hazardous Materials* 186 (1): 360–66. https://doi.org/10.1016/j.jhazmat.2010.11.001.

Arfanis, Michalis K., Panagiota Adamou, Nikolaos G. Moustakas, Theodoros M. Triantis, Athanassios G. Kontos, and Polycarpos Falaras. 2017. “Photocatalytic Degradation of Salicylic Acid and Caffeine Emerging Contaminants Using Titania Nanotubes.” *Chemical Engineering Journal* 310 (February): 525–36. https://doi.org/10.1016/j.cej.2016.06.098.

Bernabeu, A., R. F. Vercher, L. Santos-Juanes, P. J. Simón, C. Lardín, M. A. Martínez, J. A. Vicente, et al. 2011. “Solar Photocatalysis as a Tertiary Treatment to Remove Emerging Pollutants from Wastewater Treatment Plant Effluents.” *Catalysis Today* 161 (1): 235–40. https://doi.org/10.1016/j.cattod.2010.09.025.

Bertinetti, Stefano, Marco Minella, Francesco Barsotti, Valter Maurino, Claudio Minero, Emrah Özensoy, and Davide Vione. 2016. “A Methodology to Discriminate between Hydroxyl Radical-Induced Processes and Direct Charge-Transfer Reactions in Heterogeneous Photocatalysis.” *Journal of Advanced Oxidation Technologies* 19 (2): 236–45. https://doi.org/10.1515/jaots-2016-0207.

Bora, Leena V., and Rajubhai K. Mewada. 2017. “Visible/Solar Light Active Photocatalysts for Organic Effluent Treatment: Fundamentals, Mechanisms and Parametric Review.” *Renewable and Sustainable Energy Reviews* 76 (September): 1393–1421. https://doi.org/10.1016/j.rser.2017.01.130.

Byrne, Ciara, Gokulakrishnan Subramanian, and Suresh C. Pillai. 2018. "Recent Advances in Photocatalysis for Environmental Applications." *Journal of Environmental Chemical Engineering* 6 (3): 3531–55. https://doi.org/10.1016/j.jece.2017.07.080.

Chen, Dingwang, and Ajay K. Ray. 2001. "Removal of Toxic Metal Ions from Wastewater by Semiconductor Photocatalysis." *Chemical Engineering Science* 56 (4): 1561–70. https://doi.org/10.1016/S0009-2509(00)00383-3.

Cordoba, Patricia, and Lucian C Staicu. 2018. "Flue Gas Desulfurization Effluents: An Unexploited Selenium Resource." *Fuel* 223 (July): 268–76. https://doi.org/10.1016/j.fuel.2018.03.052.

Corrigan, Nathaniel, Sivaprakash Shanmugam, Jiangtao Xu, and Cyrille Boyer. 2016. "Photocatalysis in Organic and Polymer Synthesis." *Chemical Society Reviews* 45 (22): 6165–6212. https://doi.org/10.1039/c6cs00185h.

Deng, Min, Xiaodong Wu, Aimei Zhu, Qiugen Zhang, and Qinglin Liu. 2019. "Well-Dispersed TiO 2 Nanoparticles Anchored on Fe 3 O 4 Magnetic Nanosheets for Efficient Arsenic Removal." *Journal of Environmental Management* 237 (January): 63–74. https://doi.org/10.1016/j.jenvman.2019.02.037.

Duffus, John H. 2002. "'heavy Metals' - A Meaningless Term? (IUPAC Technical Report)." *Pure and Applied Chemistry* 74 (5): 793–807. https://doi.org/10.1351/pac200274050793.

Dutta, Paritam K., S. O. Pehkonen, Virender K. Sharma, and Ajay K. Ray. 2005. "Photocatalytic Oxidation of Arsenic(III): Evidence of Hydroxyl Radicals." *Environmental Science & Technology* 39 (6): 1827–34. https://doi.org/10.1021/es0489238.

Farrokhi, Alireza, Fahimeh Feizpour, and Maryam Asaadzadeh. 2019. "Degradation of Hazardous Organic Dyes with Solar-driven Advanced Oxidation Process Catalyzed by the Mixed Metal–Organic Frameworks." *Applied Organometallic Chemistry*, no. November 2018 (April): e4928. https://doi.org/10.1002/aoc.4928.

Fontana, Klaiani B., Eduardo S. Chaves, Vitor Sena Kosera, and Giane G. Lenzi. 2018. "Barium Removal by Photocatalytic Process: An

Alternative for Water Treatment." *Journal of Water Process Engineering* 22 (January): 163–71. https://doi.org/10.1016/j.jwpe.2018.01.017.

Fontana, Klaiani B., Giane G. Lenzi, Eriton C. R. Seára, and Eduardo S. Chaves. 2018. "Comparision of Photocatalysis and Photolysis Processes for Arsenic Oxidation in Water." *Ecotoxicology and Environmental Safety* 151 (September 2017): 127–31. https://doi.org/10.1016/j.ecoenv.2018.01.001.

Fuziki, Maria Eduarda Kounaris, E. Abreu, A. E. De Carvalho, L. H. B. O. Silva, M. Z. Fidelis, Angelo M. Tusset, R. Brackmann, D. T. Dias, and G. G. Lenzi. 2020. "Sol–Gel Fe/TiO2 Magnetic Catalysts Applied to Selenium Photoreduction." *Topics in Catalysis*, no. 0123456789 (May). https://doi.org/10.1007/s11244-020-01276-1.

Fuziki, Maria Eduarda Kounaris, R. Brackmann, D. T. Dias, A. M. Tusset, S. Specchia, and G. G. Lenzi. 2021. "Effects of Synthesis Parameters on the Properties and Photocatalytic Activity of the Magnetic Catalyst TiO2/CoFe2O4 Applied to Selenium Photoreduction." *Journal of Water Process Engineering* 42 (March): 102163. https://doi.org/10.1016/j.jwpe.2021.102163.

Gouvêa, Carlos A. K., Fernando Wypych, Sandra G. Moraes, Nelson Durán, Noemi Nagata, and Patricio Peralta-Zamora. 2000. "Semiconductor-Assisted Photocatalytic Degradation of Reactive Dyes in Aqueous Solution." *Chemosphere* 40 (4): 433–40. https://doi.org/10.1016/S0045-6535(99)00313-6.

Guan, Xiaohong, Juanshan Du, Xiaoguang Meng, Yuankui Sun, Bo Sun, and Qinghai Hu. 2012. "Application of Titanium Dioxide in Arsenic Removal from Water: A Review." *Journal of Hazardous Materials*. https://doi.org/10.1016/j.jhazmat.2012.02.069.

He, Yangzhuo, Yujia Xiang, Yaoyu Zhou, Yuan Yang, Jiachao Zhang, Hongli Huang, Cui Shang, Lin Luo, Jun Gao, and Lin Tang. 2018. "Selenium Contamination, Consequences and Remediation Techniques in Water and Soils: A Review." *Environmental Research* 164 (July): 288–301. https://doi.org/10.1016/j.envres.2018.02.037.

Holmes, Andrew B., Aldrich Ngan, Jane Ye, and Frank Gu. 2021. "Selective Photocatalytic Reduction of Selenate over TiO2 in the Presence of Nitrate and Sulfate in Mine-Impacted Water." *Chemosphere* 287 (P1): 131951. https://doi.org/10.1016/j.chemosphere.2021.131951.

HUANG, Shunsheng, Ming HUA, Jinshun FENG, Xinyong ZHONG, Yang JIN, Baiwan ZHU, and Hua LU. 2009. "Assessment of Selenium Pollution in Agricultural Soils in the Xuzhou District, Northwest Jiangsu, China." *Journal of Environmental Sciences* 21 (4): 481–87. https://doi.org/10.1016/S1001-0742(08)62295-0.

Hwang, Seon Wook, Hyun Jae Lee, Kee Suck Suh, Sang Tae Kim, Sung Wook Park, Dae Young Hur, Deborah Lee, Jong Keun Seo, and Ho Suk Sung. 2011. "Changes in Murine Hair with Dietary Selenium Excess or Deficiency." *Experimental Dermatology* 20 (4): 367–69. https://doi.org/10.1111/j.1600-0625.2010.01207.x.

Kabra, Kavita, Rubina Chaudhary, and R. L. Sawhney. 2007. "Effect of PH on Solar Photocatalytic Reduction and Deposition of Cu(II), Ni(II), Pb(II) and Zn(II): Speciation Modeling and Reaction Kinetics." *Journal of Hazardous Materials* 149 (3): 680–85. https://doi.org/10.1016/j.jhazmat.2007.04.028.

——. 2008. "Solar Photocatalytic Removal of Cu(II), Ni(II), Zn(II) and Pb(II): Speciation Modeling of Metal-Citric Acid Complexes." *Journal of Hazardous Materials* 155 (3): 424–32. https://doi.org/10.1016/j.jhazmat.2007.11.083.

Kanakaraju, Devagi, Nurfatyha Rusydah, Ying-chin Lim, and Andrea Pace. 2019. "Concurrent Removal of Cr (III), Cu (II), and Pb (II) Ions from Water by Multifunctional TiO 2/Alg/FeNPs Beads." *Sustainable Chemistry and Pharmacy* 14 (September): 100176. https://doi.org/10.1016/j.scp.2019.100176.

Karthikeyan, C., Prabhakarn Arunachalam, K. Ramachandran, Abdullah M. Al-Mayouf, and S. Karuppuchamy. 2020. "Recent Advances in Semiconductor Metal Oxides with Enhanced Methods for Solar Photocatalytic Applications." *Journal of Alloys and Compounds* 828 (March): 154281. https://doi.org/10.1016/j.jallcom.2020.154281.

Kumar, S. Girish, and L. Gomathi Devi. 2011. "Review on Modified TiO_2 Photocatalysis under UV/Visible Light: Selected Results and Related Mechanisms on Interfacial Charge Carrier Transfer Dynamics." *Journal of Physical Chemistry A* 115 (46): 13211–41. https://doi.org/10.1021/jp204364a.

la Cruz, N. De, J. Giménez, S. Esplugas, D. Grandjean, L. F. de Alencastro, and C. Pulgarín. 2012. "Degradation of 32 Emergent Contaminants by UV and Neutral Photo-Fenton in Domestic Wastewater Effluent Previously Treated by Activated Sludge." *Water Research* 46 (6): 1947–57. https://doi.org/10.1016/j.watres.2012.01.014.

Lemly, A. Dennis. 2004. "Aquatic Selenium Pollution Is a Global Environmental Safety Issue." *Ecotoxicology and Environmental Safety* 59 (1): 44–56. https://doi.org/10.1016/S0147-6513(03)00095-2.

Lemly, A. Dennis. 2018. "Selenium Poisoning of Fish by Coal Ash Wastewater in Herrington Lake, Kentucky." *Ecotoxicology and Environmental Safety* 150 (April): 49–53. https://doi.org/10.1016/j.ecoenv.2017.12.013.

Levy, Ivana K., Martín Mizrahi, Gustavo Ruano, Guillermo Zampieri, Félix G. Requejo, and Marta I. Litter. 2012. "TiO 2-Photocatalytic Reduction of Pentavalent and Trivalent Arsenic: Production of Elemental Arsenic and Arsine." *Environmental Science and Technology* 46 (4): 2299–2308. https://doi.org/10.1021/es202638c.

Linsebigler, Amy L., Guangquan Lu, and John T. Yates. 1995. "Photocatalysis on TiO_2 Surfaces: Principles, Mechanisms, and Selected Results." *Chemical Reviews* 95 (3): 735–58. https://doi.org/10.1021/cr00035a013.

Liu, Xuemei, Yuan Wang, Tian C. Zhang, Gang Xiang, Xinlong Wang, and Shaojun Yuan. 2021. "One-Pot Synthesis of a Magnetic TiO2/PTh/γ-Fe2O3Heterojunction Nanocomposite for Removing Trace Arsenite via Simultaneous Photocatalytic Oxidation and Adsorption." *Industrial and Engineering Chemistry Research* 60 (1): 528–40. https://doi.org/10.1021/acs.iecr.0c04262.

Ma, L., and S. X. Tu. 2011. “Removal of Arsenic from Aqueous Solution by Two Types of Nano TiO2 Crystals.” *Environmental Chemistry Letters* 9 (4): 465–72. https://doi.org/10.1007/s10311-010-0303-1.

Majidnia, Zohreh, and Mohamad Ali Fulazzaky. 2016. “Photoreduction of Pb(II) Ions from Aqueous Solution by Titania Polyvinylalcohol–Alginate Beads.” *Journal of the Taiwan Institute of Chemical Engineers* 66: 88–96. https://doi.org/10.1016/j.jtice.2016.05.024.

Mamaghani, Alireza Haghighat, Fariborz Haghighat, and Chang Seo Lee. 2018. “Photocatalytic Degradation of VOCs on Various Commercial Titanium Dioxides: Impact of Operating Parameters on Removal Efficiency and by-Products Generation.” *Building and Environment* 138 (June): 275–82. https://doi.org/10.1016/j.buildenv.2018.05.002.

Mishra, T., J. Hait, Noor Aman, R. K. Jana, and S. Chakravarty. 2007. “Effect of UV and Visible Light on Photocatalytic Reduction of Lead and Cadmium over Titania Based Binary Oxide Materials.” *Journal of Colloid and Interface Science* 316 (1): 80–84. https://doi.org/10.1016/j.jcis.2007.08.037.

Murruni, Leonardo, Flavio Conde, Gabriela Leyva, and Marta I. Litter. 2008. “Photocatalytic Reduction of Pb(II) over TiO2: New Insights on the Effect of Different Electron Donors.” *Applied Catalysis B: Environmental* 84 (3–4): 563–69. https://doi.org/10.1016/j.apcatb.2008.05.012.

Murruni, Leonardo, Gabriela Leyva, and Marta I. Litter. 2007. “Photocatalytic Removal of Pb(II) over TiO2 and Pt-TiO2 Powders.” *Catalysis Today* 129 (1-2 SPEC. ISS.): 127–35. https://doi.org/10.1016/j.cattod.2007.06.058.

National Research Council (U.S.). 1999. *Arsenic in Drinking Water. Arsenic in Drinking Water*.

Nguyen, Chi Hieu, Chun-Chieh Fu, and Ruey-Shin Juang. 2018. “Degradation of Methylene Blue and Methyl Orange by Palladium-Doped TiO_2 Photocatalysis for Water Reuse: Efficiency and Degradation Pathways.” *Journal of Cleaner Production* 202 (November): 413–27. https://doi.org/10.1016/j.jclepro.2018.08.110.

Nguyen, T. V., S. Vigneswaran, H. H. Ngo, J. Kandasamy, and H. C. Choi. 2008. "Arsenic Removal by Photo-Catalysis Hybrid System." *Separation and Purification Technology* 61 (1): 44–50. https://doi.org/10.1016/j.seppur.2007.09.015.

Nguyen, Vi Nu Hoai, Rose Amal, Donia Beydoun, Vi Nu Hoai Nguyen, Rose Amal, and Donia Beydoun. 2005. "Photocatalytic Reduction of Selenium Ions Using Different TiO2 Photocatalysts." *Chemical Engineering Science* 60 (21): 5759–69. https://doi.org/10.1016/j.ces.2005.04.085.

Nguyen, Vi Nu Hoai, Donia Beydoun, and Rose Amal. 2005. "Photocatalytic Reduction of Selenite and Selenate Using TiO_2 Photocatalyst." *Journal of Photochemistry and Photobiology A: Chemistry* 171 (2): 113–20. https://doi.org/10.1016/j.jphotochem.2004.09.015.

Nishikawa, Harumitsu, and Yasumitsu Takahara. 2001. "Adsorption and Photocatalytic Decomposition of Odor Compounds Containing Sulfur Using TiO2/SiO2 Bead." *Journal of Molecular Catalysis A: Chemical* 172 (1–2): 247–51. https://doi.org/10.1016/S1381-1169(01)00124-8.

Nogueira, Raquel F. P., and Wilson F. Jardim. 1998. "A Fotocatálise Heterogênea e Sua Aplicação Ambiental." *Química Nova* 21 (1): 69–72. https://doi.org/10.1590/s0100-40421998000100011.

Peter, Anca, Anca Mihaly-Cozmuta, Camelia Nicula, and Leonard Mihaly-Cozmuta. 2017. "Assessment of TiO2 Photoactivity on the Lead Removal: Kinetic and Mechanistic Processing." *Water Science and Technology* 75 (11): 2508–19. https://doi.org/10.2166/wst.2017.133.

Prabhu, K. Sandeep, and Xin Gen Lei. 2016. "Selenium." *Advances in Nutrition* 7 (2): 415–17. https://doi.org/10.3945/an.115.010785.

Prado, Alexandre G.S., Lucas B. Bolzon, Carolina P. Pedroso, Aline O. Moura, and Leonardo L. Costa. 2008. "Nb2O5 as Efficient and Recyclable Photocatalyst for Indigo Carmine Degradation." *Applied Catalysis B: Environmental* 82 (3–4): 219–24. https://doi.org/10.1016/j.apcatb.2008.01.024.

Prairie, Michael R., Lindsey R. Evans, Bertha M. Stange, and Sheryl L. Martinez. 1993. "An Investigation of Titanium Dioxide Photocatalysis for the Treatment of Water Contaminated with Metals and Organic Chemicals." *Environmental Science & Technology* 27 (9): 1776–82. https://doi.org/10.1021/es00046a003.

Rajh, Tijana, Agnes E. Ostafin, Olga I. Micic, David M. Tiède, and Marion C. Thurnauer. 1996. "Surface Modification of Small Particle Tich Colloids with Cysteine for Enhanced Photochemical Reduction: An EPR Study." *Journal of Physical Chemistry* 100 (11): 4538–45. https://doi.org/10.1021/jp952002p.

Royal Society of Chemistry. 2019. *ChemSpider - Structure Search*. 2019.

Samad, Abdus, Shamim Ahsan, Ikki Tateishi, Mai Furukawa, Hideyuki Katsumata, Tohru Suzuki, and Satoshi Kaneco. 2018. "Indirect Photocatalytic Reduction of Arsenate to Arsenite in Aqueous Solution with TiO2 in the Presence of Hole Scavengers." *Chinese Journal of Chemical Engineering* 26 (3): 529–33. https://doi.org/10.1016/j.cjche.2017.05.019.

Singh, Gurpreet, Moolchand Sharma, and Rahul Vaish. 2021. "Emerging Trends in Glass-Ceramic Photocatalysts." *Chemical Engineering Journal* 407 (July 2020): 126971. https://doi.org/10.1016/j.cej.2020.126971.

Skerfving, Staffan, and Ingvar A. Bergdahl. 2015. *Lead. Handbook on the Toxicology of Metals: Fourth Edition*. Fourth Edi. Vol. 1. Elsevier. https://doi.org/10.1016/B978-0-444-59453-2.00043-3.

Srivastava, N. K., and C. B. Majumder. 2008. "Novel Biofiltration Methods for the Treatment of Heavy Metals from Industrial Wastewater." *Journal of Hazardous Materials* 151 (1): 1–8. https://doi.org/10.1016/j.jhazmat.2007.09.101.

Tan, Hui Ling, Fatwa F. Abdi, and Yun Hau Ng. 2019. "Heterogeneous Photocatalysts: An Overview of Classic and Modern Approaches for Optical, Electronic, and Charge Dynamics Evaluation." *Chemical Society Reviews* 48 (5): 1255–71. https://doi.org/10.1039/c8cs00882e.

Tan, Lea Chua, Yarlagadda V Nancharaiah, Eric D. van Hullebusch, and Piet N. L. Lens. 2016. "Selenium: Environmental Significance, Pollution, and Biological Treatment Technologies." *Biotechnology Advances* 34 (5): 886–907. https://doi.org/10.1016/j.biotechadv.2016.05.005.

Tan, T. T. Y., C. K. Yip, D. Beydoun, and R. Amal. 2003. "Effects of Nano-Ag Particles Loading on TiO2 Photocatalytic Reduction of Selenate Ions." *Chemical Engineering Journal* 95 (1–3): 179–86. https://doi.org/10.1016/S1385-8947(03)00103-7.

Tan, T., D. Beydoun, and R. Amal. 2003. "Effects of Organic Hole Scavengers on the Photocatalytic Reduction of Selenium Anions." *Journal of Photochemistry and Photobiology A: Chemistry* 159 (3): 273–80. https://doi.org/10.1016/S1010-6030(03)00171-0.

Tan, Timothy T. Y., Myint Zaw, Donia Beydoun, and Rose Amal. 2002. "The Formation of Nano-Sized Selenium-Titanium Dioxide Composite Semiconductors by Photocatalysis." *Journal of Nanoparticle Research* 4 (6): 541–52. https://doi.org/10.1023/A:1022858409731.

Tan, Timothy T. Y., Donia Beydoun, and Rose Amal. 2003. "Photocatalytic Reduction of Se(VI) in Aqueous Solutions in UV/TiO2 System: Importance of Optimum Ratio of Reactants on TiO2 Surface." *Journal of Molecular Catalysis A: Chemical* 202 (1–2): 73–85. https://doi.org/10.1016/S1381-1169(03)00205-X.

Tanaka, K., K. Harada, and S. Murata. 1986. "Photocatalytic Deposition of Metal Ions onto TiO2 Powder." *Solar Energy* 36 (2): 159–61. https://doi.org/10.1016/0038-092X(86)90121-0.

Teixeira, Cláudia Poli De Almeida Barêa, and Wilson De Figueiredo Jardim. 2004. "Processos Oxidativos Avançados: Conceitos Teóricos. Campinas, SP: Universidade Estadual de Campinas (UNICAMP), 2004, v. 3, 83 P." *Caderno Temático* 03: 83. [Advanced Oxidative Processes: Theoretical Concepts. Campinas, SP: State University of Campinas (UNICAMP), 2004, v. 3, 83 P. *Thematic Notebook*]

Thurnauer, Marion C., Tijana Rajh, David M. Tiede, Prasad S. Lakkaraju, Antonio Sousa, Alexander D. Garnovskii, D. A. Garnovskii, Björn O.

Roos, Claire Vallance, and Bryan R. Wood. 1997. "Surface Modification of TiO2: Correlation between Structure, Charge Separation and Reduction Properties." *Acta Chemica Scandinavica* 51 (5): 610–18. https://doi.org/10.3891/acta.chem.scand.51-0610.

Torres-Vega, Adriana, Bernardo F. Pliego-Rivero, Gloria A. Otero-Ojeda, Leobardo M. Gómez-Oliván, and Patricia Vieyra-Reyes. 2012. "Limbic System Pathologies Associated with Deficiencies and Excesses of the Trace Elements Iron, Zinc, Copper, and Selenium." *Nutrition Reviews* 70 (12): 679–92. https://doi.org/10.1111/j.1753-4887.2012.00521.x.

Torres, J., and S. Cervera-March. 1992. "Kinetics of the Photoassisted Catalytic Oxidation of Pb(II) in TiO2 Suspensions." *Chemical Engineering Science* 47 (15–16): 3857–62. https://doi.org/10.1016/0009-2509(92)85134-W.

Vinceti, Marco, Paola Ballotari, Craig Steinmaus, Carlotta Malagoli, Ferdinando Luberto, Marcella Malavolti, and Paolo Giorgi Rossi. 2016. "Long-Term Mortality Patterns in a Residential Cohort Exposed to Inorganic Selenium in Drinking Water." *Environmental Research* 150 (October): 348–56. https://doi.org/10.1016/j.envres.2016.06.009.

Vinceti, Marco, Francesca Bonvicini, Kenneth J. Rothman, Luciano Vescovi, and Feiyue Wang. 2010. "The Relation between Amyotrophic Lateral Sclerosis and Inorganic Selenium in Drinking Water: A Population-Based Case-Control Study." *Environmental Health* 9 (1): 77. https://doi.org/10.1186/1476-069X-9-77.

Vinceti, Marco, Massimo Vicentini, Lauren A. Wise, Claudio Sacchettini, Carlotta Malagoli, Paola Ballotari, Tommaso Filippini, Marcella Malavolti, and Paolo Giorgi Rossi. 2018. "Cancer Incidence Following Long-Term Consumption of Drinking Water with High Inorganic Selenium Content." *Science of The Total Environment* 635 (September): 390–96. https://doi.org/10.1016/j.scitotenv.2018.04.097.

Wang, N., J. Yang, and H. He. 2011. “A Novel Two-Step Method to Synthesize Lotus-Leaf-Structured TiO_2 Nanocrystals with Good Photocatalytic Activity.” *Powder Technology* 3: 744–46.

Wang, Yuan, Yan Zhang, Tian C. Zhang, Gang Xiang, Xinlong Wang, and Shaojun Yuan. 2020. “Removal of Trace Arsenite through Simultaneous Photocatalytic Oxidation and Adsorption by Magnetic Fe3O4@PpPDA@TiO2Core-Shell Nanoparticles.” *ACS Applied Nano Materials* 3 (8): 8495–8504. https://doi.org/10.1021/acsanm.0c02083.

Wang, Zhao, Muthu Murugananthan, and Yanrong Zhang. 2019. “Graphitic Carbon Nitride Based Photocatalysis for Redox Conversion of Arsenic(III) and Chromium(VI) in Acid Aqueous Solution.” *Applied Catalysis B: Environmental* 248 (December 2018): 349–56. https://doi.org/10.1016/j.apcatb.2019.02.041.

WHO. 2017. *Guidelines for Drinking-water Quality*.

WHO, World Health Organization. 2011. “Lead in Drinking Water.” *Background Document for Development of WHO Guidelines for Drinking-Water Quality* ©. https://doi.org/10.2105/ajph.13.3.207.

You, Suzhen, Yun Hu, Xingchen Liu, and Chaohai Wei. 2018. “Synergetic Removal of Pb(II) and Dibutyl Phthalate Mixed Pollutants on Bi2O3-TiO2 Composite Photocatalyst under Visible Light.” *Applied Catalysis B: Environmental* 232 (December 2017): 288–98. https://doi.org/10.1016/j.apcatb.2018.03.025.

Yu, Lian, Xianjia Peng, Fan Ni, Jin Li, Dongsheng Wang, and Zhaokun Luan. 2013. “Arsenite Removal from Aqueous Solutions by γ-Fe2O3-TiO2 Magnetic Nanoparticles through Simultaneous Photocatalytic Oxidation and Adsorption.” *Journal of Hazardous Materials* 246–247: 10–17. https://doi.org/10.1016/j.jhazmat.2012.12.007.

Zhao, Xuesong, Guan Zhang, and Zhenghua Zhang. 2020. “TiO2-Based Catalysts for Photocatalytic Reduction of Aqueous Oxyanions: State-of-the-Art and Future Prospects.” *Environment International* 136 (October 2019). https://doi.org/10.1016/j.envint.2019.105453.

Zhou, Ji-Chang, Shijie Zheng, Junluan Mo, Xiongshun Liang, Yuanfei Xu, Huimin Zhang, Chunmei Gong, Xiao-Li Liu, and Xin Gen Lei. 2017. "Dietary Selenium Deficiency or Excess Reduces Sperm Quality and Testicular MRNA Abundance of Nuclear Glutathione Peroxidase 4 in Rats." *The Journal of Nutrition* 147 (10): 1947–53. https://doi.org/10.3945/jn.117.252544.

BIOGRAPHICAL SKETCHES

G. G. Lenzi

Affiliation: Federal University of Technology Paraná

Education:

2008 - Doctorate in Chemical Engineering
Universidade Estadual de Maringá (UEM).
2004 - Master in Chemical Engineering
Universidade Estadual de Maringá (UEM).

Research and Professional Experience: Concentration area Chemical Processes –, Post-doctor – Politecnico di Torino (Italy). Her master's and doctoral degree involved both the thesis and the dissertation developed aiming at the production of hydrogen. Different catalysts were prepared, characterized and applied in dry-reforming as well as methane-steam reactions, generating publications in national and international journals. In the industry, the researcher worked as chemical engineer in the service provision project linked to Petrobrás/SIX, as well as coordinator to the technological development projects in partnership with the Companhia de Saneamento do Paraná SANEPAR/FUNDAÇÃO ARAUCÁRIA. Currently developing research about photocatalysis process for pollutants removal and CO_2 valorization.

Professional Appointments: Professor in Federal University of Technology – Paraná (UTFPR) and and PostGraduate Program in Chemical Engineering (PPGEQ).

Publications from the Last 3 Years:

1. Zinc oxide immobilized on alginate beads as catalyst for photocatalytic degradation of textile dyes an evaluation of matrix effects. *Desalination and Water Treatment.*
2. Process Comparison for Caffeine Degradation: Fenton, Photo-Fenton, UV/H2O2 and UV/Fe3+. Water Air and Soil Pollution.
3. Paraquat degradation by photocatalysis: experimental desing and optimization. Journal of Environmental Science and Health Part *B-Pesticides Food Contaminants and Agricultural Wastes.*
4. Effects of synthesis parameters on the properties and photocatalytic activity of the magnetic catalyst TiO2/CoFe2O4 applied to selenium photoreduction. *Journal of Water Process Engineering.*
5. Quarry Residue: Treatment of Industrial Effluent Containing Dye. *Catalysts.*
6. Generalized RBF artificial neural network applied to a reactive dyes photodiscoloration prediction problem. *Desalination and Water Treatment.*
7. Degradation of emerging contaminants: Effect of thermal treatment on Nb2O5 as photocatalyst. *Journal of Photochemistry and Photobiology A-Chemistry.*
8. Sol-gel Fe/TiO2 Magnetic Catalysts Applied to Selenium Photoreduction. *Topics in Catalysis.*
9. Discoloration of methylene blue dye using Nb2O5/UV and Nb2O5/solar systems. *Brazilian Journal of Development.*

10. Degradation of Caffeine by Heterogeneous Photocatalysis Using ZnO with Fe and Ag. *Brazilian Archives of Biology and Technology (Online).*
11. Caffeine Adsorption onto Bentonite Clay in Suspension and Immobilized. *Brazilian Brazilian Archives of Biology and Technology* (Online).
12. Continuous process applied to degradation of triclosan and 2.8-dichlorodibenzene-p-dioxin. *Environmental Science and Pollution Research.*
13. Assisted hydrothermal carbonization of agroindustrial byproducts as effective step in the production of activated carbon catalysts for wet peroxide oxidation of micro-pollutants. *Journal of Environmental Chemical Engineering.*
14. Optimization and kinetic study of biodiesel production through esterification of oleic acid applying ionic liquids as catalysts. *Fuel.*
15. Influence of Extreme Events in Electric Energy Consumption and Gross Domestic Product. *Sustainability.*
16. Experimental Design and Optimization of Triclosan and 2.8-Diclorodibenzeno-p-dioxina Degradation by the Fe/Nb2O5/UV System. *Catalysts.*
17. Analysis of carbon monoxide production in methanol steam reforming reactor for generating hydrogen. Acta Scientiarum. *Technology* (Online).
18. Characterization-Performance of ZnO AND ZnO/ZnFe2O4 Catalyst Using Artificial and Solar Light for Mercury (II) Reduction. *Brazilian Journal of Chemical Engineering.*

L. N. B. Almeida

Affiliation: State University of Maringá

Education:

Actual- Doctorate in Chemical Engineering
Universidade Estadual de Maringá (UEM).

2017 - Master in Chemical Engineering
Universidade Estadual de Maringá (UEM).

Research and Professional Experience: Has experience in degradation of emerging pollutants, in particular, caffeine and dyes and catalyst synthesis.

Publications from the Last 3 Years:

1. Process Comparison for Caffeine Degradation: Fenton, Photo-Fenton, UV/H_2O_2 and UV/Fe^{3+}. *Water Air and Soil Pollution.*
2. Quarry Residue: Treatment of Industrial Effluent Containing Dye. *Catalysts.*
3. Cr (VI) reduction by photocatalyic process: Nb_2O_5 an alternative catalyst. *Journal of Environmental Management.*
4. Degradation of Caffeine by Heterogeneous Photocatalysis Using ZnO with Fe and Ag. *Brazilian Archives of Biology and Technology.*
5. Continuous process applied to degradation of triclosan and 2.8-dichlorodibenzene-p-dioxin. *Environmental Science and Pollution Research.*
6. Model Drude applied in ionic solutions. Mathematics In Engineering, Science and Aerospace: *The Transdisciplinary International Journal.*
7. Caffeine degradation using ZnO and Ag/ZnO under UV and Solar radiation. *Desalination and Water Treatment.*
8. Degradation of Caffeine by Heterogeneous Photocatalysis Using TiO_2 Impregnated with Fe and Ag. *Chemical Engineering Transactions.*

9. Study of the Biosorption Equilibrium of the Yellow Dye Reafix B2R by Sugarcane Bagasse. *Chemical Engineering Transactions.*

T. G. Josué

Affiliation: Federal University of Technology Paraná

Education:

Actual- Doctorate in Chemical Engineering
Universidade Estadual de Maringá (UEM).
2021 - Master in Chemical Engineering
Universidade Tecnológica Federal do Paraná (UTFPR).

Research and Professional Experience: Has experience in the metals reduction by photocatalysis and degradation pollutants.

Publications from the Last 3 Years:

1. Process Comparison for Caffeine Degradation: Fenton, Photo-Fenton, UV/H_2O_2 and UV/Fe^{3+}. *Water air and soil pollution.*
2. Quarry Residue: Treatment of Industrial Effluent Containing Dye. *Catalysts.*
3. Cr (VI) reduction by photocatalyic process: Nb_2O_5 an alternative catalyst. *Journal of environmental management.*
4. Continuous process applied to degradation of triclosan and 2.8-dichlorodibenzene-p-dioxin. *Environmental science and pollution research.*
5. Study of the Biosorption Equilibrium of the Yellow Dye Reafix B2R by Sugarcane Bagasse. *Chemical engineering transactions.*

M. E. K. Fuziki

Affiliation: State University of Maringá

Education:

Actual - Doctorate in Chemical Engineering
Universidade Estadual de Maringá (UEM).
2019 - Master in Chemical Engineering
Universidade Tecnológica Federal do Paraná (UTFPR).

Research and Professional Experience: Has experience in Chemical Engineering, catalysts synthesis and polluents degradation by different processes.

Publications from the Last 3 Years:

1. Degradation of emerging contaminants: Effect of thermal treatment on nb2o5 as photocatalyst. *Journal of Photochemistry and Photobiology A-Chemistry.*
2. Effects of synthesis parameters on the properties and photocatalytic activity of the magnetic catalyst TiO2/CoFe2O4 applied to selenium photoreduction. *Journal of Water Process Engineering.*
3. Sol-gel Fe/TiO2 Magnetic Catalysts Applied to Selenium Photoreduction. *Topics in catalysis*
4. Caffeine Adsorption onto Bentonite Clay in Suspension and Immobilized. *Brazilian Archives of Biology and Technology* (Online)

R. Brackmann

Affiliation: Departamento de Química, Universidade Tecnológica Federal do Paraná (UTFPR), Via do Conhecimento, Km 01, Fraron, CEP 85503-390, Pato Branco, Paraná, Brazil

Education:

2016 - Doctorate in Chemical Engineering
Universidade Federal do Rio de Janeiro (UFRJ)
2012 - Master in Chemical Engineering
Universidade Federal do Rio de Janeiro (UFRJ)

Research and Professional Experience: Rodrigo Brackmann works mainly in the area of Heterogeneous Catalysis with an emphasis on catalyst synthesis for energy and environmental applications. His main studies include the development of mixed oxides with ferrite structure for photocatalytic decontamination of wastewater, CeO_2-based mixed oxides selective catalytic reduction of NO_x, mixed oxides with perovskite structure for hydrogen production and immobilization of enzymes on different supports for applications biotechnology.

Professional Appointments: 2016-Present - Professor of the Department of Chemistry and of the Postgraduate Program in Chemical and Biochemical Process Technology (PPGTP) at the Universidade Tecnológica Federal do Paraná (UTFPR), campus Pato Branco.

Publications from the Last 3 Years:

1. Fuziki, M.E.K., Brackmann, R., Dias, D.T., Tusset, A.M., Specchia, S., Lenzi, G. G. Effects of synthesis parameters on the properties and photocatalytic activity of the magnetic catalyst $TiO_2/CoFe_2O_4$ applied to selenium photoreduction. *Journal of Water Process Engineering*, V. 42, P. 102163, 2021.

2. Lenzi, Giane G., Freitas, Paula; Fidelis, Michel Z., Ribeiro, Mauricio A., Brackmann, Rodrigo; Colpini, Leda M. S., Tusset, Angelo M. Paraquat degradation by photocatalysis: experimental desing and optimization. *Journal of Environmental Science and Health Part B-Pesticides Food Contaminants and Agricultural Wastes*, v. 56, p. 1-9, 2021.
3. Ferreira, Renata Deda Mendonca; Brackmann, Rodrigo; Pereira, Ernandes Benedito; Da Rocha, Raquel Dalla Costa. Corn Straw Residue: A Strategy for Lipase Immobilization. *Applied Biochemistry and Biotechnology*, v. 190, p. 839-850, 2020.
4. Fuziki, M. E. K., Abreu, E., De Carvalho, A. E., Silva, L. H. B. O., Fidelis, M. Z., Tusset, Angelo M., Brackmann, R., Dias, D. T., Lenzi, G. G. Sol-Gel Fe/Tio_2 Magnetic Catalysts Applied To Selenium Photoreduction. *Topics In Catalysis*, v. 1, p. 1, 2020.
5. Brackmann, Rodrigo; Alves, Odivaldo Cambraia; Woyames, Carla Brandão; Toniolo, Fabio Souza; Schmal, Martin. No reduction by CO on Ce-Fe mixed oxides and gold nanoparticles. *Applied Catalysis A-General*, v. 600, p. 117601-117612, 2020.
6. Mendonca Ferreira, Renata Deda; Brackmann, Rodrigo; Pereira, Ernandes Benedito; Costa Da Rocha, Raquel Dalla. Immobilization of lipase from *Candida rugosa* onto niobium oxide. *Biocatalysis and Agricultural Biotechnology*, v. 30, p. 101812, 2020.
7. Fidelis, M. Z., Abreu, E., Santos, O. A. A., Chaves, E. S., Brackmann, R., Rosa, D. T. D. F. Experimental Design and Optimization of Triclosan and 2.8-Diclorodibenzeno-p-dioxina Degradation by the Fe/Nb_2O_5/UV System. *Catalysts*, v. 9, p. 343-360, 2019.
8. De C. Roseno, K.T., Schmal, M., Brackmann, R., Alves, R.M.B., Giudici, R. Partial oxidation of methane on neodymium and lanthanium chromate based perovskites for hydrogen production. *International Journal of Hydrogen Energy*, v. 44, p. 8166-8177, 2019.

L. M. S. Colpini

Affiliation: Federal University of Paraná – Advanced Campus of Jandaia do Sul, Jandaia do Sul, Brazil.

Education: 2005 - Doctorate in Chemical. Universidade Estadual de Maringá (UEM).

Research and Professional Experience: Has experience in Chemistry, focusing on Inorganic Chemistry, mainly on the following subjects: sol-gel, mixed oxides, photocatalysis, biocatalysis and environmental catalysis.

Professional Appointments: Currently Associate Professor III at the Federal University of Paraná - Advanced Campus of Jandaia do Sul, working in the Undergraduate Courses in Food Engineering, Agricultural Engineering, Production Engineering and Degree in Exact Sciences. Also acting as a permanent professor in the Graduate Programs of the Federal University of Paraná - Palotina Sector: Biotechnology; Environmental Engineering and Technology.

Publications from the Last 3 Years:

1. Ferreira, Agmar, Fagnani, Kátia C., Alves, Helton J., Colpini, Leda M.S., Kunh, Sheila S., Nastri, Suelen, Conserva, Lisandra R.S., Melchiades, Fábio G. Effect of incorporating sludge from poultry slaughterhouse wastewater treatment system in ceramic mass for tile production. *Environmental Technology & Innovation*, v. 9, p. 294-302, 2018.
2. Aguiar, M., Cazula, B.B., Colpini, L.M.S., Borba, C.E., Silva, F.A., Noronha, F.B., Alves, Helton J. Si-MCM-41 obtained from different sources of silica and its application as support for nickel catalysts used in dry reforming of methane. *International Journal of Hydrogen Energy*, v. 44, p. 32003-32018, 2019.

3. Castro, Luiz Eduardo Nochi, Santos, João Victor Furlan; Fagnani, Kátia Cristina, Alves, Helton José, Colpini, Leda Maria Saragiotto. Evaluation of the effect of different treatment methods on sugarcane vinasse remediation. *Journal of Environmental Science and* Health *Part B-Pesticides Food Contaminants and Agricultural Wastes*, v. 54, p. 1-10, 2019
4. Molin Filho, Rafael Germano Dal, Colpini, Leda Maria Saragiotto, Ferrer, Mateus Meneghetti, Nagano, Marisa Fujiko, Rosso, Jaciele Márcia, Volnistem, Eduardo Azzolini, Paraíso, Paulo Roberto, De Matos Jorge, Luiz Mário. Characterization of different sugarcane bagasse ashes generated for preparation and application as green products in civil construction. *Clean Technologies and Environmental Policy*, v. 21, p. 1687-1698, 2019
5. Filho, R.G.D.M., Rosso, J.M., Volnistem, E.A., Vanderlei, R.D., Colpini, L.M.S., Ferrer, M.M., Paraíso, P.R., Jorge, L.M.M.. Sugarcane Bagasse Ash Micronized Using Air Jet Mills for Green Pozzolan in Brazil. *International Journal of Chemical Engineering*, v. 2019, p. 1-10, 2019
6. Fagnani, Kátia Cristina, Alves, Helton José, Castro, Luiz Eduardo Nochi De, Kunh, Sheila S., Colpini, Leda Maria Saragiotto. An alternative for the energetic exploitation of sludge generated in the physico-chemical effluent treatment from poultry slaughter and processing in Brazilian industries. *Journal of Environmental Chemical Engineering*, v. 7, p. 102996, 2019.
7. Castro, L.E.N., Meurer, E.C., ALVES, Helton José, Santos, M.A.R., Vasques, E.C., Colpini, L.M.S. Photocatalytic Degradation of Textile dye Orange-122 Via Electrospray Mass Spectrometry. *Brazilian Archives of Biology and Technology* (Online), v. 63, p. 1-15, 2020.
8. Colpini, L.M.S., Leal, L.R., Makuda, J.L., Nicolini, M.V.S., Abreu, E, Fidelis, M.Z., Lenzi, G.G. Descoloração do corante azul de metileno utilizando sistemas Nb2O5/UV e Nb2O5/solar. *Brazilian Journal of Development*, v. 6, p. 30859-30880, 2020.

9. Castilhos, Stefani, De Souza, Fernando Manzotti, Colpini, Leda Maria Saragiotto, De Mattos Jorge, Luiz Mario, Dos Santos, Onélia Aparecida Andreo. Assessment comparison of commercial TiO2 and TiO2 sol-gel on the degradation of caffeine using artificial radiation. *Environmental Science and Pollution Research*, v. XX, p. 1-14, 2020.
10. Lenzi, G.G., Freitas, P., Fidelis, M.Z., Ribeiro, M.A., Brackmann, R., Colpini, L.M.S., Tusset, A. Paraquat Degradation by Photocatalysis: Experimental Desing and Optimization. *Journal of Environmental Science and Health Part B-Pesticides Food Contaminants and Agricultural Wastes*, v. 56, p. 523-531, 2021.
11. Colpini, L.M.S., Souza, R.C.T., Lenzi, G.G., Neto, R.M., Santos, Onélia Aparecida Andreo dos, Jorge, L.M.M., Urio, M.B., Alves, Helton José. Generalized RBF Artificial Neural Network applied to a reactive dyes photodiscoloration prediction problem. *Desalination and Water Treatment* (Online), v. 229, p. 362-371, 2021.

A. M. Tusset

Affiliation: Federal University of Technology Paraná

Education: 2008 - Doctorate in Mechanical Engineering, Universidade Federal do Rio Grande do Sul (UFRGS)

Research and Professional Experience: Has experience in Dynamic Systems Control, acting on the following topics: SDRE Control, Chaos, Linear Feedback Control, Active Control, Passive Control, Robotics and Optimal Control.

Professional Appointments: Associate Professor at the Federal University of Technology - Paraná (UTFPR) (Brazil) and Graduate Program in Electrical Engineering (PPGEE-PG)

Publications from the Last 3 Years:

1. Lenzi, Giane G., Freitas, Paula, Fidelis, Michel Z., Ribeiro, Mauricio A., Brackmann, Rodrigo, Colpini, Leda M.S., Tusset, Angelo M. Paraquat Degradation By Photocatalysis: Experimental Desing and Optimization. *Journal of Environmental Science and Health Part B-Pesticides Food Contaminants and Agricultural Wastes*, V. 1, P. 1-9, 2021.
2. Lenz, W.B., Ribeiro, M. A., Rocha, R.T., Balthazar, J.M., Tusset, A.M. Numerical Simulations and Control of Offshore Energy Harvesting Using Piezoelectric Materials In A Portal Frame Structure. *Shock and Vibration*, V. 2021, P. 1-11, 2021.
3. Fuziki, M.E.K., Brackmann, R., Dias, D.T., Tusset, A.M., Specchia, S., Lenzi, G.G. Effects of Synthesis Parameters on The Properties and Photocatalytic Activity of the Magnetic Catalyst Tio2/Cofe2o4 Applied To Selenium Photoreduction. *Journal of Water Process Engineering*, V. 42, P. 102163, 2021.
4. Almeida, Lariana Negrão Beraldo De, Josué, Tatiana Gulminie, Nogueira, Othavio Henrique Lupepsa, Dias, Daniele Toniolo, Tusset, Angelo Marcelo, Santos, Onélia Aparecida Andreo Dos, Lenzi, Giane Gonçalves. Quarry Residue: Treatment of Industrial Effluent Containing Dye. *Catalysts*, V. 11, P. 852, 2021.
5. Manuel, Calequela J.T., Santos, Max M.D., Tusset, Angelo M. Mathematical Modeling Attributed To Kinematics and Dynamics of A Vehicle With 4-Wheels. *European Physical Journal-Special Topics*, V. 1, P. 1-10, 2021.
6. Daum, Hilson H., Tusset, Angelo M., Ribeiro, Mauricio A., Litak, Grzegorz, Bueno, Atila M., Balthazar, Jose M. Analysis and Chaos Control of A Four-Dimensional Magnetohydro-dynamic Model With Hyperchaotic Solutions. *European Physical Journal-Special Topics*, V. 1, P. 1-11, 2021.
7. Tusset, Angelo M., Balthazar, Jose M., Ribeiro, Mauricio A., Lenz, Wagner B., Rocha, Rodrigo T. Chaos Control of An Atomic

Force Microscopy Model In Fractional-Order. *European Physical Journal-Special Topics*, V. 1, P. 1-12, 2021.

8. Avanço, Rafael Henrique, Balthazar, José Manoel, Tusset, Ângelo Marcelo, Ribeiro, Mauricio Aparecido. Short Comments On Chaotic Behavior of A Double Pendulum With Two Subharmonic Frequencies and In The Main Resonance Zone. *Zamm-Zeitschrift Fur Angewandte Mathematik Und Mechanik*, V. 1, P. 1-10, 2021.
9. Ribeiro, Mauricio A., Tusset, Angelo M., Lenz, Wagner B., Kirrou, Ilham, Balthazar, Jose M. Numerical Analysis of Fractional Dynamical Behavior of Atomic Force Microscopy. *European Physical Journal-Special Topics*, V. 1, P. 1-10, 2021.
10. Da'm, Hilson H., Rocha, Rodrigo T., Balthazar, Jose M., Tusset, Angelo M. Dynamic Analysis and Synchronization for A System With Hyperchaotic Behavior. *Brazilian Journal of Physics*, V. 1, P. 1-13, 2021.
11. Tusset, Angelo M., Ribeiro, Mauricio A., Lenz, Wagner B., Rocha, Rodrigo T., Balthazar, Jose M. Time Delayed Feedback Control Applied In An Atomic Force Microscopy (Afm) Model In Fractional-Order. *Journal of Vibration Engineering & Technologies*, V. 8, P. 327-335, 2020.
12. Ribeiro, Mauricio A., Balthazar, Jose M., Lenz, Wagner B., Rocha, Rodrigo T., Tusset, Angelo M. Numerical Exploratory Analysis of Dynamics and Control of An Atomic Force Microscopy In Tapping Mode With Fractional Order. *Shock and Vibration*, V. 2020, P. 1-18, 2020.
13. Rocha, Rodrigo T., Tusset, Angelo M., Ribeiro, Mauricio A., Lenz, Wagner B., Balthazar, Jose M. Remarks on Energy Harvesting of Nonlinear Charge and Voltage Piezoelectric Models In A Two-Degrees-Of-Freedom Nonlinear Portal Frame Model. *Proceedings of The Institution of Mechanical Engineers Part C-Journal of Mechanical Engineering Science*, V. 1, P. 095440622093999-095440622093999, 2020.

14. Balthazar, J.M., Tusset, A.M., Ribeiro, E.P. Preface: On Dynamics, Control and Applications to Engineering and Life Science Iii. Mathematics in Engineering, Science and Aerospace: *The Transdisciplinary International Journal*, V. 11, P. 481-484, 2020.
15. Varanis, Marcus V., Tusset, Angelo Marcelo, Balthazar, José Manoel, Litak, Grzegorz, Oliveira, Clivaldo, Rocha, Rodrigo Tumolin, Nabarrete, Airton, Piccirillo, Vinicius. Dynamics and Control of Periodic and Non-Periodic Behavior of Duffing Vibrating System With Fractional Damping and Excited By A Non-Ideal Motor. *Journal of The Franklin Institute-Engineering and Applied Mathematics*, V. 357, P. 2067-2082, 2020.
16. Tumolin Rocha, Rodrigo, Tusset, Angelo, Ribeiro, Mauricio A., Haura Junior, Remei, Jarzebowska, Elzbieta, Balthazar, Jose Manoel. On The Positioning of A Piezoelectric Material in The Energy Harvesting From A Non-Ideally Excited Portal Frame. *Journal of Computational and Nonlinear Dynamics*, V. 15, P. 121002-12, 2020.
17. Fuziki, M.E.K., Abreu, E., De Carvalho, A. E., Silva, L.H. B.O., Fidelis, M. Z., Tusset, Angelo M., Brackmann, R., Dias, D. T., Lenzi, G. G. Sol-Gel Fe/Tio2 Magnetic Catalysts Applied To Selenium Photoreduction. *Topics in Catalysis*, V. 63, P. 1131-1144, 2020.
18. Lenz, Wagner Barth, Tusset, Angelo Marcelo, Ribeiro, Mauricio Ap., Balthazar, Jose Manoel. Neuro Fuzzy Control On Horizontal Axis Wind Turbine. *Meccanica*, V. 55, P. 87-101, 2020.
19. Varanis, Marcus, Norenberg, João Pedro C.V., Rocha, Rodrigo T., Oliveira, Clivaldo, Balthazar, José Manoel, Tusset, Ângelo Marcelo. A Comparison of Time-Frequency Methods for Nonlinear Dynamics and Chaos Analysis in an Energy Harvesting Model. *Brazilian Journal of Physics*, V. 50, P. 235-244, 2020.

20. Janzen, F.C., Tusset, A.M., Balthazar, J.M., Rocha, R.T., De Lima, Jeferson J., Nabarrete, A. Offshore Energy Harvesting of A Marine Floating Pendulum Platform Model. *Latin American Journal of Solids and Structures*, V. 16, P. 1-13, 2019.
21. Avanço, R.H., Tusset, A.M., Suetake, M., Navarro, H.A., Balthazar, J.M., Nabarrete, A. Energy Harvesting Through Pendulum Motion and Dc Generators. *Latin American Journal of Solids and Structures*, V. 16, P. 1-12, 2019.
22. Lima, J. J., Balthazar, J M, Rocha, R. T., Janzen, F. C., Bernardini, D., Litak, G, Tusset, A.M., Bassinello, D. On Positioning and Vibration Control Application To Robotic Manipulators With A Nonideal Load Carrying. *Shock and Vibration,* V. 2019, P. 1-14, 2019.
23. Varanis, M.V.M., Mereles, A.G., Silva, A.L., Balthazar, JM, Tusset, A.M., Clivaldo Oliveira. Modeling and Experimental Validation of Two Adjacent Portal Frame Structures Subjected To Vibro-Impact. *Latin American Journal of Solids and Structures,* V. 16, P. 1-20, 2019.
24. Piccirillo, V, Tusset, A.M., Balthazar, JM. Optimization of Dynamic Vibration Absorbers Based On Equal-Peak Theory. *Latin American Journal of Solids and Structures,* V. 16, P. 1-22, 2019.
25. Bressan, D.C., Ribeiro, M.A., Lenzi, G.G., Balthazar, J.M., Tusset, A.M. A Note On Sdre Control Applied in The Fermentation Reactor. *International Review of Mechanical Engineering* (Testo Stampato), V. 13, P. 576-586, 2019.
26. Rocha, Rodrigo Tumolin, Balthazar, Jose Manoel, Tusset, Angelo Marcelo, De Souza, Silvio Luiz Thomaz, Janzen, Frederic Conrad, Arbex, Hassan Costa. On A Non-Ideal Magnetic Levitation System: Nonlinear Dynamical Behavior and Energy Harvesting Analyses. *Nonlinear Dynamics,* V. 95, P. 3423-3438, 2019.

27. Tusset, Angelo M., Balthazar, Jose M., Rocha, Rodrigo T., Ribeiro, Mauricio A., Lenz, Wagner B. On Suppression of Chaotic Motion of A Nonlinear Mems Oscillator. *Nonlinear Dynamics,* V. 99, P. 537-557, 2019.
28. Andrade, David C., Bueno, Felipe, Franco, Felipe R., Silva, Rodrigo Adamshuk, Neme, Joao Henrique Z., Margraf, Erick, Omoto, William T., Farinelli, Felipe A., Tusset, Angelo M., Okida, Sergio, Santos, Max M. D., Ventura, Artur, Carvalho, Saulo, Amaral, Rodrigo Dos Santos. A Novel Strategy for Road Lane Detection and Tracking Based On A Vehicle?S Forward Monocular Camera. I*EEE Transactions On Intelligent Transportation Systems,* V. 20, P. 1497-1507, 2019.

In: Fundamentals of Photocatalysis
Editor: Orva Auger
ISBN: 978-1-68507-374-9

Chapter 2

PECULIARITIES OF THE REACTIONS ON PARTICULATE PHOTOCATALYSTS

Yoshio Nosaka[*]
Department of Materials Science and Technology, Nagaoka University of Technology, Nagaoka, Japan

ABSTRACT

Some peculiar issues of photocatalytic reactions which may have been overlooked in many reports are reviewed. In the beginning, electron transfer (ET) initiated reactions at the solid surface, which is essential in photocatalysis, are classified to four types based on the extent of the interaction of the reactant with the solid surface. Those four ET reactions are reversible reactions, irreversible connected reactions, deposition, and dissolution. Most photocatalytic reactions are irreversible ET connected reactions and deposition of the products that strongly interact with the solid surface, while, in electrochemistry, reversible reaction for the reactants of weak interaction is mainly treated. Though the relationship between the reaction rate and the reaction energy has been discussed with the Marcus-Gerischer theory of electrochemistry, the acceptance of this

---

[*] Correspondence Author's E-mail: nosaka@nagaokaut.ac.jp.

theory for photocatalysis may cause difficulties because the frequency of the ET is limited by the photon absorption and the ET reaction rate is compete with the carrier recombination. Namely, the usage of the reorganization energy may need careful consideration for the kinetic analysis in semiconductor photocatalysis. The electric potential near the photocatalyst surface was visualized and it was realized that the potential gradient was localized near the surface holes, whereas it was expanded to the whole surface of the flat electrode in electrochemistry. Since the semiconductor photocatalysts are not wired to an electric source, the charges stored in the semiconductor particle can be evaluated. Then, a precise energy band position could be obtained and it may be different from the measurements by electrochemical methods, which was discussed in terms of the band alignments of anatase and rutile TiO_2 crystals. The analysis of the reaction kinetics for heterogeneous photocatalysis should be different from that for the homogeneous solution because a pair of the redox reactions take place in the same particle. Then, the novel method for applying the Langmuir-Hinshelwood equation was presented to describe the photocatalytic oxidation as a function of both the reactant concentration and the light intensity.

INTRODUCTION

Photocatalytic reactions using semiconductor nano-particles have been gathering much attention in recent years because of the unique applications of photoenergy for environmental cleaning and solar fuel productions [1-3]. The reactions in photocatalysis are initiated by photoinduced electron-hole pairs in semiconductor nanocrystallites. Charge transfer reactions of both reduction and oxidation takes place at the crystallite particle surface by competing with the recombination reaction as illustrated in Figure 1, where species A is reduced to B and the specie D is oxidized to E at the surface of particulate semiconductor. Figure 1 shows only simple concept of photocatalysis. In the actual photocatalytic reactions, there are many special concept to understand the reaction steps. Therefore in this chapter, reverting to the fundamentals of charge transfer reactions, some peculiar issues in the photocatalysis will be described. Starting from the classification of various reactions originated from the electron transfer (ET) at solid-solution interface, the adaptation of Marcus-

Gerischer theory to the photocatalytic reactions, summary for the essential difference between photocatalysis and electrochemical reactions, simulation of the electric potential formed near the photocatalyst surface, peculiarity that the ET reaction takes place only by photo absorption in the particle which is free from an electric source, finally the rates of photocatalytic oxidation were expressed as a function of both the reactant concentration and the light intensity by confining the electron-hole pairs in each particle for the kinetic analysis.

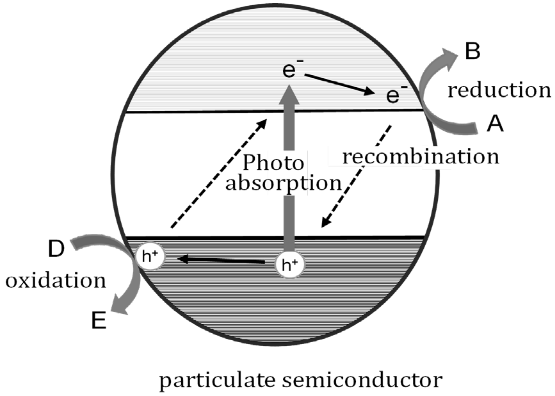

Figure 1. Fundamental reactions of photocatalysis for the reduction of A and the oxidation of D with the recombination of electron-hole pairs.

VARIOUS CHARGE-TRANSFER REACTIONS AT SOLID-SOLUTION INTERFACES

In order to discuss the types of the surface ET reactions, it is important to describe the extent of the interaction between the reactant molecules and the solid surface. The extent of the interaction could be classified into 3 cases as shown in Figure 2. When the interaction is very weak, the reactant A and the surface is separated with two solvent molecules at the nearest contact as shown in Figure 2(a). On the other hand, when the interaction between the reactant A and the surface is very strong the reactant A makes contact directly with atoms of the solid surface as illustrated in Figure 2(c).

In the moderate strength of the interaction, the reactant A may be separated by one solvent molecule as shown in Figure 2(b).

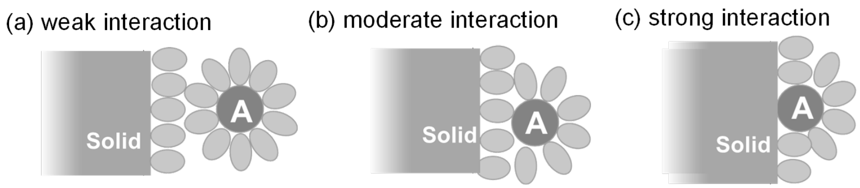

Figure 2. Schematic illustration for the various strengths of interactions between the solute molecule A and the solid surface with solvent molecules shown by ovals.

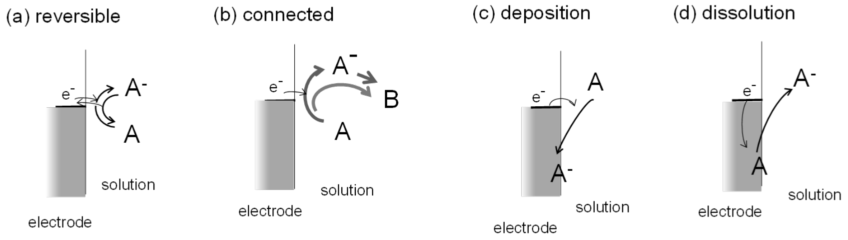

Figure 3. Possible changes of reactant A by the electron transfer at the solid-solution interfaces. The similar figure can be obtained for reactant D by reverse electron transfer or hole transfer.

In general, surface ET reactions cause various chemical events. The plausible chemical events could be classified to four types of reactions as shown in Figure 3, which are (a) reversible ET reactions without chemical reactions, (b) the ET connected reactions which change the species A to B by the modification of chemical bond, (c) the deposition of the ET product being incorporated into the solid surface. As the reverse reaction of the deposition, (d) the dissolution of ions from the surface is one of the categories of the ET induced reactions. For the ET connected reactions in Figure 3(b), the processes may be distinguished whether the ET species A^- is involved as an intermediate before giving the product B. Though the four reaction categories in Figure 3 are shown only for the electron transfer, similar figures can be provided for the hole transfer. In the case of the hole transfer, e^-, A, A^- and B in Figure 3 should be replaced by h^+, D, D^+ and E, respectively.

When the interaction of the reactant A with the solid surface is weak as shown in Figure 2(a), the electron transfer takes place as reversible reaction at the outer solvation sphere as shown in Figure 3(a). In other words, reaction occurs at the outer Helmholtz plane (OHP). In this case, the products A^- in OHP may be stable, and the transferred electron could be released to the solid as the reverse reaction. A typical example of this reversible surface electron transfer reaction is the electrochemical reduction of ferric ions (Fe^{3+}) to ferrous ions (Fe^{2+}) in aqueous solution. The fraction of two ions is basically determined by the difference of the free energies G^0 between electrons in the electrode and ions in the solution depending on the Nernst equation.

The reaction energy ΔG^0 corresponds to the potential difference ΔE between the standard reduction potential E^0 and the electrode potential ϕ (or the Fermi level of the electrode) as given by Eq (1).

$$\Delta G^0 = e\,\Delta E = e\,(\phi - E^0) \tag{1}$$

The reaction rate may correlate with the reaction energy ΔG^0. However, due to the change in the number of charge, the solvation energy may vary with the ET. This issue will be discussed in the next section as the reorganization energy.

The ET connected process in Figure 3(b) is important, because photocatalytic reactions are usually applied for the decomposition of molecules. As described above, there are two cased in the ET connected reactions. These are concerted pathway of directly producing B and stepwise pathway *via* A^-. The actual reaction pathway might depend on the free energies of A^- and B, or $-E^0(A/A^-)$ and $-E^0(A/B)$. As an example of the ET connected reactions, the electrochemical dissociation of organic halides (RX) has been investigated [4]. Figure 4 shows schematically the energy diagram of the concerted reaction. Where, RX is A while $R^\bullet + X^-$ corresponds to B in Figure 3(b). In the case of stepwise process, $RX^{\bullet -}$ radical as A^- should be expected, while this radical could not be detected in the case of concerted ET reaction. What is the controlling factor of the pathway from the stepwise to the concerted mechanism? When the energy level of the electrode electron reaches the standard potential energy of the $RX/RX^{\bullet-}$ redox, $-E^0(RX/RX^{\bullet-})$ as shown in Figure 4, the stepwise reaction *via* $RX^{\bullet-}$ takes place. Thus, the pathways of the dissociative ET reaction change from the concerted mechanism to the stepwise mechanism along with the increase of the electrode potential. When the difference ε of the standard potentials between the $(R^{\bullet}+X^{-})$ formation and the $RX^{\bullet-}$ formation, that is $\varepsilon = E^0(RX/R^{\bullet},X^{-}) - E^0(RX/RX^{\bullet-})$, is large, the concerted reaction is more favorable to take place. Antonello and Maran [5] showed that the transfer coefficient α in electrochemistry is a sensitive probe of the mechanism by which the ET and the bond cleavage are coupled in the dissociative ET. The transition from the concerted mechanism to the stepwise mechanism has been confirmed by the increase of α in the experiments of the electrode reduction with the irreversible cleavage of the O-O bond for a series of perbenzoates, such as *ter*-butyl *para*-acetylperbenzoate in DMF [5].

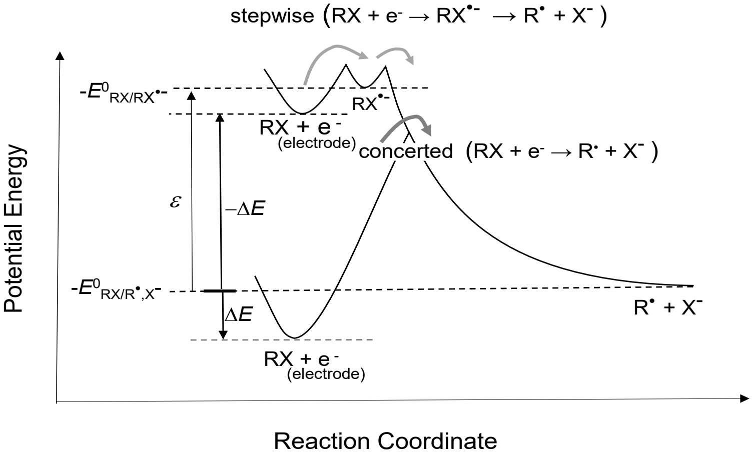

Figure 4. Potential energy of the two pathways, the stepwise and concerted paths, for the ET connected dissociation in organic halides RX as an example of ET connected reaction in Figure 3(b). Reproduced with permission from Houmam et al. [4]. Copyright 2008 American Chemical Society.

As illustrated in Figure 3(c), when the product of the ET reaction interacts very strongly with the solid surface, atoms or ions may be incorporated or deposited at the solid surface. A typical example is the deposition of metal by the reduction of metal ions. Another example is the oxidative deposition of Cl^- ions, in which Cl atoms are deposited on Ag electrode to form AgCl [6]. As illustrated in Figure 3(d), dissolution corresponds to the reverse reaction of the deposition. The dissolution of ions from the solid surface is one of the plausible chemical changes with charge transfer.

In the above discussions, only reactions caused by one-electron transfer at the solid surface were shown. However, there are many examples of reactions caused by the multi-electron transfer. In the case of electrochemistry, since the electrons are supplied continuously from the electric source through the lead wire, the outer-sphere ET reaction in Figure 3(a) may sequentially proceed to generate the multi-electron products. On the other hand, in photocatalysis, since the electron and hole cannot be generated continuously and they disappear rapidly by the recombination, the outer-sphere multi-electron reaction cannot take place. On the other hand, when the ET products are strongly adsorbed on the photocatalyst surface, the relatively stable intermediate species are produced as the first step of the multi-step reactions. Thus, the multi-electron photocatalytic reactions take place with the ET adsorption of Figure 3(c) followed by the ET dissolution of Figure 3(d). For example, the oxidation of H_2O_2 to O_2 can be expressed as the oxidative deposition as $\bullet O_2^-$ ions and succeeded oxidative dissolution as O_2 was suggested [7, 8]. In the water oxidation to produce O_2, or oxygen evolution reaction (OER), the intermediate has a higher free energy. Therefore, the adsorption to form transition metal oxyhydroxides is required [7, 8].

REACTION RATES AND REORGANIZATION ENERGY

The ET reaction rate k_{et} has been discussed as a function of the reaction energy ΔG^0 which is the free energy change by the reaction. Marcus analyzed at the first time the ET rate of metal ion complex in homogeneous solution [9]. After the successful evaluation of experimental data with the reorganization energy λ, the ET reactions at electrodes were analyzed by Marcus [9, 10] and Gerischer [11]. In these theories of the ET kinetics, the free energy of the transition state, $\Delta G^{\neq}$, can be calculated with the reorganization energy λ based on the harmonic oscillator model.

$$\Delta G^{\neq} = (\Delta G^0 + \lambda)^2/4\lambda \tag{2}$$

The reorganization energy λ is usually treated as the sum of two contributions; the vibration of the ion-solvent bond within the first solvation shell (λ_i) and the orientation change of the surrounded solvent dipoles (λ_o) [9, 12]. For the redox reaction of $Fe^{3+}{}_{aq}/Fe^{2+}{}_{aq}$, λ was measured to be 2.1 eV for an Au electrode and then λ_o was calculated to be ≈1.2 eV from the size of the first solvation shell and the permittivity of water [12]. At the surface of metal electrodes, λ_o tends to decrease by half in the homogeneous solution as the effect of the mirror image. However, at the semiconductor surface λ_o could not decrease by a possible image charge [10]. The Marcus-Gerischer theory has been applied until now to treat ET rate as a function of energy difference. For example, in the outer sphere electrochemical oxidation of NH_3 to N_2H_4 [13], the energy and the values of λ_i and λ_o have been calculated by the density functional theory (DFT), and then the activation energy was found to be expressed by the Marcus equation by replacing the bond dissociation energy by λ_I [13].

Since the reaction rate is proportional to the term of $\exp(-\Delta G^{\neq}/k_BT)$ with Boltzmann constant k_B and temperature T, the rate of ET, k_{et}, can be expressed by Eq (3) from Eqs (1,2) with a pre-exponential factor A.

$$k_{et} = A\exp\left[-\frac{(\Delta G^0+\lambda)^2}{4\lambda k_BT}\right] = A\exp\left[-\frac{(e\phi-eE^0+\lambda)^2}{4\lambda k_BT}\right] \tag{3}$$

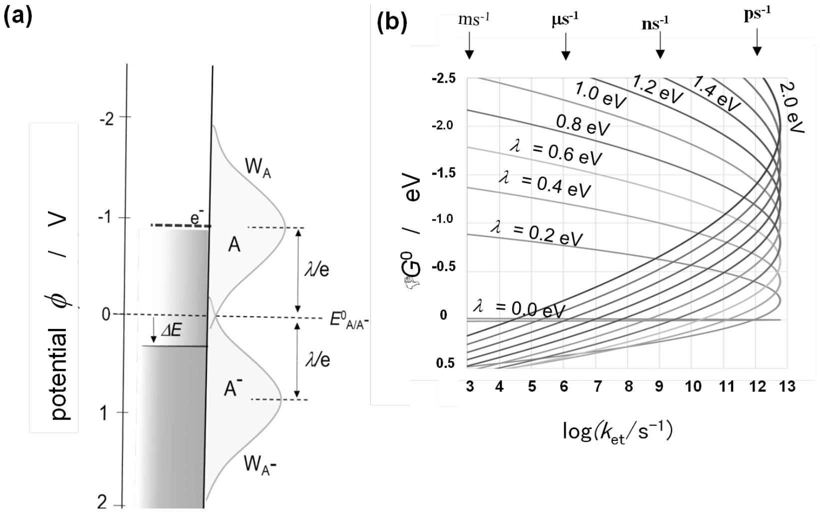

Figure 5. (a) Probability distribution of the energy state in the oxidized species W_A and the reduced species W_{A^-} besides the energy level of the electron in the electrode in the Marcus-Gerischer theory with the reorganization energy λ of 0.9 eV and the standard potential E^0 of 0 V. (b) Electron transfer rate calculated based on the Marcus-Gerischer theory with Eq (3), which corresponds to W_A in (a).

For the pre-exponential factor, a very simple estimation is $A \approx k_BT/h$ with Plank constant h. By using the estimated value of $A = 6\times10^{12}s^{-1}$, Eq (3) gives us the k_{et} as a function of the reaction energy ΔG^0 for various reorganization energies λ as shown in Figure 5(b). The probability of electron transfer W_A as a function of electrode potential ϕ in Figure 5(a) corresponds to the ΔG^0 dependence of the k_{et} in Figure 5(b). When $\phi = E^0 - \lambda/e$, or $\Delta G^0 = -\lambda$, the Eq (3) suggests that the k_{et} becomes maximum owing to the barrier free condition of $\Delta G^{\neq}=0$.

Gerischer described W_A as the density for the oxidized state in his early reports. In the process of the citation, the terminology of density of states (DOS) for the oxidation and reduction has been used [12]. Therefore, the W_A in Figure 5(a) could be easily mixed up to the states as if there exit some energy levels. The energy state of A/A^- redox couple is not distributed, but it is just the energy for reorganization to diverse the distribution when the adiabatic ET takes place [14]. It should be noted that the W_A in Figure 5(a) is the energy distribution of the transition probability for the ET reaction and it is entirely different from the DOS of electrons in materials [14].

In electrochemistry the kinetics is commonly analyzed as the reversible ET reactions as shown in Figure 3(a). Based on the assumption, the reorganization energy may be effective only for reversible electrode reaction, and basically the Marcus-Gerischer theory could be adoptable only for the reactants of weak interaction [15]. Actually, the values for λ experimentally obtained in most reports are of reversible ET reactions. In the photoinduced ET for colloidal TiO_2 solution, the values of λ for some redox reactions have been reported. For methyl viologen, by measuring the maximum ET rate on the pulsed laser excitation by changing ΔG^0, $\lambda = 0.3$ eV was reported [16]. For thiocyanate ions, the ET rate k_{et} was estimated from the oxidation yield against reported recombination rate. By using the standard potential E^0 of +1.33 V and the valence band potential of $\phi = +3.0$ V, $\lambda = 0.64$ eV was obtained from the estimated k_{et} and $A = 10^{13}$ s^{-1} with Eq (3) [17]. For salicylate ions, from the analysis of the yield of oxidized salicylate at two different excitation wavelengths, $\lambda = 0.58$ eV was reported [18]. Since the ET reaction must be terminated to overcome the rapid electron-hole recombination, almost all the photocatalytic reactions are irreversible as categorized to (b) and (c) in Figure 3.

In the case of electrochemical connected ET reaction of Figure 3(b), Savéant had suggested that λ_i may be replaced by the dissociation energy [19, 20], and the Marcus-Gerischer theory may be basically applied when the reaction is not coupled with chemical changes involving the disruption of chemical bond [4]. Therefore, this theory may be employed for the first step in the stepwise mechanism or the D^+ formation in connected ET reactions. In usual photocatalytic oxidation reactions for organic molecules RH, the ET state D^+ corresponds to $RH^{\bullet+}$. However, the $RH^{\bullet+}$ radical usually has a high standard potential comparing to that of ($R^\bullet$+H^+), which means a large ε in Figure 4. Therefore, the stepwise mechanism of producing $RH^{\bullet+}$ may not take place in usual photocatalysis. When the concerted oxidation in the photocatalytic oxidation of RH for directly producing $R^\bullet$+H^+ is the rate determining step, the reorganization energy in the Marcus-Gerischer theory could not be simply applied because the bond dissociation energy has been included into the reorganization energy. Therefore, in this case, Eq (3) could not be used, and the reaction rate is almost simply proportional to the exponential of energy difference $k_{\mathrm{et}} \propto \exp(-\Delta G^0/k_{\mathrm{B}}T)$ [4, 5].

Since the ET rate in electrode reactions is usually measured by the current of the electrode, Figure 5(a) which shows the maximum reaction rate may gain full meaning. However, in the case of photocatalytic reaction, the reaction rate is usually measured by the decrease of the reactant or the formation of the product, and the maximum rate in photocatalysis is controlled by the photo excitation rate which is about $(1\ \mathrm{ms})^{-1}$ under usual condition [21]. Therefore, the fact that the ET reaction is faster than the charge recombination is important, though the recombination rate could not be easily measured. However, the rate of ET can be estimated as shown in Figure 5(b). Even at the standard potential ($\phi = E^0$), namely at $\Delta G^0 = 0$, $\Delta G^{\neq}$ becomes $\lambda/4$, and then k_{et} has a certain value. For example, when $\lambda \leqq 0.6\mathrm{eV}$ the electron transfer rate k_{et} is larger than $(53\ \mathrm{ps})^{-1}$ as calculated from Eq (3). Therefore, the ET reaction in photocatalysis may take place even at the equivalent energy levels because the recombination takes place around 10-100 ps [1]. Since the reorganization energy λ is a parameter for the ET reaction rate, it is not the factor that directly affects the energy level for the actual electron transfer. However, there are many reports [22-27] in which reorganization energy was adopted for the kinetic analysis of reaction rates in photocatalysis using the energy diagram of Figure 5(a).

Kisch described that the interfacial ET in photocatalysis is thermodynamically allowed when the quasi-Fermi level of reactive electrons (which locates between the flatband potential and the conduction band bottom) is equal or more negative than the potential (E^0-λ/e) [26]. Since λ is a kinetic parameter which concerns to the reaction rate as described above, it should not affect the thermodynamic parameter and then the thermodynamic allowance cannot be changed by λ. Montoya et al. adopted the Marcus-Gerischer theory to the photocatalytic ET reaction and described that the rate depends on the degree of overlapping between the semiconductor energy band and the redox transition distribution with λ of the substrate [27]. However, the carriers in the energy band may be relaxed to the bottom (or the top in the case of holes) before arriving to the surface. The electron transfer rate may not be faster than the inner sphere vibration, meaning that the adiabatic transition is effective only for the outer sphere ET reactions. As described above, the ET reaction of photocatalysis could not usually take place at the outer sphere in Figure 2(a) because the electric potential gradient is localized near the surface hole.

In the above discussion, the standard potential E^0 in a homogeneous solution was employed as the free energy. However, the free energy of the reactant A may vary depending on the interaction with the solid surface. When the interaction, or adsorption, is strong as illustrated in Figure 2(c), the solid surface serves a catalytic function, then the product B may be formed more easily without the formation of A^- in the connected reaction. Therefore, the concerted mechanism in Figure 3(b) becomes more favourable in the case of photocatalysis. When the adsorbed molecules become the transition state, the free energy of each transition state should be calculated by the DFT method, and then the Marcus-Gerischer theory is not easily applied. For example, the free energy of the transition state of oxygen evolution has been calculated for the reactions over NiS_2/$NiSe_2$ [28] and over the reducible metal oxides such as TiO_2 [29]. Furthermore, the importance of the defect in electrocatalysis of O_2 over carbon materials has been experimentally revealed and it was reviewed [30].

In conclusion, the energy dependence of the interfacial ET rate is not straightforward to control the amount of product because the reaction rate of photocatalysis is usually analysed by the reaction product which is determined by the photo absorption rate, but not simply by the interfacial ET rate. Though the ET reaction usually compete with the carrier recombination, the kinetic analyses of photocatalytic reaction merely using the Marcus-Gerischer theory could be seen in many reports. It seems like they need careful considerations.

ESSENTIAL DIFFERENCE BETWEEN PHOTOCATALYSIS AND ELECTROCHEMISTRY

Reactions of electron transfer at solid surfaces are the subject of electrochemistry for a long time. Therefore, many concepts of electrochemistry are involved in the thermodynamical and kinetic discussions of photocatalysis. In the above section, the difference in kinetics between electrochemistry and photocatalysis has been discussed. When photocatalysis and electrochemistry are globally compared, the fundamental differences could be summarized in Table 1, and the peculiarity of photocatalytic reactions can be realized [6].

Table 1. Comparison between semiconductor photocatalysis and electrochemical electrolysis (electrochemistry)

	Photocatalysis	**Electrochemistry**
Form of solid	Powder, Crystallite film	Sheet, Film
Surround	Solution, Air	Electrolyte solution
Origin of charge	Photoabsorption	Power source
Typical Reaction	Irreversible (vs. rapid recombination)	Usually reversible (equilibrium)
Monitor for reaction	Product analysis	Electric current

The features of the ET reactions may be different between electrochemistry and photocatalysis because the circumstances of the ET reaction are largely different. In electrochemistry, a counter electrode and electrolyte solution should be employed, and the potential in the working electrode can be controlled by the electric source through a lead wire. The electrolyte solution is essentially indispensable to apply the electric potential to a molecule at the surface of working electrode. On the other hand, in photocatalysis, neither the counter electrode nor the electrolyte solution are employed. Therefore, it has not been clarified how the electric potential distributes near the surface of photocatalysts. The difference in the spatial profile of the potential will be discussed in the next section.

As stated above, by using electrode the reaction rate of the interfacial ET could be monitored as the current. On the other hand, electron transfer can be recognized only by the change in the amounts of the reactant or the product in semiconductor photocatalysis, where the electron transfer occurs only by the one electron-hole pair generated by absorption of one photon in a photocatalyst particle. In the usual photocatalysis with a particle of 27-nm diameter, under the normal light intensity of 10 $\mathrm{mWcm^{-2}}$, the photon absorption interval per particle is about one milli-second [21]. Therefore, the charge transfer rate would not be directly measured usually and then the kinetics of the interfacial reaction may largely differ from the electrochemical reactions. Due to these differences, the concept of electrochemistry may not be fully adoptable for the arguments in photocatalysis of particulate semiconductor.

ELECTRIC POTENTIAL NEAR THE SOLID SURFACE

For electrochemical reactions, the electrolyte solutions are indispensable to apply the electric field to the reactant molecules located near the working electrode against the counter electrode. On the other hand, for photocatalysis, the counter electrode and the electrolyte are not necessary. In electrochemistry, the feature of the electric potential near the solid surface could be given by the extension of the Debye-Hückel model of the point charge to the charge on a plane [31]. Thus the electric potential from the double layer at distance y is calculated with the following equation [32].

$$\phi = \phi_0 \exp\left(-\sqrt{\frac{8\pi e^2 N_\mathrm{A} C}{\epsilon_r \epsilon_0 k_\mathrm{B} T}}\, y\right) \tag{4}$$

where C is the ion concentration of electrolyte, e the elementary charge, N_A the Avogadro constant, ϵ_r the relative permittivity of the solution (ϵ_r= 80 for water), ϵ_0 the permittivity of vacuum. In Figure 6, the potential ϕ

for various electrolyte concentrations *C* is plotted as a function of the distance *y* from the electrode surface [6]. Only when the electrolyte concentration is as higher as *C*= 0.1 M, the electric potential could be applied for molecules near the electrode (< 0.1 nm). Thus, Figure 6 shows that a higher concentration of electrolyte is necessary to form a potential gradient near the electrode surface.

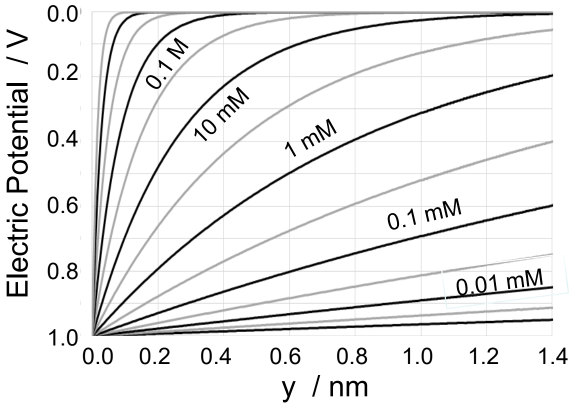

Figure 6. Electric potential ϕ in the electrolyte near the electrode polarized to ϕ_0=+1.0 V against the bulk solution, which was calculated by Eq (4) for various ion concentrations C. Reproduced from Ref [6] with permission from PCCP owner societies. Copyright 2020 Royal Society of Chemistry.

For photocatalysts, what is the feature of the electric potential near the surface? In order to know the potential profile, the two-dimensional Poisson equation Eq(5) can be used

$$\frac{\partial^2 \phi}{\partial x^2} + \frac{\partial^2 \phi}{\partial y^2} = 0 \tag{5}$$

where *x* is the distance from the positive hole along the surface, and *y* is the distance from the surface in the perpendicular direction. When we assume the use of n-type semiconductors, the potential difference between surface trapped electron and flatband potential is very small. Therefore, the potential gradient was examined only at the surface hole. The size of the positive hole was assumed to be the size of oxygen ion, which is about 0.3 nm. The potential ϕ at the positive hole was set to be +2.5 V relative to the flatband potential, and at the other place of the surface ϕ should be the flatband potential. In Figure 7(a), the boundary condition for Eq (5) is shown by the rectangular line of y = 0.0 nm. The calculation was performed in the Cartesian coordinate system, that is, the flat surface was presumed. Since the potential gradient spreads in a small area of less than 2 nm, the surface curvature of the photocatalyst particle does not largely affect the potential profile. Thus, the electric potential ϕ was obtained as a function of x and y by solving Eq(5) numerically [6]. Figure 7(a) shows the several y-sections of the potential $\phi(x,y)$. At 0.2 nm above the surface, namely at y = 0.2 nm, the potential has a minimum of about +1.0 V at $x = 0$ and becomes about 0.0 V at $|x| \geqq 0.5$ nm. Figure 7(b) shows the x-sections of the potential $\phi(x,y)$, that is the potential profiles near the surface at various distances from the surface. Thus, it is revealed that the positive hole at the surface causes a potential gradient of a bent-funnel shape. It is notable that the potential gradient in the solution near the photocatalyst surface is generated similarly to the case of electrodes in the electrolyte solution with a counter electrode. When the electric potential at the photocatalyst surface is compared with that at the electrode surface in Figure 6, only difference is that the potential gradient locates near the surface positive hole in the case of photocatalyst. Since the frequency for the reactant species to approach the potential gradient by definition should be small in photocatalysis, it is possible that the valence band holes are trapped at the surface where the reactant has been adsorbed.

In many cases of semiconductor photocatalysis, the ET induced reactions may be performed in solution similarly to the reaction of electrochemistry. However, the practical photocatalysts are widely used under the air, where the photocatalyst surface is known to be covered with a few layers of water molecules in the ambient environment [33]. Since Eq(5) does not contain the electric susceptibility of the medium, the potential around the particle in air should not be altered from that in water. Therefore, Figure 7 suggests that the electric field should be generated near the surface hole regardless the environmental conditions, and it can be concluded that the photocatalytic oxidation in the air must take place similarly to the case of the aqueous suspension.

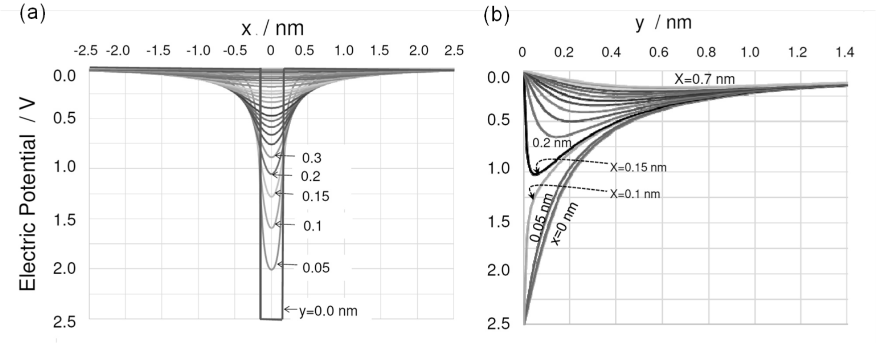

Figure 7. Electric potential ϕ produced at the front of the photocatalyst surface calculated with the Poisson equation, Eq (5). (a) Potential at various distance *y* from the surface and (b) the distance profile of potential surface at various position *x*. Figure (a) was reproduced from Ref [6] with permission from PCCP owner societies. Copyright 2020 Royal Society of Chemistry.

LEAD-WIRE-FREE PARTICULATE PHOTOELECTRODE

As has been pointed out above, the solid electrode in electrochemistry is connected to an electric source with a lead wire and electrons can be supplied continuously. On the other hand, in photocatalysis the transferring charges originate from the photo excitation of electrons in the crystallite. Since the carriers are not supplied successively, the ET reactions should be finished before the elimination of electron-hole pairs by recombination. Therefore, almost all reported photocatalytic reactions are irreversible.

Although almost all the photocatalytic reactions are irreversible, there are some examples for the reversible ET reactions. One example may be the reduction of O_2, in which the reduction product $\bullet O_2^-$ is relatively stable [8]. The reversible O_2 reduction at the surface may prolong the lifetime of the photo-induced electrons, which causes the lifetime of photoinduced electrons to be relatively longer than the photoinduced holes [15, 21]. Since the reduction actually occurs near the standard potential of $E^0 = -0.33$ V, it is obvious that the reversible reaction does not take place at the outer solvation sphere. Actually the reorganization energy λ for the reduction of O_2 was reported to be λ = 2.2 eV [34], and $\Delta G^{\neq}$of $\bullet O_2^-$formation is calculated to be 0.43 eV at ϕ = -0.6 V from Eqs(1,2). The ET rate calculated from Eq(3) is $k_{et} = (2\ \mu s)^{-1}$ which may not compete with the rapid initial carrier recombination. Therefore, the actual transition energy $\Delta G^{\neq}$of $\bullet O_2^-$ formation is significantly smaller than that calculated by Marcus equation of Eq(2), suggesting that the small barrier was originated with the adsorption of O_2 on the surface. The reduction product $\bullet O_2^-$ can be stabilized by the adsorption as has been discussed in our previous report [8]. Therefore, this reversible reaction in photocatalysis may take place in the adsorbed state. In other word, this reversible reaction could not be expressed by Figure 3(a), but it is regarded as reductive deposition (c) and succeeding oxidative dissolution (d) in Figure 3. This process of releasing the electron to the conduction band of semiconductor could not be recognized in electrode systems but only conceivable in the lead-wire free particulate system.

Another example of reversible ET in photocatalysis is methylviologen which has been known to provide a stable redox couple (MV^{2+}/MV^+) under deaerobic condition. This compound has been used in many reports, due to the convenient property that the extent of the ET reduction can be easily measured by the optical absorption in the visible-light region. The reorganization energy of the MV^{2+} reduction over colloidal TiO_2 was experimentally obtained with kinetic analysis to be $\lambda = 0.3$ eV [16], and it is smaller than that at the electrode, $\lambda = 0.6$ eV [35] as stated above. The smaller λ for particulate photocatalysts is attributable to the limited potential gradient as illustrated in Figure 7.

The redox potential of the MV^{2+}/MV^+ couple, which is -0.45 V (vs. SHE), is not dependent on the pH change, while the electronic potential of metal oxides move up with the solution pH. Therefore, the potential of MV^{2+}/MV^+ relative to metal oxides goes down with pH as shown in Figure 8, where DOS of TiO_2 are schematically depicted. Thus, the observation of the pH effect on ET reactions has been used to investigate the electronic energy levels of metal oxide particles. For colloidal TiO_2 particles, the ET of the conduction band electron to MV^{2+} was measured by monitoring the increase of MV^+ on the pulsed laser excitation. As the result, the flat band potential was -0.14 V vs. NHE at pH = 0 (or vs. RHE) [16]. By using electrochemical analysis of the produced MV^+, the Fermi levels of TiO_2 particles of anatase and rutile particles have been estimated to be -0.05 and -0.01 V [36] and recently -0.04 and +0.04 V [37], respectively. This evaluation method could be used under photo irradiation to measure the quasi-Fermi levels of the modified TiO_2 photocatalysts [26].

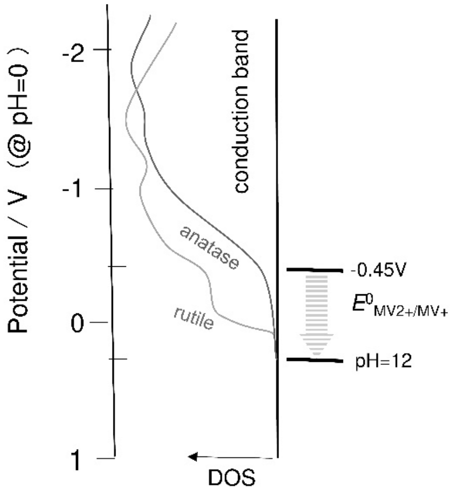

Figure 8. Schematic illustration for the relative energy level of conduction band and the redox potential of methyl viologen.

The number of the electrons accumulated in each energy level in the TiO_2 particle has been evaluated from the amount of MV^+ at various pH [38]. The experimental results obtained with the sacrificial electron donor, triethanolamine or methanol, are reproduced in Figure 9, where the scale of the electric potential ϕ is adjusted to the standard potential of the MV^{2+}/MV^+ couple at pH = 0. Although the authors reported this figure as the electrons stored at the defective site of TiO_2 crystals [38], the number of electrons reported could be counted to be about 1/3000 of the Ti-d states of TiO_2. Furthermore, the recent laser spectroscopic studies suggest that the defect level of anatase crystal should not expand to deeper energy levels comparing to that of rutile crystals [39]. Therefore, the electrons stored in the particles are probably regarded as those accumulated in the conduction band bottom as previously reported in the literatures [36, 37].

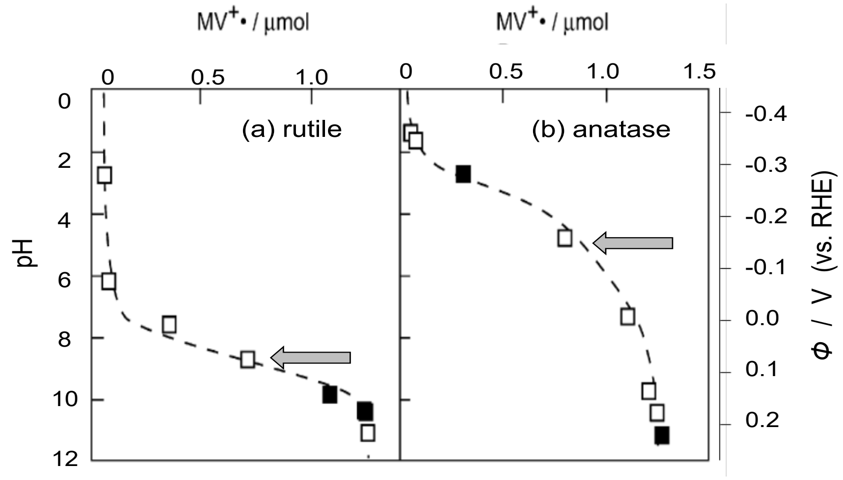

Figure 9. Amounts of produced MV^+ are plotted as a function of the pH of the ET reaction, in which electrons were stored in two kinds of TiO_2 powders by photocatalytic reactions at pH 11(□) and pH 2(■) with a sacrificial electron donor [38]. The arrows indicate the flat band potential obtained from the Mott-Schottky analyses in aqueous media [40]. Reproduced from Ref [6] with permission from PCCP owner societies. Copyright 2020 Royal Society of Chemistry.

Figure 9 shows that, with the increase of the solution pH, the electrons stored in the particles become capable of reducing MV^{2+} to MV^+ as indicated in Figure 8. For the rutile TiO_2 particles in Figure 9(a), the curve is steep and a half of the stored electrons are transferred to MV^{2+} at pH=8.7 as shown by the arrow. This pH corresponds to the potential ϕ of +0.063 V (=-0.45+0.0592×8.7). Taking the thermal energy of 0.026 eV for the ET into the account, the flatband potential of the rutile crystal is estimated to be +0.037 V, which is compatible to the data obtained by many Mott-Schottky analyses [40]. For anatase polymorph of TiO_2, Figure 9(b) shows that a half of the stored electrons transfer to MV^{2+} at pH = 5. This observation indicates the flat band potential of -0.17 V (vs. RHE) which is also compatible to the Mott-Schottky analysis [40]. In the case of anatase, a small part of the stored electron remains at the higher pH, indicating that the energy levels of anatase TiO_2 extent to the lower potentials. Since the anatase TiO_2 is an indirect-transition semiconductor, the DOS calculated with a DFT method shows that the extension of a very small amount of DOS to the conduction band bottom [41, 42], as schematically depicted in Figure 8.

The present authors have examined the band alignment of anatase and rutile TiO_2 [43]. Experimental data of the higher rate of O_2 reduction suggested that the conduction band bottom of rutile should be higher than that of anatase. The electrochemical impedance method for Mott-Schottky analysis has been commonly used to evaluate the flat-band potential [40]. Though the opposite band alignment in aqueous media was confirmed, it has been shown that the work function of rutile and anatase varied on the environment [40]. In the analysis of electrochemical impedance, since the TiO_2 electrode is wired with the electric source to measure the small alternating current, the energy levels with small DOS may be overlooked [43]. On the other hand, by using semiconductor powders, the precise number of electrons can be measured by using the pH-dependence of the MV^{2+} reduction because the number of the stored electrons in the conduction band became steady state by the recombination with the oxidized products [36]. The number of states at the conduction-band bottom is limited because the number of Ti atoms in the particle is limited. Therefore, the lowest energy state of the conduction band of each particle could not be equal to that of bulk semiconductor for the very small DOS region. Thus, in the case of anatase in Figure 9(b) the distribution of the energy levels of the stored electron of each particle would reflect the properties of DOS at a lower potential edge. Even if Figure 9 reflects the energy distribution of the defective sites as suggested in the report [38], these sites could not be detected by the electrochemical measurements.

EFFECTS OF LIGHT INTENSITY AND REACTANT CONCENTRATION ON PHOTOCATALYTIC OXIDATION RATES

Though photocatalytic reactions gather enormous attention, dependences of light intensity and reactant concentration in powder suspension system have not been concurrently expressed by distinct equation. As illustrated in Figure 1, photoinduced electrons and holes are both produced in the same particle. However, in many reports, the concentration of electrons [e^-] and holes [h^+] in solution are independently treated for the kinetic analysis [44]. In other words, the photogenerated charges in the particle have been analyzed as the individual reactants in solution. On the other hand, the dependence of the reactant concentration on the reaction rates has been analyized with Langmuir type adsorption of reactant molecules on the surface of the particle. To combine the dependence of the reactant concentration with the light intensity dependence, the kinetic equation reported became complicated [27, 45, 46]. Previously, the present authors successfully analyized the dependences of the size of powders and the intensity of excitation light on the photoinduced ET efficiency using the 2D-ladder kinetic model [47]. By applying this model to the photocatalyst suspension, we analyized the dependencies of light intensity and the reactant concentration on the initial reaction rates of photocatalytic oxidation as follows [21].

In this kinetic model, the rates of four fundamental processes were treated as the transitions between the states of each powder characterized by pair numbers of possessing negative and positive charges. We can described the initial part as follows.

i. photo-absorption or generation of charges in a semiconductor particle,

$$\{0,0\} \xrightarrow{g} \{e^-,h^+\} \text{ or } \{1,1\} \tag{6}$$

ii. reduction of A to B

$$\{1,1\} + \mathrm{A} \xrightarrow{\kappa_\mathrm{e}} \{0,1\} + \mathrm{B} \tag{7}$$

iii. oxidation of D to E

$$\{1,1\} + \mathrm{D} \xrightarrow{\kappa_\mathrm{h}} \{1,0\} + \mathrm{E} \tag{8}$$

iv. recombination in photocatalyst

$$\{1,1\} \xrightarrow{\kappa_\mathrm{r}} \{0,0\} \tag{9}$$

Thus, each particle is identified by the number of containing *m* electrons and *n* holes as $\{m,n\}$, and, for example, the oxidation of a molecule can be determined as the transition of the particle state from $\{m,n\}$ to $\{\mathrm{m},(n\text{-}1)\}$. By numerically solving the simultaneous equation for $\mathrm{d}\{m,n\}/\mathrm{dt}$ under a constant excitation rate of *g*, the oxidation rate r_D was calculated by summing up $n\kappa_\mathrm{h}$ for all $\{m,n\}$ states over *m* and *n* [21]. As the result, the oxidation rates were analyized as a function of these four parameters, *g*, κ_e, κ_h, and κ_r. Well known light intensity (*I*) dependence of the oxidation rate $r_\mathrm{D} \propto I^{1//2}$ could be recognized when the excitation rate *g* is larger than the reduction rate κ_e, where $\kappa_\mathrm{e} \ll \kappa_\mathrm{r}$ should be hold [21].

By assuming that the oxidation takes place for the adsorbed molecule $\mathrm{D_{ad}}$, the oxidation rate could be given by $\kappa_\mathrm{h}=k_\mathrm{h}[\mathrm{D_{ad}}]$. For usual decomposition of organic molecules, O_2 is reduced. Therefore, the reduction rate can be given by $\kappa_\mathrm{e}=k_\mathrm{e}[\mathrm{O_{2,ad}}]$. Thus, the oxidation rate *r* could be given by the form of Langmuir-Hinshelwood kinetics Eq (10) as a function of reactant concentration [D] with two parameters of r_L and K_L.

$$r = \frac{r_\mathrm{L} K_\mathrm{L}[\mathrm{D}]}{1+K_\mathrm{L}[\mathrm{D}]} \tag{10}$$

The initial oxidation rate r measured for various reactant concentrations [D] under a certain light intensity can be analyzed by Eq(10) to obtain the values of r_L and K_L.

The adsorption constant K_L obtained at the various light intensities, I, could be expressed by Eq(11).

$$K_L = \frac{\frac{k_a}{k_d} + c_a I^2}{1 + c_d I^2} \tag{11}$$

Where, k_a and k_d are the rate constants for adsorption and desorption of D in the dark, and the effects of light intensity I on the adsorption and desorption rates are given by the two parameters c_a and c_d, respectively. It was revealed that I^2 is effective on K_L, though simple dependence on the adsorption or desorption in the form of I was discussed in literature [45, 46]. This observation suggests that one photon process causes no effect on the surface property, but only when two photons were absorbed in the particle, the adsorption property can be affected.

The intrinsic reaction rate r_L in Eq (10) is given by Eqs (12-14).

$$r_L = \frac{\beta \chi_1}{2\eta_1}\left[-1 + \sqrt{1 + (4{\eta_1}^2/\chi_1)I}\right] \tag{12}$$

$$\chi_1 = \frac{k_e[O_{2,ad}]k_h[S_D]}{k_r \beta} \tag{13}$$

$$\eta_1 = \frac{k_e[O_{2,ad}] + k_h[S_D]}{k_e[O_{2,ad}] + k_h[S_D] + k_r} \tag{14}$$

where, the unit of χ_1 is the same as that of the light intensity I, and β plays a role to convert the unit of χ_1 to the reaction rate in the experimental system. $[S_D]$ is the total concentration of the adsorption site for D, and k_r is the recombination rate. By using Eqs (10-14), dependencies of the reactant concentration [D] and light intensity I could be analyzed separately. In the conventional analysis by using the concentration for electrons and holes, the quadratic equation similar to Eq (12) has been reported [45, 46]. However, the intrinsic quantum yield η_1 in the equation was not the form of η_1^2 but η_1. This difference is the key point obtained from the 2D-laddar kinetic analysis to separate r_L and K_L in the I dependence [21].

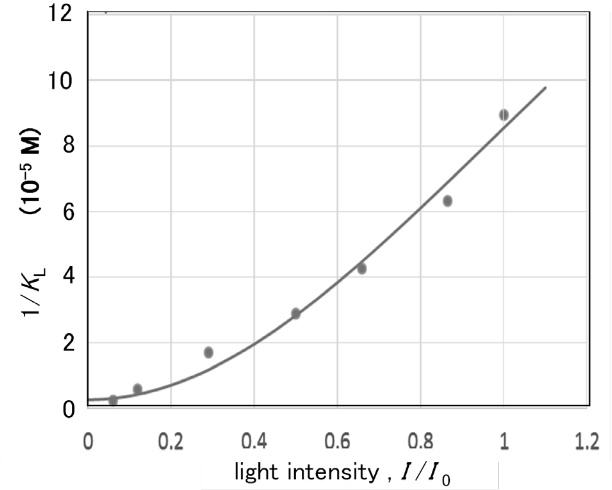

Figure 10. Association constant K_L in Langmuir-Hinshelwood equation Eq (10) obtained experimentally at various light intensities I [48]. The curve was calculated with Eq (11) by fitting the parameters k_a/k_d, c_a, and c_d. Reproduced with permission from Ref [21]. Copyright 2018 American Chemical Society.

The experimental data of $1/K_L$ for the decomposition of phenol in TiO_2 (P25) aqueous suspension at various light intensity have been reported in literature [48]. These data were replotted in Figure 10, and Eq (11) was fitted to determine the parameters k_a/k_d, c_a, and c_d.

The reaction rates reported as a function of the light intensity for several reactant concentrations [D] are plotted in Figure 11. These experimental data could be simulated by using Eqs (10-12). By fitting the calculated curves to the experimental data, the remained three parameters for Eq (12), that is, β, χ_1, and η_1, could be evaluated [21].

Since the lifetime of electrons is usually longer than that of holes, the relationship of $k_h[S_D] \gg k_e[O_{2,ad}]$ holds. Then, in the case of phenol oxidation, the $k_e[O_{2,ad}]$ is calculated with Eqs (13,14) to be 6×10^{-7}mol min^{-}

^{1} from the values of β, χ_1, and η_1 of Figure 11. On the other hand, the rates of $\bullet O_2^-$ production in air saturated solution could be measured by means of a chemiluminescence technique [49]. Thus, the O_2 reduction rate obtained by analyzing the reported data was found to be compatible to the $\bullet O_2^-$ formation rate measured experimentally [21].

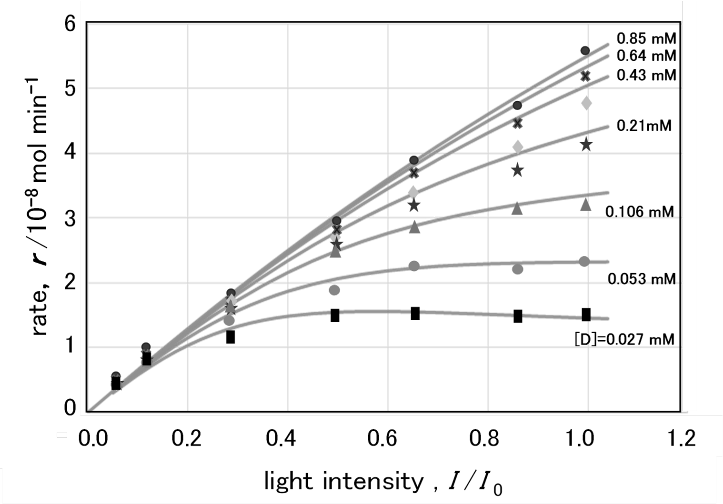

Figure 11. The decomposition rates for phenol was plotted as a function of the incident light intensity for various reactant concentrations [48]. The curves were calculated with Eqs (10-12) by fitting parameters β, χ_1, and η_1 to the experimental data. Reproduced with permission from Ref [21]. Copyright 2018 American Chemical Society

The present equations were also applied to the datasets of the photocatalytic oxidation of 4-chlorophenol reported by Mills and co-workers [46]. As the result, we could simulate the experimental data with Eqs (10-14). By substituting the obtained three parameters, β, χ_1, and η_1, for Eqs (13,14), $k_e[O_{2,ad}]$ is calculated to be 1.1×10^{-5} mol min^{-1}. The obtained $k_e[O_{2,ad}]$ is extremely larger than that for the phenol decomposition stated above. Since $HClO_4$ was added for the 4-chlorophenol decomposition, the extremely faster reduction suggests that ClO_4^- ions might be reduced in place of O_2 in their experiments.

CONCLUSION

Following issues are the peculiarities in photocatalytic reactions, which may have been overlooked in many reports.

Almost all photocatalytic reactions are irreversible reactions because the electron transfer (ET) reaction should have be finished before the electron-hole recombination, while reversible reactions are mainly treated in electrochemistry where electrons can be supplied from the electric source along the lead-wire. In photocatalysis, the ET reaction is not usually rate determining step, but it should competes with the fast carrier recombination, and the reaction rate is measured by the decomposition of the reactant or the formation of the products. Therefore, energy dependence on the ET kinetics based on the Marcus-Gerischer theory which was developed for electrode reactions may not be simply applied in photocatalysis.

The electric potential produced around the surface hole in air should be same as that in water, whereas for the electrode reactions the electrolyte solution is indispensable to polarize the solid surface.

Photoinduced electron-hole pair is generated in the same photocatalyst crystallite, and the concentrations of each carrier could not be treated independently for kinetic analysis.

REFERENCES

[1] Nosaka, Y. and Nosaka, A. (2016). *Introduction to Photocatalysis - From Basic Science to Applications,* Royal Society of Chemistry, Cambridge.

[2] Schneider, J., Bahnemann, D., Ye, J., Gianluca, L. P. and Dionysiou, D. D. eds (2016) *Photocatalysis: Complete Set (Energy and Environment Series)* Royal Society of Chemistry, Cambridge.

[3] Pichat, P. eds (2013) *Photocatalysis and Water Purification,* Wiley-VCH Verlag GmbH, Weinheim.

[4] Houmam, A. (2008) Electron transfer initiated reactions: Bond formation and bond dissociation. *Chem. Rev.*, 108: 2180–2237.

[5] Antonello, S. and Maran, F. (1999) The role and relevance of the transfer coefficient α in the study of dissociative electron transfers: Concepts and examples from the electroreduction of perbenzoates. *J. Am. Chem. Soc.*, 121: 9668–9676.

[6] Nosaka, Y. and Nosaka, A. Y. (2020) Intrinsic nature of photocatalysis by comparing with electrochemistry. *Phys. Chem. Chem. Phys.*, 22: 7146-7154.

[7] Huang, Z.-F., Song, J., Du, Y., Xi, S., Dou, S., Nsanzimana, J. M. V., Wang, C., Xu, Z. J. and Wang, X. (2019) Chemical and structural origin of lattice oxygen oxidation in Co–Zn oxyhydroxide oxygen evolution electrocatalysts. *Nature Energy*, 4: 329–338.

[8] Nosaka, Y. and Nosaka, A. Y. (2017). Generation and detection of reactive oxygen species in photocatalysis. *Chem. Rev.* 117: 11302−11336.

[9] Marcus, R. A. (1965) On the theory of electron-transfer reactions. VI. Unified treatment for homogeneous and electrode reactions. *J. Chem. Phys.*, 43: 679–701.

[10] Marcus, R. A. (1990) Reorganization free energy for electron transfers at liquid-liquid and dielectric simiconductor-liquid interfaces. *J. Phys. Chem.*, 94: 1050–1055.

[11] Gerischer, H. (1969) Charge transfer processes at semiconductor-electrolyte interface in connection with problems of catalysis. *Surf. Sci.*, 18: 97–122. Doi: 10.1016/0039-6028(69)90269-6.

[12] Memming, R. (2015) *Semiconductor Electrochemistry*, 2nd Ed, Wiley-VCH Verlag GmbH, Weinheim.

[13] Schiffer, Z. J., Lazouski, N., Corbin, N. and Manthiram, K. (2019) Nature of the first electron transfer in electrochemical ammonia activation in a nonaqueous medium. *J. Phys. Chem. C*, 123: 9713-9720.

[14] Nakato, Y. (2016) *Electrochemistry. Basic Science for Solar Energy Conversion*, Tokyo Kagaku Dojin, Tokyo, (in Japanese)

[15] Gerischer, H. (1993) Photoelectrochemical catalysis of the oxidation of organic molecules by oxygen on small semiconductor particles with TiO_2 as an example. A new approach. *Electrochim. Acta*, 38: 3–9. Doi: 10.1016/0013-4686(93)80003-I

[16] Duonghong, D., Ramsden, J. and Grätzel, M. (1982) Dynamics of interfacial electron-transfer processes in colloidal semiconductor systems. *J. Am. Chem. Soc.*, 104: 2977–2985.

[17] Bahnemann, D. W., Hilgendorff, M. and Memming, R. (1997) Charge carrier dynamics at TiO_2 particles: Reactivity of free and trapped holes. *J. Phys. Chem. B*, 101: 4265-4275.

[18] Grela, M. A., Brusa, M. A. and Colussi, A. J. (1997) Harnessing excess photon energy in photoinduced surface electron transfer between salicylate and illuminated titanium dioxide nanoparticles *J. Phys. Chem. B,* 101: 10986-10989.

[19] Savéand, J.-M. (2000) Electron transfer, bond breaking, and bond formation. *Adv. Phys. Org. Chem.*, 35: 117–192.

[20] Costentin, C., Robert, M. and Savéant, J.-M. (2000) Stepwise and concerted pathways in thermal and photoinduced electron-transfer/bond-breaking reactions. *J. Phys. Chem. A*, 104: 7492–7501.

[21] Nosaka, Y. and Nosaka, A. Y. (2018) Langmuir-Hinshelwood and light-intensity dependence analyses of photocatalytic oxidation rates by two-dimensional-ladder kinetic simulation. *J. Phys. Chem. C*, 122: 28748–28756.

[22] Villarreal, T. L., Gómez, R., González, M. and Salvador, P. (2004) A kinetic model for distinguishing between direct and indirect interfacial hole transfer in the heterogeneous photooxidation of dissolved organics on TiO_2 nanoparticle suspensions, *J. Phys. Chem. B*, 108: 20278–20290.

[23] Tada, H., Jin Q. and Kobayashi, H. (2012) Prediction of the main route in the TiO_2-photocatalyzed degradation of organic compounds in water by density functional calculations. *ChemPhysChem*, 13: 3457–3461.

[24] Montoya, M. J. F., Peral, J. and Salvador, P. (2014) Comprehensive kinetic and mechanistic analysis of TiO_2 photocatalytic reactions according to the direct-indirect model: (I) Theoretical approach. *J. Phys. Chem. C*, 118: 14266–14275.

[25] Liu, B., Chao, X., Terashima, C., Fujishima, A. and Nakata, K. (2014) Thermodynamic and kinetic analysis of heterogeneous photocatalysis for semicondctor systems. *Phys. Chem. Chem. Phys*., 16: 8751–8760.

[26] Kisch, H. (2013) Semiconductor photocatalysis - Mechanistic and synthetic aspect. *Angew. Chem. Int. Ed.,* 52: 812–847.

[27] Montoya, J. F., Velásquez, J. A. and Salvador, P. (2009) The direct–indirect kinetic model in photocatalysis: A reanalysis of phenol and formic acid degradation rate dependence on photon flow and concentration in TiO_2 aqueous dispersions. *Appl. Catal. B,* 88: 50–58.

[28] Yang, Y., Kang, Y., Zhao, H., Dai, X., Cui, M., Luan, X., Zhang, X., Nie, F., Ren, Z. and Song, W. (2020) An interfacial electron transfer on tetrahedral $NiS_2/NiSe_2$ heterocages with dual-phase synergy for efficiently triggering the oxygen evolution reaction. *Small*, 16(1): 1905083. Doi:10.1002/smll.201905083.

[29] Huang, X., Wang, J., Tao, H. B., Tiana, H. and Xu, H. (2019) An essential descriptor for the oxygen evolution reaction on reducible metal oxide surfaces. *Chem. Sci*., 10: 3340–3345.

[30] Yan, D., Li, Y., Huo, J., Chen, R., Dai, L. and Wang, S. (2017) Defect chemistry of nonprecious-metal electrocatalysts for oxygen reactions. *Adv. Mater*., 29: 1606459.

[31] Bourikas, K., Kordulis, C. and Lycourghiotisern, A. (2014) Titanium dioxide (anatase and rutile): Surface chemistry, liquid−solid interface chemistry, and scientific synthesis of supported catalysts. *Chem. Rev*., 114: 9754−9823.

[32] Bockris, J. O. and Reddy, A. K. N. (1970) *Modern Electrochemistry*, Vol. 2, Plenum press, New York.

[33] Nosaka, A. Y. and Nosaka, Y. (2005) Characteristics of water adsorbed on TiO_2 photocatalytic surfaces as studied by ^{1}H-NMR

spectroscopy. *Bull. Chem. Soc. Jpn.*, 78:1595–1607. DOI 10.1246/bcsj.78.1595.

[34] Buda, M. (2013) On calculating reorganization energies for electrochemical reactions using density functional theory and continuum solvation models. *Electrochim. Acta*, 113: 536– 549.

[35] Royea, W. J., Hamann, T. W., Brunschwig, B. S. and Lewis, N. S. (2006) A comparison between interfacial electron-transfer rate constants at metallic and graphite electrodes. *J. Phys. Chem. B*, 110: 19433–19442.

[36] Ward, M. D., White, J. R. and Bard, A. J. (1983) Electrochemical investigation of the energetics of particulate titanium dioxide photocatalysts. The methylviologen-acetate system. *J. Am. Chem. Soc.*, 105: 27–31.

[37] Di Paola, A., Bellardita, M., Ceccato, R., Palmisano, L. and Parrino, F. (2009) Highly active photocatalytic TiO_2 powders obtained by thermohydrolysis of $TiCl_4$ in water. *J. Phys. Chem. C*, 113: 15166–15174.

[38] Ikeda, S., Sugiyama, N., Murakami, S., Kominami, H., Kera, Y., Noguchi, H., Uosaki, K., Torimoto, T. and Ohtani, B. (2003) Quantitative analysis of defective sites in titanium(IV) oxide photocatalyst powders. *Phys. Chem. Chem. Phys.*, 5: 778–783.

[39] Yamakata, A. and Matsunaga, H. (2019) Curious behaviors of photogenerated electrons and holes at thedefects on anatase, rutile, and brookite TiO_2 powders: A review. *J. Photochem. Photobiol. C. Photochem. Rev.*, 40: 234−243.

[40] Mansfeldova, V., Zlamalova, M., Tarabkova, H., Janda, P., Vorokhta, M., Piliai, L.and Kavan, L. (2021) Work function of TiO_2 (anatase, rutile, and brookite) single crystals: Effects of the environment. *J. Phys. Chem. C*, 125: 1902–1912.

[41] Pfeifer, V., Erhart, P., Li, S., Rachut, K., Morasch, J., Brotz, J., Reckers, P., Mayer, T., Ruhle, S., Zaban, A., Sero, I. M., Bisquert, J., Jaegermann, W. and Klein, A. (2013) Energy band alignment between anatase and rutile TiO_2. *J. Phys. Chem. Lett.,* 4: 4182−4187.

[42] Scanlon, D. O., Dunnill, C. W., Buckeridge, J., Shevlin, S. A., Logsdail, A. J., Woodley, S. M., Catlow, C. R. A., Powell, M. J., Palgrave, R. G., Parkin, I. P., Watson, G. W., Keal, T. W., Sherwood, P., Walsh, A. and Sokol, A. A. (2013) Band alignment of rutile and anatase TiO_2. *Nat. Mater.*, 12: 798−801.

[43] Nosaka, Y. and Nosaka, A. Y. (2016) Reconsideration of intrinsic band alignments within anatase and rutile TiO_2. *J. Phys. Chem. Lett.*, 7: 431–434.

[44] Muñoz-Batista, M. J., Ballari, M. M., Kubacka, A., Alfano, O. M. and Fernández-García, M. (2019) Braiding kinetics and spectroscopy in photo-catalysis: the spectro-kinetic approach. *Chem. Soc. Rev.*, 48: 637-682.

[45] Mills, A. and O'Rourke, C. (2015) Revised disrupted Langmuir−adsorption model of photocatalysis. *J. Phys. Chem. C*, 119: 19941–19946.

[46] Mills, A., O'Rourke, C. and Moore, K. (2015) Powder semiconductor photocatalysis in aqueous solution: An overview of kinetics-based reaction mechanisms. *J. Photochem. Photobiol.* A, 310: 66−105.

[47] Nosaka, Y., Ohta, N. and Miyama, H. (1990) Photochemical kinetics of ultrasmall semiconductor particles in solution: Effect of size on the quantum yield of electron transfer. *J. Phys. Chem.*, 94: 3752-3755.

[48] Emeline, A. V., Ryabchuk, V. and Serpone, N. (2000) Factors affecting the efficiency of a photocatalyzed process in aqueous metal-oxide dispersions: Prospect of distinguishing between two kinetic models. *J. Photochem. Photobiol. A*, 133: 89−97.

[49] Hirakawa, T., Yawata, K. and Nosaka, Y. (2007) Photocatalytic reactivity for $O_2{\bullet}^-$ and OH• radical formation in anatase and rutile TiO_2 suspension as the effect of H_2O_2 addition. *Appl. Catal. A*, 325: 105−111.

In: Fundamentals of Photocatalysis
Editor: Orva Auger
ISBN: 978-1-68507-374-9

Chapter 3

ZNO-CDO NANOBLOCKS: UTILIZATION AS ADSORBENT AND EFFICIENT SOLAR PHOTO-CATALYST TOWARDS BRILLIANT CRESOL BLUE DEGRADATION

Mohammed M. Rahman[1,]*, Jahir Ahmed[2],
Abdullah M. Asiri[1] and Md Humayun Kabir[3]
[1]Center of Excellence for Advanced Materials Research (CEAMR),
King Abdulaziz University, Jeddah, Saudi Arabia;
[2]Promising Centre for Sensors and Electronic Devices (PCSED),
Advanced Materials and Nano-Research Centre, Najran University,
Najran, Saudi Arabia
[3]Department of Chemistry and Occupational Health Science,
University of North Alabama, Florence, AL, USA

---

* Corresponding Author's E-mail: mmrahman@kau.edu.sa; mmrahmanh@gmail.com.

ABSTRACT

Here, ZnO-CdO nanoblocks (NBs) have been prepared by facile wet-chemical technique at low-temperature and characterized by UV–vis., FT-IR, XRD, FESEM, XPS, and XEDS etc. The NBs were used and applied for the selective detection of Fe(III) ions as an efficient adsorbent as well as active photo-catalytic degradation using Brilliant cresol blue (BCB). The detection efficiency of NBs phase was also investigated for a selective detection of Fe(III) by Inductively coupled plasma - optical emission spectrometry (ICP-OES). NBs were found the most selective towards Fe(III), where adsorption process was mainly monolayer on a homogeneous adsorbent surface. In photo-catalysis, almost 52.3% degradation with BCB dye was observed under solar irradiation with NBs.

Keywords: photocatalyst, ZnO-CdO nanoblocks, optical properties, photo-degradation, brilliant cresol blue, environmental remediation

INTRODUCTION

Nanostructures offer particular patterns for the growth of doped-materials with promising optical, electro-chemical, opto-electronic and magnetic properties compared to un-doped nanomaterials. In nature, semiconductors displays enormously high absorb behaviours based on the band-gap energy. The exceptional nanostructure of doped morphology allows them to absorb the solar-lights and promote photo-catalysis with higher efficiency [1-2]. Considering the solar-light absorption of the nano-structures, it is intended simulated block-structures to act as photo-catalysts as well as solid phase adsorbent with higher capacity and sensitivity. Removal of organic dye contaminants (especially BCB dye) in water has been a considerable issue in wastewater treatment because of the non-biodegradable nature of the pollutants using nanostructure materials. The degradation techniques, such as, adsorption using activated-carbon and coagulation using coagulants, actively convert the aqueous dyes to the solid state leaving the contaminant intact. During the past decades, many researchers have put focus on searching for a direct and effective technique to resolve this problem [3-9]. Recently scientists have studied the photo-catalytic degradation of toxic organic dyes using photo-catalysts typically with semiconducting materials (i.e., titanium oxide, zinc oxide, cobalt oxide, cerium oxide etc) in UV/visible and xenon beams [10-13]. Our attempt was to study the photo-catalytic degradation of BCB organic dye (water soluble) with calcined doped ZnO-CdO NBs in aqueous system under solar light sources. The mechanism comprised heterogeneous photo-catalytic oxidation has been executed thoroughly in this study.

In addition, the growth of simple, rapid and efficient methods has become of interest for monitoring toxic metal ions contaminants in the environment. Several analytical methods have been applied to analyze metal ions in aqueous solutions, such as atomic absorption spectrometry [14], inductively coupled plasma-optical emission spectrometry (ICP-OES) [15], anodic stripping voltammetry [16], and ion chromatography [17]. However, analytical methods can not directly measure metal ions, in particular at ultra-trace concentration, in aqueous systems due to the lack of sensitivity and selectivity of these methods. Therefore, an efficient separation procedure is usually required prior to the determination of noble metals for sensitive, accurate and interference-free determination of noble metals [18]. Several analytical methods can be used for separation of analyte of interest, including liquid–liquid extraction, ion exchange, coprecipitation, cloud point extraction and solid phase extraction (SPE) [19-23]. SPE is considered to be one of the most powerful techniques because it minimizes solvent usage and exposure, disposal costs, and extraction time for sample preparation. Several adsorbents have appeared because of the popularity of SPE for selective extraction of analytes, such as alumina [24], C18 [25], molecular imprinted polymers [26], cellulose [27], silica gel [28], activated carbon [29, 30] and carbon nanotubes [31, 32]. In accordance, the purpose of this experiment was to examine the analytical potential of doped ZnO-CdO NBs as solar photo-catalysts and solid-phase adsorbent on the photo-degradation and adsorption capacity of BCB dye and Fe(III) ions respectively. The selectivity of ZnO-CdO NBs towards different metal ions, including Cd(II), Co(II), Cr(III), Cu(II), Fe(III), Ni(II) and Zn(II), was assessed in order to study the effectiveness of NBs onto the adsorption of selected metal ions. Based on the selectivity study, it was concluded that the selectivity of NBs phase was the most towards Fe(III). The static uptake capacity for Fe(III) was determined to be ~110.80 mgg^{-1}. Results of adsorption isotherm also confirmed that the adsorption process was mainly monolayer on a homogeneous adsorbent surface. Adsorption data of Fe(III) were well fit with the Langmuir classical adsorption isotherm.

EXPERIMENTAL SECTIONS

Materials and Methods

Cadmium nitrate [$Cd(NO_3)_2$], Zinc nitrate [$Zn(NO_3)_2$], sodium hydroxide (NaOH), and all other chemicals were used in analytical grade and purchased from Sigma-Aldrich Company (www.sigmaaldrich.com). Stock standard solutions of 1000.0 mgL^{-1} Cd(II), Co(II), Cr(III), Cu(II), Fe(III), Ni(II), and Zn(II) were purchased from Sigma-Aldrich (Milwaukee, WI, USA). All reagents used were of analytical and spectral purity grade. Doubly distilled de-ionized water was also used throughout experimental studies. The doped ZnO-CdO NBs was investigated with UV/visible spectroscopy (Lamda-950, Perkin Elmer, www.perkinelmer.com). The λ_{max} (315.0 nm) of calcined doped ZnO-CdO NBs was investigated with UV/visible spectroscopy (UVO-2960, www.labomed.com). FT-IR spectra were measured for doped ZnO-CdO NBs with a spectrophotometer (Spectrum-100 FT-IR) in the mid-IR range, which was obtained from Perkin Elmer, Germany (www.perkinelmer.com). The powder X-ray diffraction (XRD) prototypes were checked with X-ray diffractometer (XRD; X'Pert Explorer, PANalytical diffractometer; www.panalytical.com) prepared with CuKα1 radiation (λ=1.5406 nm) using a generator voltage of 40.0 kV and current of 35.0 mA applied for the measurement. Morphology of doped ZnO-CdO NBs was evaluated on FESEM instrument (FESEM; JSM-7600F, Japan;

www.jeol.com). Elemental analysis of doped ZnO-CdO NBs was done using XEDS from JEOL, Japan. The X-ray photoelectron spectroscopy (XPS) measurements were executed for ZnO-CdO NBs on a Thermo Scientific K-Alpha KA1066 spectrometer (www.thermoscientific.com). ICP-OES investigation was performed by using of a Perkin Elmer ICP-OES model Optima 4100 DV (www.perkinelmer.com). The ICP-OES instrument was optimized daily before measurement and operated as recommended by the manufacturers. The ICP-OES spectrometer was used with following parameters, such as FR power (1300.0 kW), frequency (27.12 MHz), demountable quartz torch (Ar/Ar/Ar), plasma gas (Ar) flow (15.0 $Lmin^{-1}$), auxiliary gas (Ar) flow (0.2 $Lmin^{-1}$), nebulizer gas (Ar) flow (0.8 $Lmin^{-1}$), nebulizer pressure (2.4 bar), glass spray chamber according to Scott (Ryton), sample pump flow rate (1.5 $mLmin^{-1}$), integration time (3.0 s), replicates (3), wavelength range of monochromator (165~460 nm) etc. Selected metal ions were investigated at wavelengths of 228.80 nm for Cd(II), 238.90 nm for Co(II), 267.72 nm for Cr(III), 327.39 nm for Cu(II), 259.94 nm for Fe(III), 221.65 nm for Ni(II) and 206.20 nm for Zn(II).

Synthesis and Growth Mechanism of Doped ZnO-CdO NBs

Doped nanostructure materials have been prepared by adding uni-molar concentration of cadmium nitrate and zinc nitrate as starting materials into reactant cell for 12 hours. The precursors of codoped materials [$Cd(NO_3)_2$ (0.1M) and $Zn(NO_3)_2$ (0.1M)] are soluble in aqueous system. Initially cadmium nitrate and zinc nitrate were gradually dissolved into the de-ionized water to form 0.1 M concentration separately at room temperature. Then these uni-molar (Cd-sol:Zn-sol::0.1M:0.1M) solutions were mixed dynamically and shaken until merge appropriately. Then the mixture solution pH is properly adjusted (~10.5) by using prepared NaOH (0.5M) and kept onto the hot-plate at 150.0°C for 8 hours. The starting materials of zinc nitrate and cadmium nitrate were utilized without further purification for co-precipitation technique to codoped (ZnO-CdO) composition. Again reducing agent, NaOH was added drop-wise into the vigorously stirred zinc nitrate and cadmium nitrate solutions mixture to produce a significant codoped precipitate.

The growth mechanism of the doped ZnO-CdO nanomaterials can be explicated on the basis of chemical reactions and nucleation as well as growth of ZnO-CdO NBs. The probable reaction mechanisms are proposed for achieving the codoped nanomaterials, which is proposed in below.

$$NaOH \rightarrow Na^{+}_{(aq)} + OH^{-}_{(aq)} \quad (1)$$

$$Zn(NO_3)_2 + 2NaOH + H_2O \rightarrow$$
$$Zn(OH)_{2(aq)} + 2Na^{+}_{(aq)} + NO_3^{-}{}_{(aq)} + H_2O \quad (2)$$

$$Cd(NO_3)_2 + 2NaOH \rightarrow Cd(OH)_{2(aq)} + 2Na^{+}_{(aq)} + NO_3^{-}{}_{(aq)} \quad (3)$$

$$Zn(OH)_{2(aq)} + NaOH_{(aq)} + Cd(OH)_{2(aq)} \rightarrow$$
$$CdO\text{-}ZnO_{(s)}\downarrow + Na^{+} + OH^{-} + H_2O \quad (4)$$

The reaction is advanced steadily according to the proposed equation (1) to equation (4). During preparation, pH plays a major role in the codoped nanomaterial formation. At a particular pH, when $Zn(NO_3)_2$ and $Cd(NO_3)_2$ is hydrolyzed with reducing agent (NaOH), unstable zinc hydroxide and cadmium hydroxide is formed instantly according to the equation (2). During the whole synthesis route, NaOH operates a pH buffer to control the pH value of the solution and slow contribute of OH^- ions. When the concentrations of the Zn^{2+}, Cd^{2+}, OH^- ions are go above in critical value, the precipitation of ZnO-CdO nuclei begin to start. As there is high concentration of Cd^{2+} ion in the reaction system, the nucleation of ZnO crystals become easier due to the lower activation energy barrier of heterogeneous nucleation. However, as the concentration of Cd^{2+} existences, a number of larger ZnO-CdO crystals with an aggregated particle-like morphology form among the nanostructures.

The shape of calcined ZnO-CdO nanomaterials is around reliable with the growth pattern of doped selective crystals [33, 34]. Then the solution was washed thoroughly with ethanol and acetone, and kept for drying at room temperature. Finally, the as-grown ZnO-CdO nanomaterials were calcined at 450.0°C for 4 hours in the furnace (Barnstead Thermolyne, 6000 Furnace, USA). In nanoblocks growth method, initially CdO and ZnO nucleus growth takes place by self- & mutual-aggregation, which nano-crystal then re-aggregates and formed aggregated ZnO-CdO nanocrystal using Ostwald ripening method. Nanocrystal crystallizes and re-aggregates with each other counter parts through Vander-Waals forces and reforms doped ZnO-CdO NBs morphology, which is presented in Scheme 1. The calcined doped products were characterized in detail in terms of their morphological, structural, optical properties, elemental and applied for metal ion uptakes.

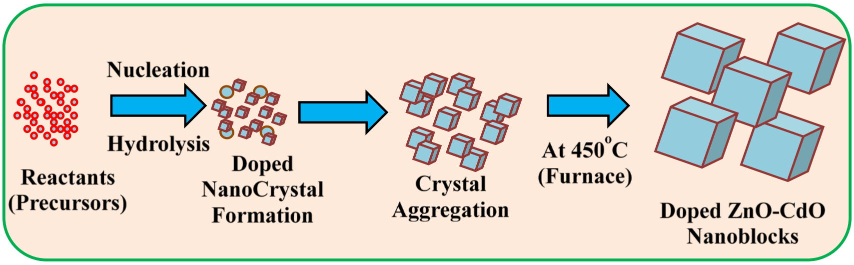

Scheme 1. Schematic representation of growth mechanism of calcined ZnO-CdO NBs via. wet-chemical process.

Photocatalytic Degradation of BCB with Doped ZnO-CdO NBs

Photo-degradation of BCB using calcined ZnO-CdO NBs was investigated by UV/visible spectroscopy at room conditions. The photo-catalytic reaction was carried out in a 250.0 ml beaker, which contain 150.0 ml of BCB dye solution (0.01 mM) and 150.0 mg of ZnO-CdO NBs catalyst.

Before the photo-irradiation, the mixture solution was stirred gently for at least 10 min in the dark to allow equilibrium of the system so that loss of compound due to the adsorption can be taken into account. The suspension was continuously purged with oxygen bubbling throughout the experiment. Irradiation was carried out under solar light. Samples (3.0 ml) were taken before and at usual intervals during the irradiation (10.0 mins) and BCB solution were isolated from the photo-catalysts by centrifugation before measurement of UV/visible analysis. The photo-degradation was executed by measuring the absorbance using UV-visible spectrophotometer (UVO-2960). The absorbance of BCB (0.01 mM) was followed at 315.0 nm wavelength. All solutions were made and organized with de-ionized water in room conditions.

Samples Preparation and Procedure for Metal Ions Uptakes Using ZnO-CdO NBs

Stock solutions of Cd(II), Co(II), Cr(III), Cu(II), Fe(III), Ni(II) and Zn(II) were made in 18.2 MΩ·cm distilled deionized water and stored in the dark at 4.0°C. For selectivity study, standard solutions of 5.0 mgL^{-1} of each metal ions were prepared and adjusted at 5.0 pH value with acetate buffer. Then, each standard solution was individually mixed with 25.0 mg of ZnO-CdO NBs. In this study, a fixed pH (~5.0) was chosen for all metal ions in order to avoid any precipitation of other species, in particular for Fe(III). For example, Fe(III) usually forms a precipitation of $Fe(OH)_3$ with buffer solutions at pH value greater than 5.0. For the study of Fe(III) static adsorption capacity, standard solutions of 0, 5.0, 10.0, 15.0, 20.0, 25.0, 30.0, 50.0, 75.0, 125.0, and 150.0 mgL^{-1} were prepared as above, adjusted to the optimum pH value of 5.0 and individually mixed with 25.0 mg ZnO-CdO NBs. All mixtures were mechanically shaken for 1.0 h at room temperature.

RESULTS AND DISCUSSION

Characterization of Doped ZnO-CdO NBs

The optical property of the codoped ZnO-CdO NBs is one of the significant features for the assessment of its photo-catalytic activity. Accordingly, optical properties of the calcined ZnO-CdO NBs were exposed using UV/visible spectro-photometer and presented in Figure 1a. UV/visible absorption spectrum exhibited absorption peak 315.0 nm, which is corresponded the characteristic absorption peak. No extra peak associated with impurities and structural defects are observed in the optical spectrums, which proved that the prepared NBs are well crystalline of ZnO-CdO NBs. Band gap energy is calculated on the sources of the highest absorption band of ZnO-CdO NBs and obtained to be ~3.9365 eV (E_{bg}), according to the following equation (5).

$$E_{bg} = \frac{1240}{\lambda} \text{ (eV)} \tag{5}$$

where E_{bg} is the band-gap energy and λ_{max} is the wavelength (~315.0 nm) of the ZnO-CdO NBs. As can been observed, the optical E_{bg} of doped ZnO-CdO NBs is ~3.8390, which is in good conformity with the ZnO codoped CdO band structure [35, 36]. This proposed that the ZnO-CdO NBs are transition-codoped semiconductor with measured energy-value. E_{bg} is accredited to inter-band (conduction and valance band) doped transition and considered as the accurate energy gap.

The doped ZnO-CdO NBs are also demonstrated from the atomic and molecular vibrations. To expect the aggravated recognition, FT-IR spectra basically in the region of 400-4000 cm^{-1} are investigated. Figure 1b displays the FT-IR spectrum of the calcined ZnO-CdO NBs. It exhibits a band at ~676.0 cm^{-1}. These observed wide-vibration bands (~676.0 cm^{-1}) could be assigned as metal-oxygen (Cd-O and Zn-O modes) stretching vibrations respectively [37], which verified the formation of codoped nanocomposite materials. Finally, the observed vibration bands at low frequencies regions suggested the formation of doped ZnO-CdO NBs.

The doped ZnO-CdO NBs were analyzed and exhibited as wurtzite structure with hexagonal shapes. The sample was calcined at ~450.0°C in furnace for the formation of nano-crystalline phases. Figure 1c shows typical crystallinity of calcined ZnO-CdO NBs and their aggregation. All the reflection peaks in this prototype were found to match with ZnO phase (zincite) having hexagonal geometry [Joint Committee on Powder Diffraction Standards, JCPDS # 071-6424]. The phases showed the major characteristic peaks (star symbol, *) with indices for crystalline ZnO at 2θ values of 31.2(101), 33.8(002), 48.1(102), 638(103), and 81.2(312) degrees. The hexagonal (unit cell) lattice parameters are a = 3.2494, b = 5.2038, Point group: P63mc, and Radiation: CuKα1 (λ= 1.5406). These indicated that there is considerable amount of crystalline ZnO present in codoped nanocoposite materials. The diffraction patterns of doped NBs can be indexed to the hexagonal structure of ZnO [38]. The peaks were found to match with CdO phase having cubic geometry [39]. The major phases are indicated the characteristic peaks (Hash symbol, #) with indices for 2θ values at 33.7(111), 39.8(200), 56.8(311), and 60.8(201) degrees. These indicate that there is significant amount of crystalline CdO present in codoped nanocomposite materials. The other peaks of ZnO-CdO NBs related secondary phases were not exhibited in cadmium oxide sample, which may be attributed to the incorporation of ZnO into CdO lattice site. The crystalline size was also calculated and confirmed using Scherrer formula (6),

$$D = 0.9\lambda/(\beta\cos\theta) \tag{6}$$

where λ is the wavelength of x-ray radiation, β is the full-width at half maximum (FWHM) of the peaks at the diffracting angle θ. The average diameter of doped ZnO-CdO NBs is close to ~155.2 nm.

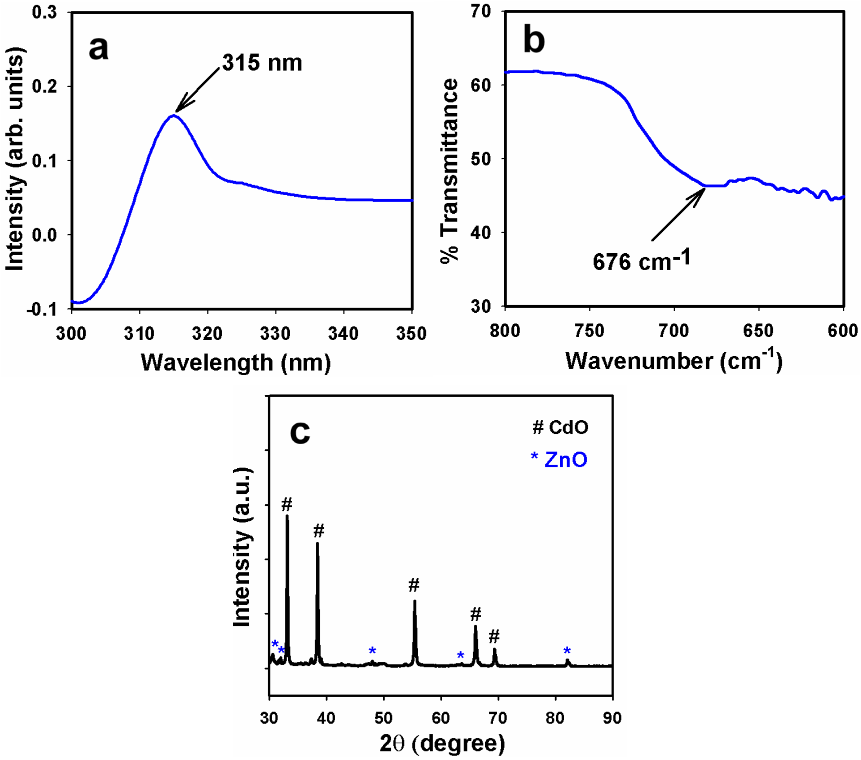

Figure 1. (a) UV/visible, (b) FT-IR spectroscopy, and (c) powder X-ray diffraction pattern of doped ZnO-CdO nanoblocks.

The general morphologies of the doped ZnO-CdO NBs are investigated using FESEM. High-resolution FESEM images (low-high magnification) of doped NBs are presented in Figure 2(a-b). The FESEM images are composed of nanostructure materials with cumulative structure in block-shape and reveals that the nano-blocks are grown in a very high density. The average diameter of doped ZnO-CdO NBs is 158.8 ± 10.0 nm in the range of 120.3 to 165.1 nm, which is calculated from Figure 2b. The nanostructures are arranged in such a particular manner that they are making a perfect block-shaped morphology. It was interesting to see that the diameters of the calcined NBs are almost uniform along their cross-section (diameter). It is also suggested that almost all of the products possessed in aggregated doped ZnO-CdO NBs. Excitingly, it was also observed that the major portion of these block-shaped structures have a perfectly hexagonal, which makes the nanostructures a block-like morphology (Figure 2b). When the size of codoped NBs material decreases into nanometer-sized scale, the surface area increases extensively, this develops the energy of the system, making the re-distribution of Zn, Cd, and O atoms in the crystalline phases. The nanometer-sized blocks could have tightly packed into the lattice, which is good agreement with the previous results on doped and undoped nanomaterials [40-45].

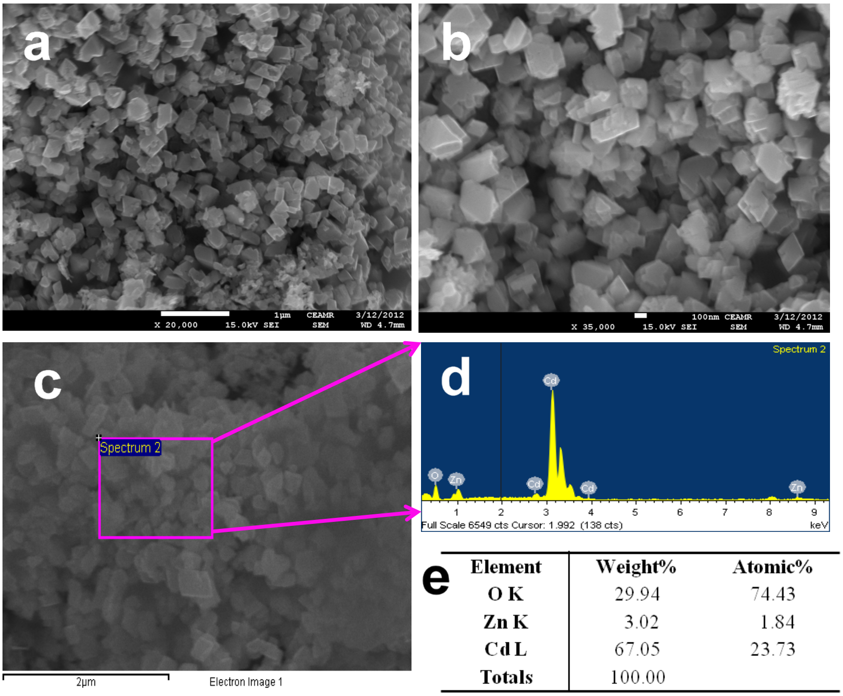

Element	Weight%	Atomic%
O K	29.94	74.43
Zn K	3.02	1.84
Cd L	67.05	23.73
Totals	100.00	

Figure 2. (a-b) low to high magnified FESEM images and (c-d) XEDS investigation (selective area, elemental signals with particular chemical-symbols, and (e) weight percentage in inset-table) of calcined ZnO-CdO NBs.

The X-ray energy dispersive spectroscopy (XEDS) investigation of doped ZnO-CdO NBs indicates the presence of Cd, Zn, and O composition in the pure calcined doped nanocomposite materials. It is clearly exhibited that calcined prepared materials controlled only cadmium, zinc, and oxygen elements, which presented in Figure 2(c-e). The composition of Cd, Zn, and O is 67.05%, 3.02%, and 29.94% respectively. No other peak related with any impurity has been detected in the XEDS, which confirms that the ZnO-CdO NBs products are composed only with Cd, Zn, and O.

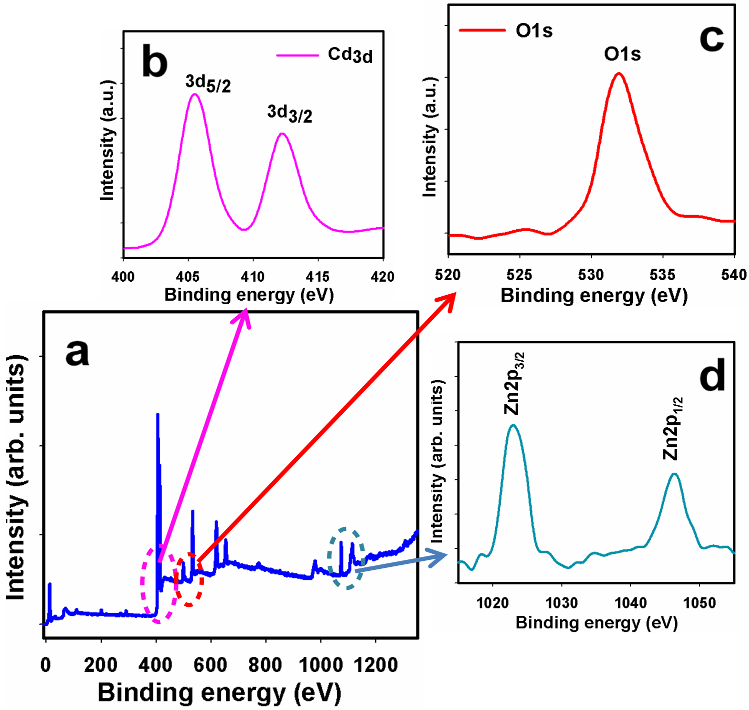

Figure 3. XPS of calcined (a) full-spectrum of NBs, (b) Cd3d level, (c) O1s level, and (d) Zn2p level acquired with MgKα1 radiations for nanostructure ZnO-CdO NB materials.

X-ray photoelectron spectroscopy (XPS) is a quantitative spectroscopic technique that examines the elemental-composition, empirical-formula, chemical-state, and electronic-state of the elements that present within a material. XPS spectra are acquired by irradiating a material with a beam of X-rays, while simultaneously determining the kinetic energy and number of electrons that get-away from the top one to ten nm of the material being analyzed. Here, XPS measurements were executed for doped ZnO-CdO NBs materials to examine the chemical states of CdO and ZnO. The XPS full-spectrum of doped ZnO-CdO NBs [Cd3d, Zn2p, and O1s] is presented in Figure 3a. In Figure 3b, the spin orbit peaks of the $Cd3d_{(5/2)}$ and $Cd3d_{(3/2)}$ binding energy for NBs appeared at around 405.6 eV and 412.9 eV respectively, which is in good agreement with the reference data for CdO [46]. The O1s spectrum shows a main peak at 532.5 eV, which is represented in Figure 3c. The peak at 532.5 eV is assigned to lattice oxygen, which is indicated to oxygen (ie, O_2^-) in presence in the doped ZnO-CdO NBs [47]. XPS was also used to resolve the chemical state of the doped ZnO NBs and their depth. Figure 3d presents the XPS spectra (spin-orbit peaks) of the $Zn2p_{(3/2)}$ and $Zn2p_{(1/2)}$ regions recorded with semiconductor NB doped materials. The binding energy of the $Zn2p_{(3/2)}$ and $Zn2p_{(1/2)}$ peak at 1024.3 eV and 1046.9 eV respectively denotes the presence of ZnO since their bindings energies are similar [48].

Photocatalytic Degradation of BCB Using ZnO-CdO NBs

The molecular structure and absorbance spectrum of BCB is presented in the Figure 4a and Figure 4b respectively. The photo-catalysis of the BCB dye occurs mainly on the doped ZnO-CdO NBs surface. The extent of degradation of the BCB dye was investigated by monitoring its concentration with and without NBs after reaching the degradation. Figure 4c shows the gradual decreasing in absorption spectra for the degradation of BCB dye with doped ZnO-CdO NBs as a function of photo-irradiation time (min). It is found that the irradiation of an aqueous suspension of BCB dye in the presence of doped ZnO-CdO NB leads to reduce in absorption spectra at 592.0 nm. The absorbance spectra at 592.0 nm is significantly decreased with increasing in exposure time (min) and slowly decrease until 120 min which concludes that the BCB dye has decolorization property with doped ZnO-CdO NBs close to 52.3%. The decrease in absorption intensity vs. irradiation time (min) for the BCB in the presence of doped ZnO-CdO NBs is shown in the Figure 4d. Figure 4e shows a plot for the % degradation vs. irradiation time (min) for the oxygen saturated aqueous suspension of BCB in the presence of doped ZnO-CdO NBs. Figure 4e shows that around 52.3% degradation of the BCB dye takes place after 120 min of irradiation in the presence of catalytic doped ZnO-CdO NBs. Finally, the degradation of BCB clearly demonstrated that prepared doped ZnO-CdO NBs (MOx) possess significant photo-catalytic activity and these NBs could be beneficial photo-catalysts for the removal of colored dyes.

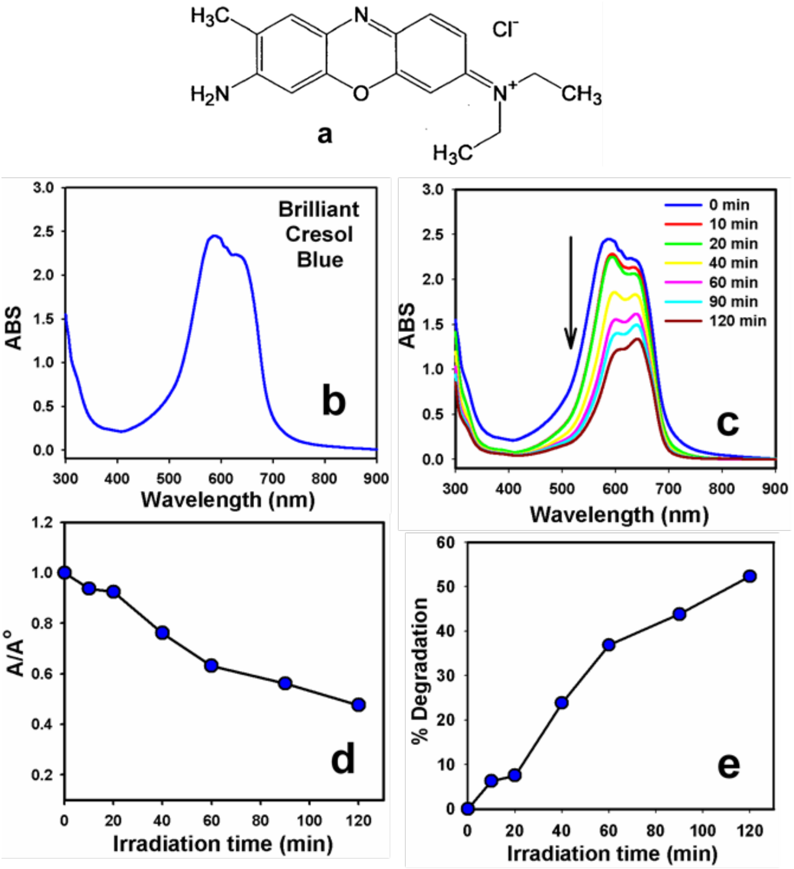

Figure 4. Photo-catalytic degradation of BCB using doped ZnO-CdO NBs. (a) Molecular structure of BCB; (b) Absorbance spectrum of aqueous solution of BCB; (c) Spectrum of BCB at different time interval (until 120 min); (d) Change in absorbance with irradiation time; (e) Percent degradation in different time intervals of BCB in presence of doped ZnO-CdO NBs materials.

The schematic representation of BCB dye degradation with doped ZnO-CdO NBs is presented in Figure 5. Mechanism of heterogeneous photo-catalysis has been discussed expansively in literature [49-51]. When a codoped semiconductor such as ZnO-CdO NBs (NB, MOx) absorbs a photon of energy equal to or greater than its band gap, there will be the formation of electron/hole pair (Figure 5). If charge separation is retained, the electron and hole may transfer to the doped NBs surface, which can ultimately bring about redox reactions of the organic substrates (BCB) dissolved in water in the presence of oxygen. During the photo-catalytic oxidation processes hydroxyl radicals ($^{\cdot}OH$) and super-oxide radical anions ($O^{\cdot}_2{}^-$) are supposed to be the main oxidizing species. These oxidative retorts would significance in the mineralization of the BCB dye. Alternatively, direct absorption of light by the dye named BCB, can lead to charge injection from the excited state of the BCB to the conduction band of the semiconductor (ZnO-CdO NBs) as summarized in the following equations (7-11):

$$NB_x + h\upsilon \rightarrow e^-_{cb} + h^+_{vb} \tag{7}$$

$$O_2 + e^-_{cb} \rightarrow {}^{\cdot}O^-_2 \tag{8}$$

$$H_2O + h^+_{vb} \rightarrow {}^{\cdot}OH + H^+ \tag{9}$$

$$BCB_{ads} + h\upsilon \rightarrow BCB_{ads}{}^* \tag{10}$$

$$BCB_{ads}{}^* + NB_x \rightarrow BCB_{ads}{}^+ + {}^{\cdot}NB_2(e^-) \tag{11}$$

The photo-degradation process was initiated by the photolysis of NBx-oxide/hydroxyl species, and accelerated by mercury beam irradiation, owing to enhance photolysis of NBs species, which enhances the regeneration of metal precursor with concomitant production of oxide free radicals.

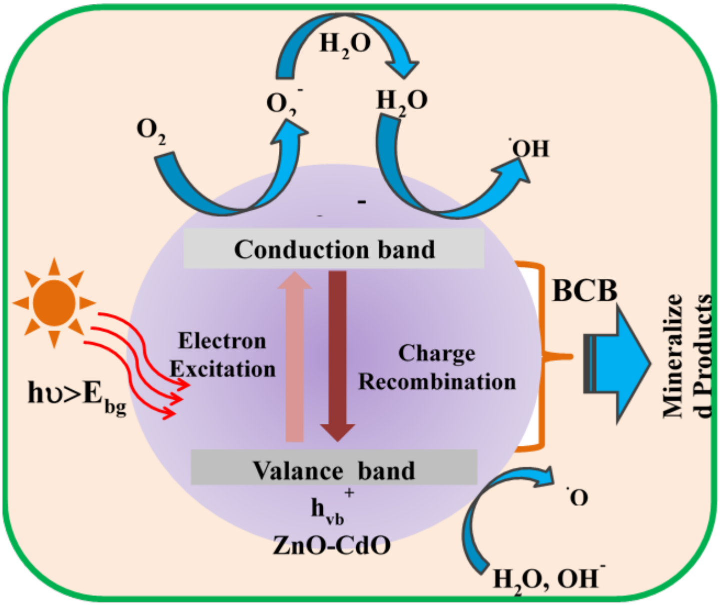

Figure 5. Schematic representation of photo-catalytic mechanism of BCB in presence of doped ZnO-CdO NBs under solar lights.

Hydroxyl radicals ($OH^·$) and superoxide radical anions ($O_2^{·-}$) contribute to the oxidation process by attacking the dye molecules and would results in the bleaching of the BCB dye. The results above clearly indicate that the prepared NBs shows a good photo-catalytic activity, thus it can be used as a photo-catalyst for the treatment of colored dyes in wastewater.

Metal Ions Uptakes Using Doped ZnO-CdO NBs (Batch Method)

Selectivity Study of Calcined ZnO-CdO NBs

Selectivity of the newly prepared doped ZnO-CdO NBs phase towards various metal ions was investigated based on determination of the distribution coefficient of NBs phase. The distribution coefficient (K_d) can be obtained from the following equation (xii) [52]:

$$K_d = (C_o - C_e / C_e) \times (V/m) \tag{12}$$

where C_o and C_e refer to the initial and final concentrations before and after filtration with doped ZnO-CdO NBs, respectively, V is the volume (mL) and m is the weight of ZnO-CdO NBs phase (g). Distribution coefficient values of all metal ions investigated in this study are reported Table 1.

Table 1. Selectivity study of doped ZnO-CdO NBs phase adsorption towards different metal ions at pH 5.0 and 25.0°C (N= 5)

Metal Ion	$q_e\,(mgg^{-1})$	K_d (mLg^{-1})
Fe(III)	5.00	4999000.00
Cu(II)	2.15	751.93
Cr(III)	1.60	471.89
Co(II)	1.08	275.18
Cd(II)	0.55	123.85
Ni(II)	0.40	86.72
Zn(II)	0.33	71.58

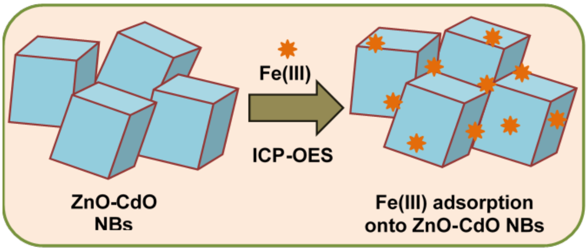

Figure 6. Schematic representation of Fe(III) ions uptake mechanism onto the doped ZnO-CdO NBs surfaces under room conditions.

It can be clearly noticed from Table 1 that the greatest distribution coefficient value was obtained for Fe(III) as compared to all metal ions. As shown in Table 1, the amount of Fe(III) was all extracted by doped ZnO-CdO NBs phase. Results of selectivity study provided that the newly synthesized calcined ZnO-CdO NBs phase was the most selective towards Fe(III) among all metal ions included in this study. Thus, codoped ZnO-CdO NBs phase is able to selectively bind with Fe(III), implying that the mechanism of adsorption may be electrostatic attraction or a chelating mechanism. A schematic representation of Fe(III) ion adsorption on the doped ZnO-CdO NBs is presented in Figure 6.

Static Adsorption Capacity

For determination of the static uptake capacity of Fe(III) on doped ZnO-CdO NBs phase, 25.0 mL Fe(III) sample solutions with different concentrations (0~150.0 mgL^{-1}) were adjusted to pH 5.0 and individually mixed with 25.0 mg doped ZnO-CdO NBs. These mixtures were mechanically shaken for 1.0 hr at room temperature. Static adsorption capacity was obtained using equation (13) as follows:

$$q_e = \frac{(C_o - C_e)V}{m} \tag{13}$$

where q_e represents the adsorbed Fe(III) by the doped ZnO-CdO NBs phase (mgg^{-1}), C_o and C_e are the initial and equilibrium concentrations of Fe(III) ion in solution (mgL^{-1}), respectively, V is the volume (L) and m is the weight of doped ZnO-CdO NBs phase (g).

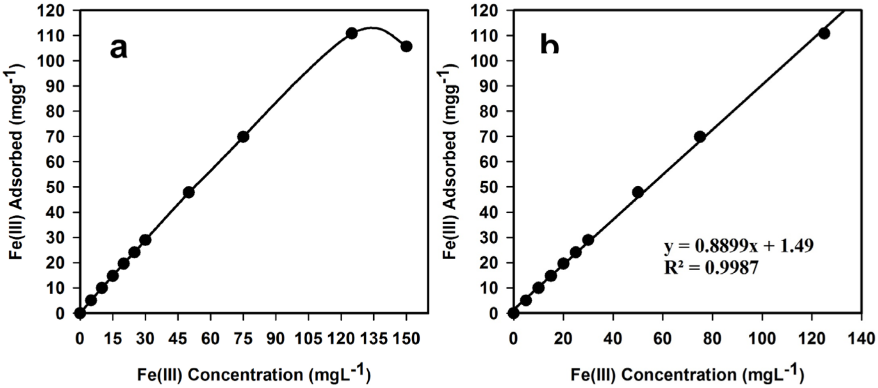

Figure 7. (a) Adsorption profile and (b) sensitivity of Fe(III) on 25.0 mg doped ZnO-CdO NBs phase in relation to the concentration at pH 5.0 and 25.0°C.

Figure 7a and Figure 7b shows the static adsorption capacity and sensitivity (~0.8899) of doped ZnO-CdO NBs for Fe(III) obtained from the experiment of adsorption isotherm. In this study, the adsorption capacity of doped ZnO-CdO NBs for Fe(III) was determined to be ~110.80 mgg^{-1}, which is comparable with those previously reported for Fe(III) in other studies 7.00 [53], 18.30 [54], 28.69 [55], 28.90 [56], and 173.14 [57] mgg^{-1}.

Adsorption Isotherm Models

Experimental equilibrium adsorption data were analyzed using different models in order to develop an equation that accurately represents the results. Langmuir equation is based on an assumption of a monolayer adsorption onto a completely homogeneous surface with a finite number of identical sites and a negligible interaction between the adsorbed molecules. The Langmuir adsorption isotherm model is governed by the following relation (14) [58]:

$$C_e/q_e = (C_e/Q_o) + 1/Q_o b \tag{14}$$

where C_e corresponds to the equilibrium concentrations of Fe(III) ion in solution ($mgmL^{-1}$) and q_e is the adsorbed metal ion by the adsorbate (mgg^{-1}). The symbols Q_o and b refer to Langmuir constants related to adsorption capacity (mgg^{-1}) and energy of adsorption (Lmg^{-1}), respectively. These constants can be determined from a linear plot of C_e/q_e against C_e with a slope and intercept equal to $1/Q_o$ and $1/Q_o b$, respectively. Moreover, the essential characteristics of Langmuir adsorption isotherm can be represented in terms of a dimensionless constant separation factor or equilibrium parameter, R_L, which is defined as $R_L = 1/(1 + bC_o)$, where b is the Langmuir constant (indicates the nature of adsorption and the shape of the isotherm); C_o the initial concentration of the analyte. The R_L value indicates the type of the isotherm, and R_L values between 0 and 1 represent a favorable adsorption [59-61].

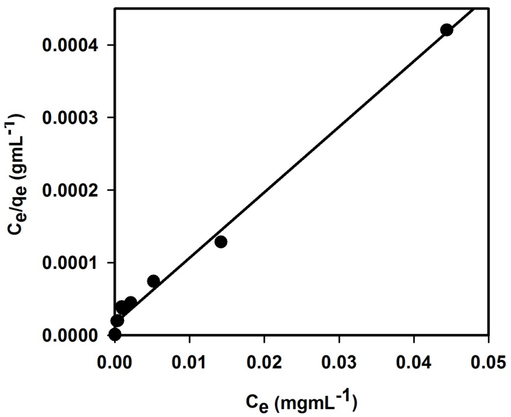

Figure 8. Langmuir adsorption isotherm model of Fe(III) adsorption on 25.0 mg doped ZnO-CdO NBs phase at pH 5.0 and 25.0°C. Adsorption experiments were obtained at different concentrations (0-150.0 mgL^{-1}) of Fe(III) under static conditions.

The experimental isotherm data were fit well with the Langmuir equation based on the least square fit, as shown in Figure 8, supporting the validity of Langmuir adsorption isotherm model for the adsorption process. Consequently, adsorption isotherm data indicated that the adsorption process was mainly monolayer on a homogeneous adsorbent surface. Langmuir constants Q_o and b are found to be ~110.72 mgg^{-1} and ~0.55 Lmg^{-1}, respectively. The correlation coefficient obtained from the Langmuir model is found to be $R^2 = 0.991$ for adsorption of Fe(III) on doped ZnO-CdO NBs. Furthermore, the static adsorption capacity (~110.72 mgg^{-1}) calculated from Langmuir equation was in agreement with that (~110.80 mgg^{-1}) of the experimental isotherm study. The R_L value of Fe(III) adsorption on the ZnO-CdO NBs is 0.01, indicating a highly favorable adsorption process based on the Langmuir classical adsorption isotherm model [62-64].

CONCLUSION

In this chapter, the present work offers a wet-chemically synthesize low-dimensional doped ZnO-CdO NBs, which was characterized using several conventional techniques like XRD, FE-SEM, XPS, XEDS, UV/visible, and FT-IR spectroscopy. The detailed morphological characterizations by XRD and FESEM displayed that the synthesized NBs possess almost block-shape with typical diameters of ~158.8 ± 10.0 nm. The optical properties of ZnO-CdO NBs were investigated by UV-visible absorption which shows the presence of characteristic NBs peak in the spectrum. It was also investigated the photo-catalytic degradation with BCB under solar-light sources and found the 52.3% degradation held with ZnO-CdO NBs. The efficiency of the newly prepared doped ZnO-CdO NBs phase for selective adsorption and determination of Fe(III) in aqueous solution is also investigated. Reasonable static adsorption capacity of ~110.80 mgg^{-1} with doped ZnO-CdO NBs adsorbent for Fe(III) in aqueous solution is executed. Adsorption data of Fe(III) were well fit with the Langmuir adsorption isotherm model. Thus, the method may play an important role for using it as an effective approach for a selective adsorption and determination of Fe(III) in complex matrices.

REFERENCES

[1] Wang F., D. Zhao, Z. Guo, L. Liu, Z. Zhang, D. Shen. *Nanoscale* 5 (2013) 2864-2869.
[2] Zheng Y., C. Chen, Y. Zhan, X. Lin, Q. Zheng, K. Wei, J. Zhu. *Journal of Physical Chemistry C* 112 (2008) 10773-10777.
[3] Faisal M., M. A. Tariq, M. Muneer. *Dyes. Pig*. 72 (2007) 233-239.
[4] Rahman M. M., M. A. Hasnat, I. A. Siddiquey, S. M. Islam. *International Journal of Scientific Research* 17 (2007) 69-74.
[5] Choi B. D., D. K. *Schroder Applied Physics Letter*. 79 (2001) 2645-2647.

[6] Rahman M. M., M. A. Hasnat, K. Sawada. *Journal of Scientific Research 1* (2008) 108-113.

[7] Saquib M., M. A. Tariq, M. Faisal, M. Muneer. *Desalination. Desalination* 219 (2008) 301-309.

[8] Blake D. M. (2001) Bibliography of work on the photocatalytic removal of hazardous compounds from water and air. *National Renewal Energy Laboratory*, USA. pp. 40-253.

[9] Mathews R. W., S. R. McEvoy. *Journal of Photochemical and Photobiology. A: Chemistry*. 64 (1992) 231-235.

[10] Rahman M. M., S. B. Khan, A. Jamal, M. Faisal, A. M. Asiri, K. A. Alamry, A. Khan, A. A. P. Khan, M. A. Rub, N. Azum, A. O. Al-Youbi. *Micro and Nanosystems*. 5 (2013) 3-13.

[11] Hristovski K. D., P. K. Westerhoff, T. Moller, P. Sylvester. *Chemical Engineering Journal* 146 (2009) 237-243.

[12] Jamal, M. M. Rahman, S. B. Khan, M. Faisal, A. M. Asiri, A. A. P. Khan, A. Khan, M. A. Rub, N. Azum. *Micro and Nanosystems* 5 (2013) 22-28.

[13] Faisal M., S. B. Khan, M. M. Rahman, A. Khan, M. Muneer, M. M. Abdullah. *Micro and nanosystems* 5 (2013) 38-46.

[14] Mohammadi S. Z., D. Afzali, D. Pourtalebi. *Central European Journal of Chemistry*. 8 (2010) 662-668.

[15] Cho H. J., S. W. Myung. *Bulletin of Korean Chemical Society* 32 (2011) 489-497.

[16] Xu H., Q. Zheng, P. Yang, J. Liu, L. Jin. *Chinese Journal of Chemistry* 29 (2011) 805-812.

[17] Tanikkul S., J. Jakmunee, S. Lapanantnoppakhun, M. Rayanakorn, P. Sooksamiti, R. E. Synovec, G. D. Christian, K. *Grudpan. Talanta* 64 (2004) 1241-1246.

[18] Pyrzynska K., *Spectrochimica Acta, Part B* 60 (2005) 1316-1322.

[19] Nasu, S. Yamaguchi, T. Sekine. *Analytical Science* 13 (1997) 903-911.

[20] Tao G. H., Z. Fang, *Journal of Analytical Chemistry* 360 (1998) 156-160.

[21] Soylak M., N. D. Erdogan. *Journal of Hazardous Materials* 137 (2006) 1035-1041.

[22] Manzoori J. L., H. Abdolmohammad-Zadeh, M. Amjadi. *Microchimica Acta* 159 (2007) 71-78.

[23] Fang G., J. Chen, J. Wang, J. He, S. Wang. *Journal of Chromatography A* 1217 (2010) 1567-1574.

[24] Ahmad R., R. Kumar. *Clean: Soil, Air, Water* 39 (2011) 74-82.

[25] Pei S., Z. Fang. *Analytica Chimica Acta* 294 (1994) 185-193.

[26] Rocha-de C. G., A. I. Luiz-de, R. P. dos-Santos. *Journal of Material Research* 7 (2004) 329-334.

[27] Wei K., L. Shu, W. Guo, Y. Wu, X. Zeng. *Chinese Journal of Chemistry* 29 (2011) 143-146.

[28] Liu Y., L. Guo, L. Zhu, X. Sun, J. Chen. *Chemical Engineering Journal* 158 (2010) 108-114.

[29] Marwani H. M., H. M. Albishri, T. A. Jalal and E. M. Soliman. *Desalination and Water Treatment* 45 (2012) 128-135.

[30] Marwani H. M., H. M. Albishri, E. M. Soliman and T. A. Jalal. *Journal of Dispersion Science and Technology* 33 (2012) 549–555.

[31] Tong S., S. Zhao, W. Zhou, R. Li, Q. Jia. *Microchimica Acta* 174 (2011) 257-264.

[32] Biparva P., M. R. Hadjmohammadi. *Clean: Soil, Air, Water* 39 (2011) 1081-1086.

[33] Li X., P. Sun, T. Yang, J. Zhao, Z. Wang, W. Wang, Y. Liu, G. Lu, Y. Du. *CrystEngComm* 15 (2013) 2949-2955.

[34] V. Galstyan, E. Comini, C. Baratto, A. Ponzoni, E. Bontempi, M. Brisotto, G. Faglia, G. Sberveglieri. *CrystEngComm*, 15 (2013) 2881-2887.

[35] Zou B. S., V. V. Volkov, Z. L. Wang. *Chemistry Materials* 11 (1999) 3037-3043.

[36] Peng Z. A., X. Peng. *Journal of American Chemical Society* 123 (2001) 183-184.

[37] Jung S. H., E. Oh, K. H. Lee, Y. Yang, C. G. Park, W. Park, S. H. Jeong. *Crystal Growth & Design* 8 (2008) 265-269.

[38] Rahman M. M., A. Jamal, S. B. Khan, M. Faisal. *ACS Applied Materials and Interfaces* 3 (2011) 1346-1351.

[39] Rahman M. M., S. B. Khan, M. Faisal, A. M. Asiri, M. A. Tariq. *Electrochimica Acta* 75 (2012) 164-170.

[40] Rahman M. M., A. Jamal, S. B. Khan, M. Faisal. A. M. Asiri. *Talanta* 95 (2012) 18-24.

[41] Rahman M. M., A. Jamal, S. B. Khan, M. Faisal. *Journal of Physical Chemistry C* 115 (2011) 9503–9510.

[42] Umar, M. M. Rahman, S. H. Kim, Y. B. Hahn. *Chemical Communication* (2008) 166-169.

[43] Rahman M. M., A. Jamal, S. B. Khan, M. Faisal. *Biosensors and Bioelectronics* 28 (2011) 127-134.

[44] Feng D., W. Luo, J. Zhang, M. Xu, R. Zhang, H. Wu, Y. Lv, A. M. Asiri, S. B. Khan, M. M. Rahman, G. Zheng, D. Zhao. *Journal of Materials Chemistry A* 1(2013)1591-1599.

[45] Rahman M. M., S. B. Khan, G. Gruner, M. S. Al-Ghamdi, M. A. Daous, A. M. Asiri. *Electrochimica Acta* 103 (2013) 143-150.

[46] Gulino, F. Castelli, P. Dapporto, P. Rossi, I. Fragalà. *Chemistry Materials* 14 (2002) 704-709.

[47] Rahman M. M., S. B. Khan, M. Faisal. M. A. Rub, A. O. Al-Youbi, A. M. Asiri. *Talanta* 99 (2012) 924-931.

[48] Park S., S. An, H. Ko, C. Jin, C. Lee. *ACS Applied Material and Interfaces* 4 (2012) 3650–3656.

[49] Subash B., B. Krishnakumar, M. Swaminathan, M. Shanthi. *Langmuir* 29 (2013) 939–949.

[50] Uddin M. T., Y. Nicolas, C. Olivier, T. Toupance, L. Servant, M. M. Müller, H. J. Kleebe, J. Ziegler, W. Jaegermann. *Inorganic Chemistry* 51 (2012) 7764-7773.

[51] Bae J., J. B. Han, X. M. Zhang, M. Wei, X. Duan, Y. Zhang, Z. L. Wang. *Journal of Physical Chemistry C* 113 (2009) 10379–10383.

[52] Han D. M., G. Z. Fang and X. P. Yan. *Journal of Chromatography A* 1100 (2005) 131-136.

[53] O'Connell D. W., C. Birkinshaw, T. F. O'Dwyer. *Bioresource Technology* 99 (2008) 6709-6724.

[54] Tokalioglu S., V. Yilmaz, S. Kartal, A. Delibas and C. Soykan, *Journal of Hazardous Materials* 169 (2009) 593–598.

[55] Zang Z., Z. Hu, Z. Li, Q. He, X. Chang. *Journal of Hazardous Materials* 172 (2009) 958-963.

[56] Li Z., X. Chang, X. Zou, X. Zhu, R. Nie, Z. Hu, R. Li. *Analytica Chimica Acta* 632 (2009) 272-277.

[57] Ghimire K. N., J. Inoue, K. Inoue, H. Kawakita, K. Ohto. *Separation Science and Technology* 43 (2008) 362-375.

[58] Langmuir. *Journal of American Chemical Society* 38 (1916) 2221-2295.

[59] Mckay G., H. S. Blair, J. R. Gardener. *Journal of Applied Polymer Science* 27 (1982) 3043-3057.

[60] Rahman M. M., S. B. Khan, H. M. Marwani, A. M. Asiri, K. A. Alamry, M. A. Rub, A. Khan, A. A. P. Khan, A. H. Qusti. *Journal of Industrial and Engineering Chemistry* 20 (2014) 1071-1078.

[61] Rahman M. M., S. B. Khan, A. M. Asiri, K. A. Alamry, A. A. P. Khan, A. Khan, M. A. Rub. *Microchimica Acta*. 180 (2013) 675-685.

[62] Rahman M. M., S. B. Khan, H. M. Marwani, A. M. Asiri, K. A. Alamry, A. O. Al-Youbi. *Talanta* 104 (2013) 75-82.

[63] Qian X., D. Xiong, A. M. Asiri, S. B. Khan, M. M. Rahman, H. Xu, D. Zhao. *Journal of Materials Chemistry A* 1 (2013) 7525-7532.

[64] Rahman M. M., S. B. Khan, A. M. Asiri, H. M. Marwani, A. H. Qusti. *Composites B Part: Engineering.* 54 (2013) 215-223.

In: Fundamentals of Photocatalysis ISBN: 978-1-68507-374-9
Editor: Orva Auger

Chapter 4

HETEROGENEOUS PHOTOCATALYSIS EXPLAINED THROUGH THE USE OF TITANIUM AND TUNGSTEN OXIDE NANOSTRUCTURES

L. Soares*[*] *and A. Alves
Department of Materials Engineering,
Federal University of Rio Grande do Sul, Porto Alegre, Brazil

ABSTRACT

Heterogeneous photocatalysis is well-known as an advanced oxidative process (POA's) due to its multiple applications, such as air purification, antibacterials, green energy, self-cleaning, water treatment and CO_2 reduction. Photocatalytic processes gained notoriety in 1972, with an innovative study by Fujishima and Honda. His work boosted the use of TiO_2 in photocatalytic processes. However, the wide bandgap (± 3.2 eV) of TiO_2 causes low efficiency to separate the charges and presents a low absorption capacity under solar irradiation. Doping or combining

---

[*] Corresponding Author's E-mail: lugoes.soares@gmail.com.

TiO_2 with metals or non-metals appears as an option to improve its photocatalytic performance as a semiconductor. The presence of the dopant adjusts the bandgap and the behaviour of the electron/hole pair what contributes to the better photocatalytic performance of TiO_2 when irradiated with sunlight in the UV-visible region. WO_3 is a transition metal widely used as a semiconductor and as a dopant due to its smaller bandgap, between 2.6-2.8 eV, which increases the radiation absorption capacity of this oxide in the visible region.

Keywords: heterogeneous photocatalysis, bandgap, doping

INTRODUCTION

Photocatalytic processes gained notoriety in 1972, with an innovative study by Fujishima and Honda (1972). His work boosted the use of TiO_2 in photocatalytic processes, Wu et al., (2018).

Among the Advanced Oxidative Processes (POA's), heterogeneous photocatalysis is the most efficient to degrade pollutants, as it does not generate harmful intermediates to the environment. When light hits the semiconductor, it absorbs photons, with energy greater than or equal to the bandgap energy, causing the electron to be promoted from the valence band (VB) to the conduction band (CB), thus generating the electron/hole pair (e/h+), Basavarajappa et al., (2020).

These photogenerated species react with oxygen molecules or hydroxyl groups to produce reactive oxygen species such as hydroxyl radicals (OH) and superoxide anion radicals (O_2-). These species can interact with organic molecules, dissociating them by oxidation. In this way, the electron (and reducing agent)/hole (h^+ oxidizing agent) pair is formed on the surface of these photoactivated semiconductors, Ibrahim et al., (2020).

TiO_2 is the most used semiconductor in heterogeneous photocatalysis, as it has properties such as photostability, high efficiency for the degradation of organic compounds and low cost. These presented characteristics favour its wide application in photocatalytic processes. As a disadvantage, TiO_2 has a high bandgap value, limiting its activation when exposed to visible light (Ibrahim et al., 2020).

Doping and combining TiO_2 with transition metals adjust the bandgap and charge behaviour of the electron/hole pair. The presence of dopants such as vanadium, manganese, silver, tungsten, niobium, zirconium, among others, in the TiO_2 crystal lattice, in addition to decreasing the possibility of recombination of the electron/hole pair, and increasing the speed of the oxidation/reduction reaction, also increases the TiO_2 absorption range when exposed to visible light, Wu et al., (2018).

Several techniques are used for TiO_2 doping, such as direct hydrolysis of inorganic/organic salts, sputtering, ion implantation, ball milling, sol-gel, hydrothermal, solvothermal, electrospinning, spin-coating, among others, Basavarajappa et al., (2020).

Mourão and Mendonça (2009) addressed in their study the main synthesis methods used to obtain nanostructures with photocatalytic capacity. They reported the main ways to carry out the photodegradation of organic molecules. They were focusing on nanoscale photocatalyst synthesis methods. Finally, they described several examples of semiconductor synthesis in the form of immobilized nanoparticles and thin films.

Hunge et al., (2017) report the photocatalytic performance of layered WO_3 and WO_3/TiO_2 thin films, successfully prepared by the spray pyrolysis method. The photoelectrocatalytic activity is more remarkable when using the stratified WO_3/TiO_2 sample than the WO_3 thin-film photoelectrode in oxalic acid degradation. The WO_3/TiO_2 sample can remove 83% of the oxalic acid after 180 minutes of exposure. The photoelectrocatalytic experimental results indicate that the WO_3/TiO_2 stratified photoelectrode is a promising material for removing pollutants from water.

Ge et al. (2017) present a review, reporting the most recent developments in the fabrication of different TiO_2 nanostructures, aiming to increase light absorption in the visible region and decrease the chance of electron/hole pair recombination. The described nanostructures are promising for the most diverse applications, ranging from semiconductors in photocatalytic processes, such as hydrogen production and pollutant degradation, to photoelectric processes.

This work reports the synthesis and photoactivity of TiO_2 and TiO_2 nanostructures containing tungsten precursors (H_2WO_4 and $Na_2WO_4.2H_2O$) obtained by spin-coating. These samples were used as semiconductors in heterogeneous photocatalysis, and their photocatalytic capacity was evaluated.

LITERATURE REVIEW

Photocatalysis

Among the techniques currently available, advanced oxidative processes (AOP's) are the most effective technology in removing organic pollutants from wastewater. In heterogeneous photocatalysis, a semiconductor is activated when exposed to solar or artificial radiation. It has a high degradation power due to the action of its redox reactions, Hunge (2017).

Several semiconductor materials are used in heterogeneous photocatalysis, such as TiO_2, WO_3, Bi_2WO_6, ZnO, Bi_2O_3, CdS, among others. TiO_2 is the most used semiconductor due to its low cost, good stability, and being ecologically correct. The main drawback found when using it is that TiO_2 has a high bandgap (3.2 eV). What causes a low absorption capacity, about only 4% of photons in the solar spectrum. Aiming to increase the absorption capacity of TiO_2, many researchers have been developing different combinations between semiconductors photocatalysts obtained by different methods; some examples include TiO_2/SnO_2, TiO_2/ZnO, TiO_2/CdS and TiO_2/WO_3. Among these, samples containing WO_3/TiO_2 is a promising route due to the presence of a more significant number of Lewis and Bronsted acid sites (W^{6+} species), which generate a high amount of hydroxyl (OH) radicals, necessary for the mineralization of organic impurities, Hunge (2017).

Titanium Dioxide (TiO_2)

In photocatalytic processes, the most active semiconductor is TiO_2. It is an n-type, indirect gap photocatalyst and is generally used in the degradation of organic compounds. The fact that it has a wide bandgap (3.2 eV) restricts its absorption capacity in the visible spectrum, in addition to causing rapid recombination between charge carriers and low interfacial charge transfer rates, which makes its most significant application, Nagaraj et al., (2019).

TiO_2 exists under three different crystal structures: anatase, brookite and rutile. These three phases are described in terms of the Ti atom, surrounded by six oxygen atoms. Despite the similarities in the Ti-O_6 octahedral arrangement for these three allotropic forms, their electronic structures are different Nagaraj et al., (2019).

Among the crystalline phases mentioned, the anatase form has the highest photoactivity. On a nanometric scale, it is considered the most favourable phase for converting solar energy and application in photocatalysis, Nagaraj et al., (2019).

Preparation of pure TiO_2 nanoparticles by different methods are well reported; some options include: hydrothermal, sol-gel, chemical vapour deposition, microemulsion, electrospinning, spray deposition and aerosol-assisted chemical vapour deposition. However, most of the methods mentioned above are expensive or complicated. As a result, researchers are committed to formulating more straightforward and more economically viable methods.

Doping with other metal oxides is a good alternative, which aims to increase the visible light absorption capacity of TiO_2, Nagaraj et al., (2019).

Tungsten Trioxide (WO_3)

Tungsten trioxide is one of the most promising metal oxides, and for this reason, it is widely studied. It has high thermal and chemical stability in acidic and neutral environments, Hromadko et al., 2021. It is presented under the phases: monoclinic (γ-WO_3) at room temperature up to ~ 330ºC (space group $P2_1/n$), orthorhombic (β-WO_3, 330–740°C, $P2/_m$) and tetragonal (α-WO_3, ≥740°C, P4/NCC), Hromadko et al., (2021).

It is an n-type semiconductor with a bandgap ranging between (2.4–2.8 eV). Its advantage is that it can be activated under visible light illumination (by wavelengths ≤450 nm), Hromadko et al., (2021).

Regardless of the application, it is preferable to use WO_3 in the nanostructured form, since in this way, a large surface area and a high surface/volume ratio are obtained. Other advantages include efficient charge separation and increased light absorption, Hromadko et al., (2021).

The main techniques used to obtain these nanostructures mention the sol-gel routes Kantha et al., (2020), spray pyrolysis Hunge (2017), hydrothermal Farjood and Zanjanchi (2019), electrospinning Soares et al., (2021), WO_3 anodization Barczuk et al., (2006) and centrifugal spinning Rihova et al., (2021) among others.

Sodium Tungstate Dihydrate ($Na_2WO_4.2H_2O$)

Sodium tungstate dihydrate is a commercially available salt in the form of a white crystalline powder, soluble in water, often used as a source of tungsten, with a molecular weight of 329.85 g/mol, the density of 3.23 at (20°C), has a melting point at 100°C, and is a relatively strong oxidizing agent. Sodium tungstate dihydrate synthesizes inorganic compounds, polyoxometalates, and as a catalyst or catalyst precursor in various organic reactions. It can oxidize several substrates in the presence of hydrogen peroxide, obtaining only water as a by-product. On the other hand, the association of this reagent with other inorganic reagents, such as polyoxometalates, provides the generation of several complexes, mainly peroxocomplexes, Duarte (2013).

Its application includes epoxidation, cleavage of double bonds (carboxylic acids, aldehydes or ketones), oxidation of alcohols, oxidation of amines (primary amines to hydroxylamines and nitro derivatives and secondary amines nitrones), oxidation of imines, oxidation of organosulfur compounds, halogenation of aromatic compounds, synthesis of β–aryl vinyl bromides and in the synthesis of substitution 5 by 1 -H- tetrazoles, Duarte (2013).

Substrates

Most studies using photocalyzers occur in suspension (films) or under total mixture (fibers). Applied under complete mixing, it has advantages such as; a greater surface area. However, the fact that it is impossible to recover the photocatalyst causes an increase in operating costs, associated with loss of mass and separation of the catalyst, which has encouraged the use of photocatalysts in immobilized form. What enables its recovery and subsequent reuse, Oshani et al., (2014).

The substrates used in immobilization need to have high porosity and adsorption capacity to increase surface area, greater thermal stability during crystalline phase changes, and a reduction in photocatalyst density, allowing more significant photocatalyst/pollutant interaction, Feltrin et al., (2014).

Although several other parameters influence the effectiveness of immobilization, substrate roughness and suspension properties are undoubtedly the most significant, Feltrin et al., (2014).

Within this context, several materials have been tested to function as a substrate, including granular activated carbon, stainless steel, quartz, ceramic materials, zeolites, polymers, glass, among others, Oshani et al., (2014).

In the case of using glass as a substrate, the photocatalytic properties of the films will depend mainly on the method used in the synthesis of the samples. Both thin and thick films can be obtained. The greater the thickness, the greater the number of crystals, the greater the number of electron/hole pairs, making photocatalysis more efficient. Therefore, for the success of the photocatalytic reaction, it is essential to analyze the composition of the substrate and its interaction with the material placed on it, as these influence the formed phase and the efficiency of the process, Oshani et al., (2014).

Electrospinning

Semiconductors for application in photocatalysis can be prepared by various techniques, including colloidal chemistry, organometallic route, Silva et al., 2010, sol-gel, hydrothermal route, electrospinning, Pechini method or polymeric precursor method, among others, Kantha et al., (2020).

Most of the works published in the last ten years report the electrospinning or electrospinning method as the primary technique for obtaining fibers/nanofibers from different materials, Yang (2013). It is generally chosen to synthesize TiO_2 nanofibers due to its ease of implementation, rapid formation of fibers and fabrics, non-woven fibers, continuously, with diameters ranging from 0.01 to 10 μm, for various materials, from biopolymers to ceramics, Rutledge and Fridrikh (2007).

For the continuous production of fibers, five components are needed: infusion pump, a syringe filled with the polymer solution, capillary (needle), a high voltage source and a collector, Rutledge and Fridrikh (2007).

The nanofiber fibers are generated due to the high voltage applied to a capillary containing the polymer solution. When electrostatic forces overcome the surface tension of the polymeric liquid, a drop of polymeric solution is ejected towards the collector, Rutledge and Fridrikh (2007).

Spin-Coating

Several methods have been used to deposition thin films on ceramic substrates, such as cathodic anodizing, chemical vapour deposition, magnetron sputtering, dip coating, and spin coating. The most used application techniques for thick films are flat screen printing, airbrushing, iconography, and digital printing. The latter is associated with heat treatment, Feltrin et al., (2014).

Spin-coating is a technique used to deposition thin films in the protection of metals, polymers, electrical circuits, integrated optical systems, and Bolsoni (2011). It is based on the deposition of drops of the initial precursor solution on the surface of a substrate, which is subjected to rotational movements, generating speed in relation to the substrate and draining the liquid towards its ends, Guaraldo (2014). The substrate rotates around an axis, which must be perpendicular to the overlay region. Subsequently, the liquid reaches the end of the substrate and is removed in the form of droplets. The removal rate of excess liquid decreases, the viscosity increases, and the concentration of non-volatile particles increases. Finally, the solvent evaporation process ends, resulting in the formation of films, Feltrin et al., (2014).

MATERIALS AND METHODS

Sample Construction

Electrospinning

Fiber synthesis occurs through the electrospinning technique, which consists, firstly, in the preparation of precursor solutions containing the necessary reagents to form fibers. The TiO_2 solution contained 2.5 ml of titanium tetraisopropoxide (TTIP), 2.0 ml of glacial acetic acid and 5 ml of an alcoholic solution containing 10% by weight of polyvinylpyrrolidone (PVP). The TiO_2/WO_3 solution contained the reagents of the TiO_2 solution plus 1 mL of hydrogen peroxide and 0.10 g of H_2WO_4, which were kept under magnetic stirring for 15 minutes. Finally, the $TiO_2/Na_2WO_4.2H_2O$ solution contained the same reagents as the TiO_2 solution, plus 1 mL of hydrogen peroxide and 0.10 g of $Na_2WO_4.2H_2O$, which remained under magnetic stirring for 15 minutes. Once the preparation has been completed, a plastic syringe is loaded with 5 ml of each precursor solution. Then, a 1 mm diameter stainless steel hypodermic (capillary) needle is connected to the high voltage source. The rotating cylindrical collector, where the fibers are deposited, is covered with a sheet of aluminium foil and is 12 cm from the capillary tip. A voltage of 13.5 kV is used between the capillary and the collector. The flow control of each precursor solution (1.8 mL/h) is performed by an infusion pump (KD Scientific). Fibers were collected every 30 minutes for 4 hours for each formulation. After fiber synthesis, an electric oven (Sanchis) is used to perform the heat treatment of the samples. The temperatures ranged between 650°C and 800°C, with a 1 hour plateau and a heating rate of 1.4°C/min.

Obtaining the Films by Spin-Coating

To obtain the films, 13 solutions were first prepared, which would be deposited on the glass plates. These solutions contained: 0.25 g of TiO_2-P25 standard (commercial Evonik-powder) or fibers of each formulation, heat-treated at 650°C, 700°C, 750°C and 800°C, mixed with 8 mL of anhydrous ethanol and 0.8 ml of acetylacetone (Sigma-Aldrich). The mixtures were dispersed in ultrasound for 10 minutes. After this period, 0.1 mL of Triton X-100 (Sigma-Aldrich) and 0.4 g of polyvinyl butyral (PVB) were added, which were kept under magnetic stirring for 10 minutes.

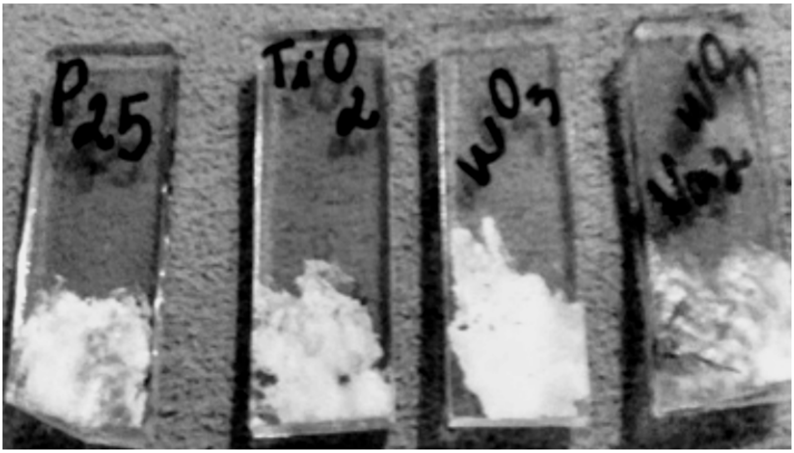

Figure 1. Photographic image of the films obtained by spin-coating.

The films were obtained by depositing 5 drops of each solution prepared above on glass plates (1 cm x 2 cm) covered with FTO (Fluorine-Doped Tin Oxide, XOP Glass). These glass plates were fixed with double-sided tape in the appropriate place on the equipment to start the spin-coating process. The equipment used was a (TC 100 Spin Coater) with a rotation of 800 RPM for 30 s. Figure 1 is a photographic image of the films obtained by spin-coating.

Characterization of Nanostructures

The X-ray diffraction (XRD) technique was used to determine the crystalline phases formed. Measurements were performed by a PHILIPS diffractometer, with CuKα radiation, using a voltage of 40 kV and 40 mA, with a speed of 0.05°/min and a step of 1 s, in a range of 5 to 75°. The obtained diffractograms were compared to the JCPDS database (Joint Committee on Powder Diffraction Standards) using the X'Pert HightScore® software, which comes with the equipment, which helped in the determination of the phases present in the samples. The microstructure of the samples was performed in a scanning electron microscope (SEM, JEOL JSM 6060), equipped with EDS (Energy Dispersive Spectroscopy), used to aid and identify Na, W, Ti and O atoms present in the films, depending on the composition of the samples. A UV–vis-NIR (Cary 5000) double-beam spectrophotometer was used to determine the bandgap of the samples using the Kubelka-Munk correlation. Films photoactivity was analyzed using a spectrophotometer (Cary Agilent 7000) with the UMA accessory, Soares and Alves (2018).

Photocatalytic Measurements

The photoactivity of all samples was determined based on monitoring the discoloration of the methyl orange dye over time in the presence of the synthesized films.

Before starting the photocatalytic tests, adsorption tests were carried out only with the substrate. The substrate was submerged in 125 ml of a 20 ppm solution of the methyl orange dye and left in the dark for 15,30, 45, 60, 75, 90, 105, 120 and 135 minutes. After each period, the liquid was analyzed by a spectrophotometer (Cary 5000, Agilent, with UMA accessory).

The photocatalysis process was carried out in a photocatalytic reactor, made of pyrex glass, where 12 black UV-A lamps provided radiation, 8 W each, model Flúor BLB T5 and branded Sadokin. The lamps are arranged in two semi-cylinders, which have a reflecting internal surface. The other components of the photocatalytic reactor comprised a magnetic stirrer, a compressed air aeration system and a thermostatic bath.

Samples were removed from the reactor flask through a channel closed by a silicone septum. The water circulation was carried out constantly through the outer part of the flask, making it possible to keep the test temperature fixed at 30°C. The bottle also has a cap with an extension with a porous tip to bubble compressed air into the liquid. To carry out the photocatalysis tests, 125 ml of a solution containing 20 ppm of methyl orange were used, transferred to a photocatalytic reactor, and the UV light system was turned on. Next, the TiO_2, TiO_2/WO_3 and $TiO_2/Na_2WO_4.2H_2O$ film was immobilized inside the reactor, one at a time. Before the beginning of each test, a 4 mL aliquot of the solution was collected, defined as the initial reference sample (absorbance indicative of a concentration equal to 100% methyl orange; reaction time of zero minutes). This first aliquot was removed before applying the light system, circulating water and bubbling air.

After the beginning of each assay, 4 mL aliquots were removed with a syringe at 15-minute intervals, filtered through a 0.2 μm filter, and transferred to polymethylmethacrylate (PMMA) buckets. Then, the aliquots were analyzed by a spectrophotometer (Cary 5000, Agilent, with UMA accessory).

RESULTS AND DISCUSSION

Descriptive of the Phases Present in the Samples

The samples containing the fibers without heat treatment (WHT) were amorphous, regardless of their composition, as shown in Figure 2.

TiO_2 samples (Figure 3) treated up to 700°C showed only the presence of the anatase crystalline phase (JCPDS 01-078-2486). Its first characteristic peak appeared at approximately $2\vartheta = 25.325°$. For samples treated from 750°C, in addition to the anatase phase, the rutile phase formation was identified (JCPDS 01-077-0442). The first characteristic peak of the rutile phase appears at approximately $2\vartheta = 27.425°$. Result of the occurrence of a transition from the anatase crystalline phase to the rutile phase. The latter, which arises after increasing the temperature of the heat treatment. However, the temperature at which this phase transition occurs depends on factors such as impurities or additives, a technique used in sample synthesis, and others, Feltrin et al., (2009).

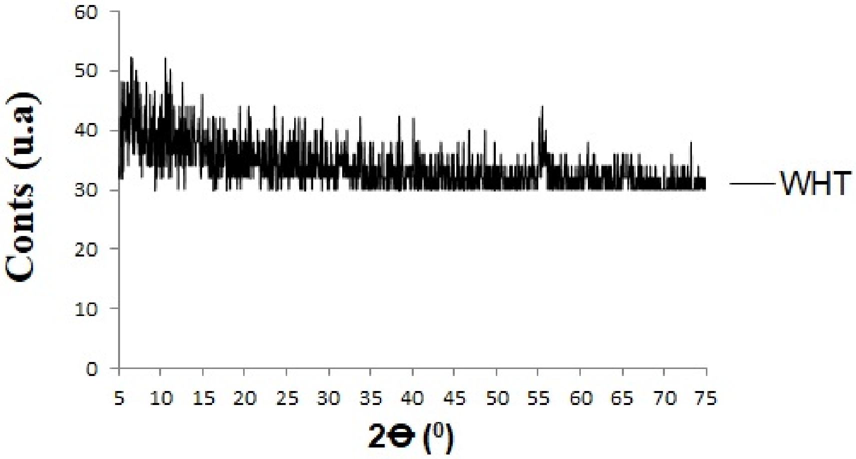

Figure 2. Diffractogram of samples without heat treatment.

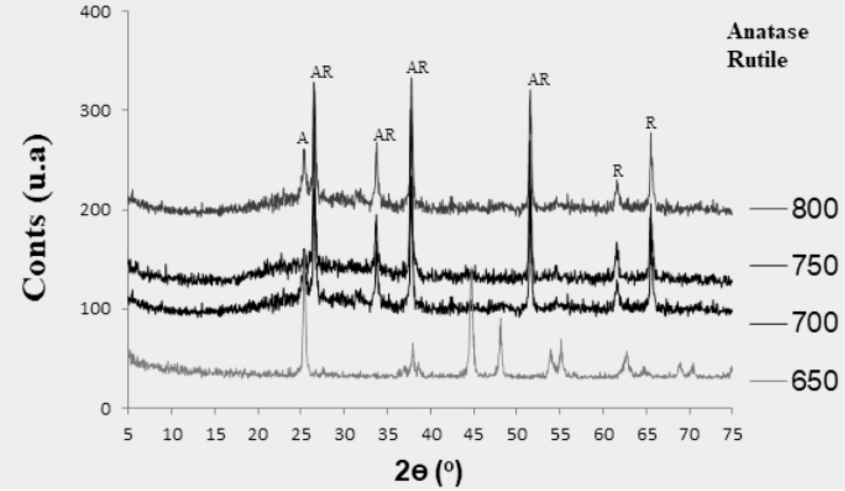

Figure 3. Diffractogram of TiO_2 samples.

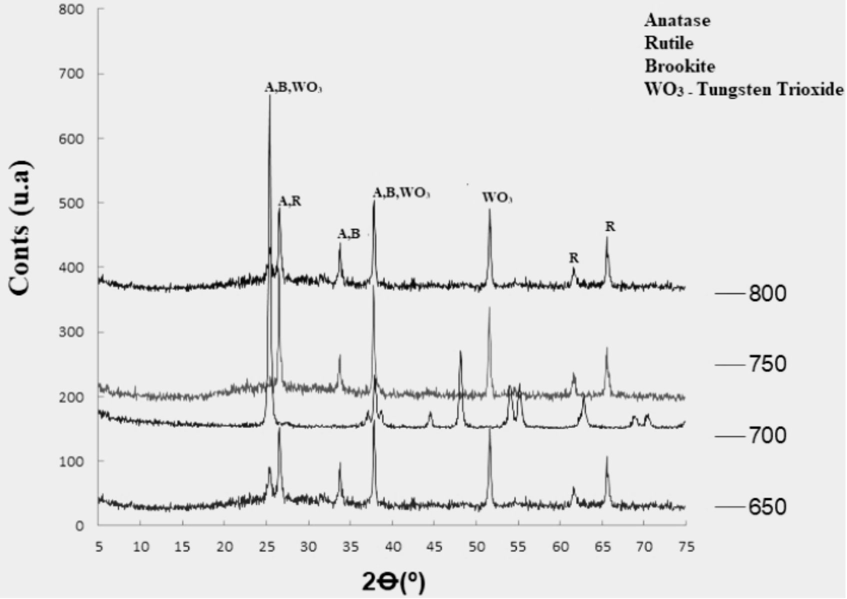

Figure 4. Diffractogram of TiO_2/WO_3 samples.

Until to the temperature of 650°C, for the TiO_2/WO_3 samples (Figure 4), the anatase (JCPDS 01-078-2486) and brookite (JCPDS 01-075-1582) phases were identified, with characteristic peaks at $2\vartheta = 25.271°$ and 25.425°, respectively. The heat treatment from 700°C was identified for TiO_2 and the anatase and brookite phases and the rutile phase (JCPDS 01-077-0442), the latter with the first characteristic peak at $2\vartheta = 27.425°$. For WO_3, the monoclinic phase (JCPDS 00-032-1393) was detected, with the first characteristic peak at approximately $2\vartheta = 23°$, at all heat treatment temperatures, between 650°C and 800°C.

For the samples of $TiO_2/Na_2WO_4.2H_2O$ (Figure 5) treated up to a temperature of 700°C, the anatase (JCPDS 01-078-2486) and brookite (JCPDS 01-075-1582) phases were identified for TiO_2 and the monoclinic phase for WO_3 (JCPDS 00-032-1393). For samples submitted to heat treatment at 750°C, the same phases already mentioned for TiO_2 were identified, and the tetragonal phase (JCPDS 00-002-0414) for WO_3, with the first peek at $2\vartheta = 15.604°$. For the samples treated at a temperature of 800 °C, in addition to the anatase and brookite phases, the rutile phase (JCPDS 01-077-0442) was also identified for TiO_2 and the tetragonal phase for WO_3. For the Na(OH) group, the orthorhombic phase (JCPDS 00-035-1009) was detected, which appeared in all samples, independent of the heat treatment temperature. The first characteristic peak appeared at approximately $2\vartheta = 16°$.

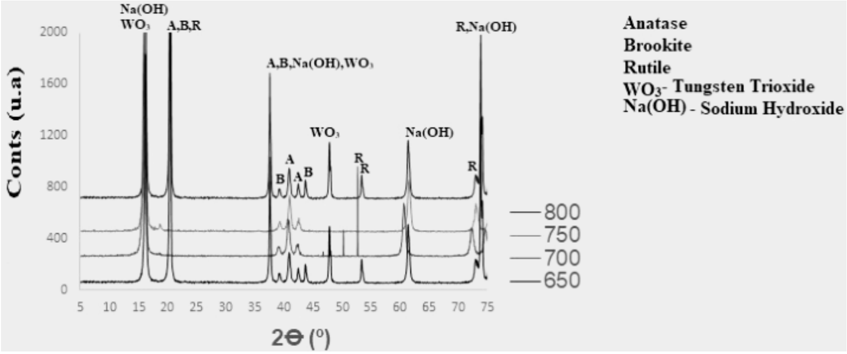

Figure 5. Diffractogram of $TiO_2/Na_2WO_4.2H_2O$ samples.

Microstructure in the Samples

Figure 6 a-c shows scanning electron microscopy (SEM) images of the surface of TiO_2, TiO_2/WO_3 and $TiO_2/Na_2WO_4.2H_2O$ films. Overall, these samples appeared to have an elongated, continuous and misaligned nanostructure. The agglomerate observed in the $TiO_2/Na_2WO_4.2H_2O$ samples (Figure 6c) is due to the presence of several interconnected grains, confirmed by the transmission electron microscopy (TEM) image in Figure 7. Energy dispersive spectroscopy (EDS) proved the existence of Na, W, Ti and O atoms, depending on the composition of the samples.

Figures 8, 9 and 10 show the photocatalytic activity of TiO_2, TiO_2/WO_3 and $TiO_2/Na_2WO_4.2H_2O$ films in the degradation of methyl orange dye during 135 minutes of exposure to UVA light ($\lambda = 365$ nm). All samples showed photocatalytic activity. For TiO_2 films, the most photoactive were those that received heat treatment at 650ºC; they managed to degrade approximately 25% of the methyl orange dye in 135 minutes of UVA irradiation. The TiO_2-800ºC films and the P25 standard had similar behaviour, degrading approximately 12% and 14%, respectively, of the dye in 135 minutes of UVA irradiation. TiO_2-700ºC and 750ºC films degraded approximately 19% and 20%, respectively, of the dye in 135 minutes of UVA irradiation. The decrease in degradation effectiveness observed when the heat treatment temperature increases is a trend due to the appearance of the rutile phase, which, in the case of films, is formed from treatments above 700°C. The rutile phase has a lower photocatalytic activity than the anatase phase, and, for this reason, its appearance results in a decrease in degradative capacity, Feltrin et al., (2009).

The presence of tungstic acid (H_2WO_4) in the TiO_2/WO_3 films increased the degradation capacity of these samples. TiO_2/WO_3 films - 650°C, 700°C, 750°C and 800°C degraded approximately 38%, 44%, 60% and 98% of the dye, respectively. It stands out that the TiO_2/WO_3 – 800ºC sample was the most effective and fast in dye degradation since, in just 90 minutes of exposure to UV-A light, it discolored 97% of the dye. This increase in degradation capacity is due to the association between bandgap reduction from 3.05 eV to 2.89 eV, inhibition of electron/hole pair recombination [(e^-)/(h^+)], which allows the transfer of loads between TiO_2 and WO_3, and the increase in the formation of point defects (O_2 vacancies). Charge transfer is favored by the presence of the hydroxyl group (OH) on the surface of the films, which facilitates the separation of photogenerated electrons/holes. TiO_2 has higher positive potentials than the valence and conduction band of WO_3. Thus, the conduction band (CB) of WO_3 can act as an electron collector and can pull the CB electrons (e^-) generated in the CB of TiO_2 to its own CB, at the same time, the valence band (VB) of TiO_2 acts like an orifice collector (h^+), therefore, photogenerated orifices are transferred from the VB of WO_3 to the VB of TiO_2 and, the e^-/h^+ pairs increase the degradation capacity and the efficiency of the process, Hunge (2017).

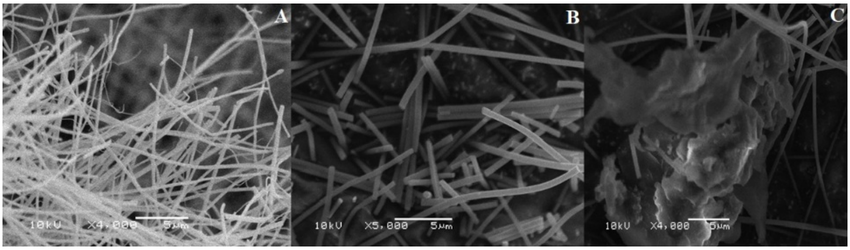

Figure 6. Scanning electron micrograph of (a) TiO_2, (b) TiO_2/WO_3 and (c) $TiO_2/Na_2WO_4.2H_2O$ films.

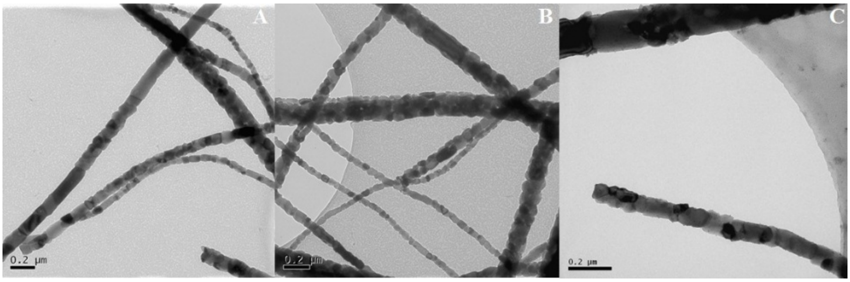

Figure 7. Transmission electron micrograph of (a) TiO_2, (b) TiO_2/WO_3 and (c) $TiO_2/Na_2WO_4.2H_2O$ films.

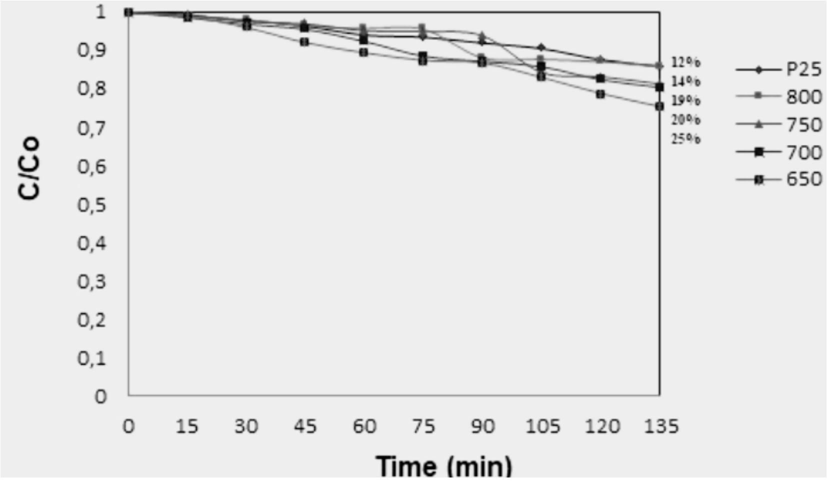

Figure 8. Degradation of methyl orange dye in TiO_2 thin film under UV-A illumination.

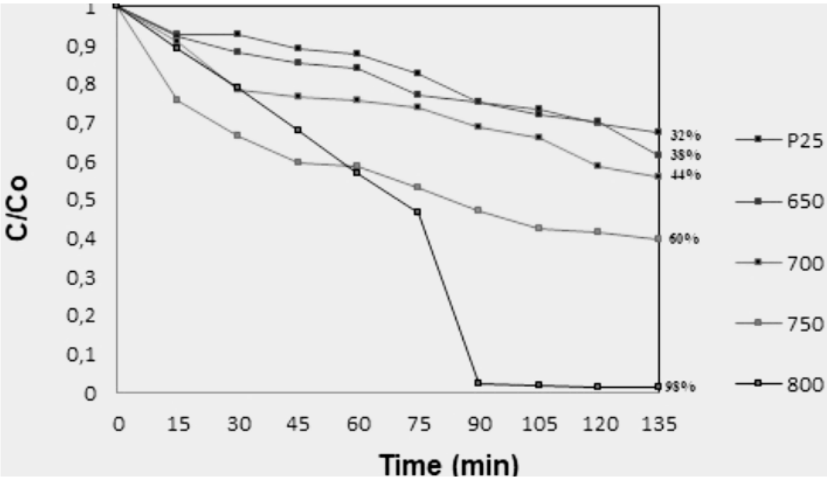

Figure 9. Degradation of methyl orange dye in TiO_2/WO_3 thin film under UV-A illumination.

The most effective samples in the degradation of the methyl orange dye were $TiO_2/Na_2WO_4.2H_2O$ - 800°C films, which discolored 99% of the methyl orange dye. Note that within 120 minutes of exposure to UV-A light, these samples had already degraded 87% of the methyl orange dye.

The other films, heat-treated at 650°C, 700°C and 800°C, degraded 52%, 84% and 88%, respectively, of the methyl orange dye. All samples had their degradation capacity increased with the precursor of sodium tungstate dihydrate ($Na_2WO_4.2H_2O$) compared with the photoactivity of the TiO_2 and TiO_2/WO_3 samples, respectively. The high temperature caused an increase in the kinetic energy of the molecules, which reacted quickly, increasing the reaction speed. This generated many vacancies of O_2 and hydroxyl radicals (OH) that quickly adsorbed on the surface of the sample, Hunge (2017). O_2 vacancies are punctual defects that occupy positions in the atomic lattice and are strongly linked to application in photocatalysis. The increase in the number of O_2 vacancies provided stability of the structural phase of TiO_2, responsible for the increase in the conductivity of the oxygen ion. The presence of O_2 vacancies drastically reduces the chance of recombination of the electron/hole pair. The high temperature of the heat treatment allowed the O_2 vacancies to acquire the necessary mobility to move to a disordered state in the anionic sub-network, Muccillo (2008). A study by Chen et al., (2018) described the better performance of black TiO_2 nanoparticles than TiO_2 nanoparticles due to O_2 vacancies.

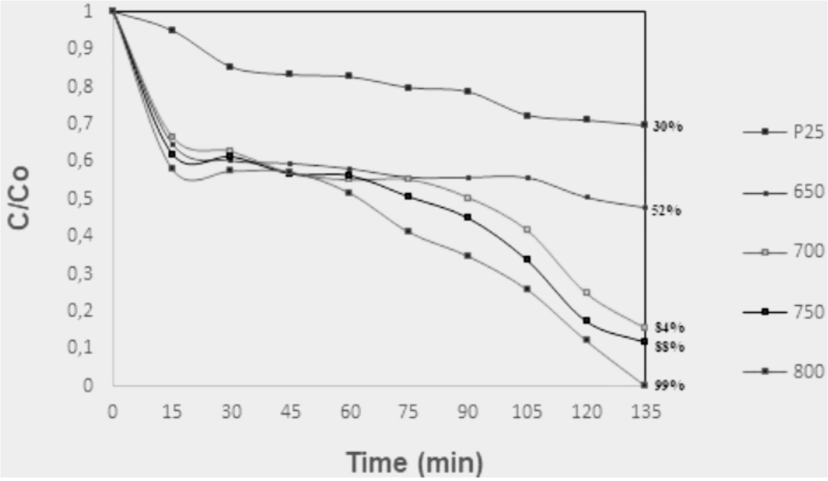

Figure 10. Degradation of methyl orange dye in $TiO_2/Na_2WO_4.2H_2O$ thin film under UV-A illumination.

APPLICATIONS

Heterogeneous photocatalysis can be used for many different purposes. It is a well-established technique and has been widely used in the degradation of organic contaminants present in wastewater, removal of color in industrial effluents, sewage disinfection, among others. Below we report some recent works highlighting various applications using heterogeneous photocatalysis, Hunge et al., (2017).

Bharti et al., (2016) produced TiO_2 films doped with different metals and observed that the best results were obtained with the Fe-doped TiO_2 thin film due to the increase in the number of O_2 vacancies associated with the reduction of the gap of the samples. They concluded that the joint action of these two factors produces transparent TiO_2 thin films with good optical properties, making them promising candidates for application as electrodes.

Hunge (2017) reports a promising study for application in water treatment. In their report, thin-layered films of WO_3/TiO_2 were prepared by spray pyrolysis. The best result was achieved using the stratified WO_3/TiO_2 photoelectrode. This sample degraded 66% of the benzoic acid after 320 minutes under sunlight. The result achieved was attributed to the presence of Lewis and Bronsted acid sites (W^{6+} species) that adsorb a more significant amount of OH or H_2O, therefore, considered necessary for the generation of OH radicals and mineralization of organic impurities.

Soares et al., (2021) describe the use of fibers containing titanium and tungsten oxides for the generation of hydrogen through the water-splitting technique. The most efficient samples in hydrogen generation were $TiO_2/Na_2WO_4.2H_2O$ - 800°C fibers. The authors attributed this result to the formation of a more significant number of O_2 vacancies due to the increase in temperature and the bandgap reduction. This allowed a more significant charge transfer between the two semiconductors, which reduced the chance of recombination of the electron-hole pair, which increased the photocatalytic efficiency in hydrogen generation.

CONCLUSION

This research examined the photocatalytic activity of nanostructures of titanium and tungsten oxides. The results showed that the presence of tungsten precursors favored the photocatalytic properties of the samples, especially the $TiO_2/Na_2WO_4.2H_2O$ – 800°C films. The high temperature caused an increase in the kinetic energy of the molecules, which reacted quickly, increasing the reaction speed. This generated many vacancies of O_2 and hydroxyl radicals (OH) that quickly adsorbed on the surface of the sample. The association of these factors gave these samples an excellent photocatalytic performance.

REFERENCES

Barczuk, P. J., Tsuchiya, H., Macak, J. M., Schmuki, P., Szymanska, D., Makowski, O., Miecznikowski, K. & Kulesza, P. J. (2006). Enhancement of the electrocatalytic oxidation of methanol at Pt/Ru nanoparticles immobilized in different WO_3 matrices. *Electrochem. Solid State Letters*, E13–E16. doi.org/10.1149/1.2190597.

Basavarajappa, P. C., Shivaraj, B. P., Ganganagappa, N., Reddy, K. R., Raghu, A. V. & Reddy, Ch. V. (2020). Recent progress in metal-doped TiO_2, non-metal doped/codoped TiO_2 and TiO_2 nanostructured hybrids for enhanced photocatalysis. *International Journal of Hydrogen Energy*, 7764-7778. doi.org/10.1016/ j.ijhydene.2019.07.24.

Bharti, B., Kumar, S., Lee, H. N. & Rajesh, K. (2016). Formation of oxygen vacancies and Ti^{3+} state in TiO_2 thin film and enhanced optical properties by air plasma treatment. *Scientific Reports*, 1-12. doi.org/10.1038/srep32355.

Bolsoni, A. T. (2011). *Síntese, Cracterização e Estudos das Propriedades Catalíticas de Compostos de Tungstênio e Pentóxido de Vanádio*. 50p. Tese de Doutorado (Faculdade de Filosofia, Ciência e Letras de Ribeirão Preto) – Programa de Pós – Graduação em Química, Departamento de Química, Ribeirão Preto. [*Synthesis, Characterization and Studies of Catalytic Properties of Tungsten Compounds and Vanadium Pentoxide*]

Chen, S., Xiao, Y. Wang, Y. Hu, Z. Zhao, H. & Xie, W. (2018). A Facile approach to prepare black TiO_2 with oxygen vacancy for enhancing photocatalytic activity. *Nanomaterials*, 2-16. doi.org/10.3390/ nano8040245.

Duarte, T. A. G. (2013). Sodium tungstate dihydrate. *Revista Virtual Química*, 318-325. doi.org/10.5935/1984-6835.20130030.

Guaraldo, T. T. *Síntese e Aplicação de Filmes Bicomponentes Nanoestruturados de Ti/TiO_2/WO_3 por Template e Si/TiO_2/Pt por Heterojunção em Conversão de Energia Solar e Remediação Ambiental*. 2014. 219p. Tese de Doutorado (Instituto de Química de Araraquara) - Universidade Estadual Paulista, Araraquara. [*Synthesis and Application of Bicomponent Nanostructured Films of Ti/TiO2/WO3 by Template and Si/TiO2/Pt by Heterojunction in Solar Energy Conversion and Environmental Remediation*]

Ibrahim, N. S., Leaw, W. L., Mohamad, D., Siti, H. A. & Nur, H. (2020). A critical review of metal-doped TiO_2 and its structureephysical propertiesephotocatalytic activity relationship in hydrogen production. *International Journal of Hydrogen Energy*, 28553-28565. doi.org/10. 1016/j.ijhydene.2020.07.233.

Kantha, B., Shaw, R. N. & Ghosh, A. (2020). Influence of annealing temperatures in improving the sensitivity of Pd modified WO_3 nanoparticles based hydrogen sensor. *IEEE 5th International Conference on Computing Communication and Automation*, 780–784. doi.org/10.1109/ICCCA49541.2020.9250788.

Mourão, H. A. J. L. & Mendonça, V. R. (2009). Nanoestruturas em fotocatálise: uma revisão sobre estratégias de síntese de fotocatalisadores em escala nanométrica. *Química Nova*, 2181-2190. doi.org/10.1590/S0100-40422009000800032. [Nanostructures in photocatalysis: a review of nanoscale photocatalyst synthesis strategies. *New Chemistry*]

Farjood, M. & Zanjanchi, M. A. (2019). Template-free synthesis of mesoporous tungsten oxide nanostructures and its application in photocatalysis and adsorption reactions. *Chemistry*, 3042–3046. doi.org/10.1002/slct.201804007.

Feltrin, J., Sartor, M. N., De Noni, A. J., Bernardin, A. M., Hotza, D. & Labrincha, J. (2013). Superfícies fotocatalíticas de titânia em substratos cerâmicos. Parte I: Síntese, estrutura e fotoatividade. *Cerâmica*, 620-632. doi.org/10.1590/S0366-69132013000400020.

Fujishima, A. & Honda, K. (1972). Electrochemical photolysis of water at a semiconductor electrode. *Nature*, 37–38. doi.org/10.1038/ 238037a0.

Ge, M., Cai, J., Iocozzia, J., Cao, C., Huang, J., Zhang, X., Shen, J., Wang, S., Zhang, S., Zhang, K. Q., Lai, Y. & Lin, Z. (2017). A review of TiO_2 nanostructured catalysts for sustainable H_2 generation. *International Journal of Hydrogen Energy*, 7764-7778. *International Journal of Hydrogen Energy*, 8418-8449. doi.org/10.1016/j.ijhydene. 2016.12.052.

Hunge, Y. M. (2017). Sunlight assisted photoelectrocatalytic degradation of benzoic acid using stratified WO_3/TiO_2 thin films. *Ceramics International*, 10089–10096. doi.org/10.1016/j.ceramint.2017. 05.028.

Hunge, Y. M., Mahadik, M. A., Moholkar, A. V. & Bhosale, C. H. (2017). Photoelectrocatalytic degradation of oxalic acid using WO_3 and stratified WO_3/TiO_2 photocatalysts under sunlight illumination. *Ultrasonics Sonochemistry*, 233–242. doi.org/10.1016/ j.ultsonch. 2016.09.024.

Hromadko, L., Motola, M., Cicmancov, V., Bulanek, R. & Macak, J. M. (2021). Facile synthesis of WO_3 fibers via centrifugal spinning as an efficient UV and VIS-light-driven photocatalyst. *Ceramics International*, xxx-xxx. doi.org/10.1016/j.ceramint.2021.09.079.

Muccillo, E. N. S. (2008). Condutores de íons oxigênio - uma breve revisão. *Cerâmica*, 129-144. doi.org/10.1590/S0366-6913200800 0200002. [Oxygen ion conductors - a brief review. *Ceramics*]

Nagaraj, G., Dhayal, R., Irudayaraj, A. A. & Josephine, R. L. (2019). Tuning the optical band Gap of pure TiO_2 via photon induced Method. *Optik - International Journal for Light and Electron Optics*, 889–894. doi.org/10.1016/j.ijleo.2018.11.009.

Oshani, F., Marandi, R., Rasouli, S. & Farhoud, M. K. (2014). Photocatalytic investigations of TiO_2–P25 nanocomposite thin films prepared by peroxotitanic acid modified sol–gel method. *Applied Surface Science*, 308–313. doi.org/10.1016/j.apsusc.2014.05.059.

Rihova, M., Ince, A. E., Cicmancova, V. L., Hromadko, K., Castkova, D., Pavlinak, L., Vojtova, J. & Macak. M. (2021). Water-born 3D nanofiber mats using cost-effective centrifugal spinning: comparison with electrospinning process: a complex study. *J. Applied Polymer Science., 49975.* doi.org/10.1002/app.49975.

Rutledge, G. C. & Fridrikh, S. V. (2007). Formation of fibers by electrospinning. *Advanced Drug Delivery Reviews*, 1384–139. doi.org/10.1016/j.addr.2007.04.020.

Silva, F. O., Viol, L. C. S., Ferreira, D. L., Alves J. L. A. & Schiavon, M. A. (2010). O estado da arte da síntese de semicondutores nanocristalinos coloidais. *Quimica Nova*, 1933-1939. doi.org/ 10.1590/S0100-40422010000900021.

Soares, L. & Alves, A. (2018). Analysis of colorimetry using the CIE-L*a*b* system and the photocatalytic activity of photochromic films. *Materials Research Bulletin*, 318-321. doi.org/10.1016/ j.materresbull.2018.05.012.

Soares, L. G., Vaz, M. O., Teixeira, S. R. & Alves, A. K. (2021). Absorbance determination and photocatalytic production of hydrogen using tungsten and TiO_2 oxide nanostructures as catalyst. *Cleaner Engineering Technology*, 100268. doi.org/10.1016/ j.clet.2021. 100268.

Wu, M. C., Wu, P. Y., Lin, T. H. & Lin, T. (2018). Photocatalytic performance of Cu-doped TiO_2 nanofibers treated by the hydrothermal synthesis and air-thermal treatment. *Applied Surface Science*, 390–398. doi.org/10.1016/j.apsusc.2017.09.035.

Yang, H. *Electrospinning of polymeric and ceramic fibers: understanding of the morphological control and its application.* 2013, 136 p. University of Rochester, New York.

In: Fundamentals of Photocatalysis
Editor: Orva Auger
ISBN: 978-1-68507-374-9

Chapter 5

DESIGNING AN ENHANCED VISIBLE-LIGHT ACTIVATED HIERARCHICAL THREE-DIMENSIONAL AG/TIO$_2$ NANOWIRES/GRAPHENE SANDWICH PHOTOCATALYST

Tao Peng[1,3], PhD, Srimanta Ray[2,*], PhD
and Jerald A. Lalman[1], PhD
[1]Department of Civil and Environmental Engineering,
University of Windsor, Windsor, Ontario, Canada
[2]Department of Chemical Engineering, National Institute of
Technology Agartala, Tripura, India
[3]Advanced Research Institute, Shenzhen University, Shenzhen, China

---

[*] Corresponding Author's E-mail: rays.nita@gmail.com.

ABSTRACT

Graphene is of significance in photocatalysis because of its high electric charge carrier mobility and optical transparency, intrinsic large surface and capability of chemical functionalization. Increasing surface area is known to increase the photocatalytic efficiency. One dimension (1-D) TiO_2 nanowires (TNW) is of recent interest because the structure is less prone to agglomeration when compared to TiO_2 nanoparticles. The fabrication and evaluation of TNWs supported on graphene and sensitized with Ag in a unique hierarchical three-dimensional (3-D) sandwich structure is reported in this study. The Ag/TNW/graphene (Ag/TNWs/G) 3-D photocatalyst demonstrated that the surface plasmon resonance (SPR) effect caused by Ag nanoparticles resulted in strong and broad absorption bands for the photocatalyst over the ultraviolet and visible region. The TNWs and graphene in the 3-D Ag/TNWs/G composite increased the specific surface area (SSA) by a factor of approximately 5.4 when compared to commercial TiO_2 nanoparticles (P25). The high SSA contributed to increasing the adsorption of pollutants. The photocatalyst sandwich was able to decompose methylene blue (MB), a model pollutant, efficiently using visible-light. The MB degradation rate was approximately 32-fold greater than for P25 and approximately 2-fold greater than for TNWs/G. Coupling the characteristics of graphene with the SPR properties of Ag nanoparticles in the 3-D hierarchical sandwich could be a promising strategy for preparing other noble metal and carbon based TiO_2 nanotube composite photocatalysts for various application

Keywords: photocatalysts, graphene, TiO_2 nanowire, surface plasmon resonance, Ag nanoparticle

INTRODUCTION

Titanium dioxide (TiO_2) has emerged as a promising photocatalyst because of its superior high oxidizing power, non-toxic properties, chemical inertness as well as photo-stability against the strong oxidation environment in photocatalytic degradation applications (Du et al. 2011, Asahi et al. 2001). However, the photocatalytic performance of TiO_2 using visible light is low because of the fast recombination of photo-generated electron-hole pairs and the limited optical response in the light spectrum. The photoactivity of TiO_2 can be enhanced by coupling with a noble metal, metal ion doping, anion doping and incorporating electron-accepting materials such as carbon nanotubes or graphene (Asahi et al. 2001, Fakhouri et al. 2014, Smith et al. 2012, Wen et al. 2011, Xian et al. 2015, William et al. 2008). These methods have been used to suppress the recombination of photo-generated electron-hole pairs or extend the optical absorption in the visible light region. However, improving the performance is still insufficient for commercial use because of the low adsorbability of pollutants, limited response to visible light and poor charge separation (Du et al. 2011, Xian et al. 2015, Yang et al. 208, Shen et al., 2011).

A significant amount of work to optimize the photocatalytic properties of TiO_2 has mainly been focused on increasing the pollutant adsorption on TiO_2-based photocatalysts by increasing the specific surface area (SSA) and the mass transfer capacity, enhancing the optical absorption of visible light and increasing the charge separation of TiO_2 (Xian et al. 2015, Yang et al. 208, Shen et al., 2011). Graphene is considered an ideal material for improving the photocatalytic activity of TiO_2 because of its superior charge transport properties and high SSA (Novoselov et al. 2012, Geim 2009). Enhanced photocatalytic activity of TiO_2-graphene nanocomposites is reported by many researchers (William et al. 2008, Tu et al. 2012, Zhang et al. 2010). However, combining TiO_2 nanoparticles and graphene has several challenges because the nanoparticles tend to agglomerate and the poor interfacial contact between nanoparticles and the graphene surface. A possible solution to resolve this challenge is to design a 1-dimension (1-D) TiO_2 nanostructure (TN) which is less prone to agglomerate when compared to TiO_2 nanoparticles (Pan et al. 2012, Perera et al. 2012).

Another major disadvantage of TiO_2 photocatalyst is their poor activity in the visible light region. Recently, several researchers have demonstrated improved visible-light photocatalysis using noble-metal-loaded TiO_2 nanotubes or nanowires. This improvement in photocatalytic activity is due to the surface plasmon resonance (SPR) effect of noble metal nanoparticles and the improved morphology of TiO_2 (Wen et al. 2011, Liang et al. 2011, Yang et al. 2013, Li et al. 2012, Zhang et al. 2013, Matsubara and Tatsuma 2007, Linic et al. 2011). The objectives of the present study were to synthesize a visible-light activated hierarchical 3-D Ag/TiO_2 nanowires/graphene (Ag/TNW/RGO) sandwich and to assess the photocatalytic ability of the catalyst using visible light. The work integrated the SPR properties of Ag nanoparticles (0-D), the unique 1-D structure of TNW and the excellent electrical properties of graphene (2-D) as a means to synthesize a photocatalyst capable of visible light activation.

EXPERIMENTAL METHODS

Materials

Commercial TiO_2 nanoparticles (P25) were purchased from Degussa (now Evonik Industries, Germany). Graphite flakes (325 mesh, 99.9995%), $AgNO_3$ (99.995%), $NaBH_4$, $KMnO_4$ (99.0%) and KOH were procured from Alfa Aesar (MA, USA). H_3PO_4, H_2SO_4, H_2O_2, ethanol and HCl were purchased from Fischer Scientific (Ontario, Canada). Hydrazine hydrate (50-60%) and dialysis were purchased from Sigma-Aldrich (Ontario, Canada) (proteins M.W. cut-off > 12,000 Da).

Synthesis

Graphene Oxide (GO) Synthesis

GO was synthesized using an improved Hummer's method (Marcano et al., 2010). Briefly, a 9:1 mixture of concentrated H_2SO_4/H_3PO_4 (360:40 ml) was added to a mixture of graphite flakes (3.0 g) together with $KMnO_4$ (18.0 g) in a 1 L beaker. The solution was heated to 50°C and simultaneously stirred for 24 h. The reaction solution was cooled to room temperature and poured onto ice flakes (400 mL).

Five mL of 30% H_2O_2 was added to the mixture and the yellow mixture was centrifuged at 5,000 rpm for 2 h. After centrifugation, the yellow solid was washed with water (200 mL), followed by washing with 30% HCl (200 mL) and subsequently, with 6 washes of ethanol (200 mL). After each washing, the mixture was centrifuged (5,000 rpm for 2 h) and the supernatant decanted. Finally, the yellow solid was dialyzed against Milli-Q water to remove residual metal ions. The solution was placed in a dialysis bag and vacuum-dried at 50°C to yield 5.8 g of GO powder.

Ag/TNW/RGO Synthesis

The procedure to synthesize the Ag/TNW/RGO nanocomposite using an alkaline hydrothermal treatment approach is outlined in Figure 1 (Peng, 2018). Briefly, GO (10% w/w) (300 mg) and P25 (2.7 g) were mixed and ultra-sonicated in 60 mL Milli-Q water for 1 h to ensure re-exfoliating of the GO and inserting P25 nanoparticles between the GO sheets. Next, 45g KOH was added to the GO plus P25 mixture with stirring for 1 hour. The mixture was poured into a 100 mL Teflon® capped container. The Teflon® container was placed into a stainless-steel bottle then capped, heated at 200 °C for 24 h and subsequently, cooled to room temperature. The resulting gray gel was mixed with 200 mL 0.1 M HCl and stirred for 1 hour. The product TNW/GO was repeatedly washed with DI water, centrifuged and dried at 80 °C. The mixture was diluted to 100 ml, and then 1 ml of hydrazine hydrate was added with stirring. The mixture was heated to 95 °C in a water bath for 45 min with the production of a black solid precipitate. The TNW/RGO product was isolated by filtration (PTFE 20 um pore size) and washed 3 times with DI water and methanol, dried at 60°C for 12h and calcinated at 700°C in N_2 for 1 h. The TNW/RGO (approximately 0.5 g) was dispersed in 30 ml DI water and 20 ml of a 0.1 mol/L $AgNO_3$ aqueous solution was added to the suspension. The mixture was stirred for 20 min, filtered, washed and dried at 25 °C. The powder was added to 20 ml of 25 mg/ml $NaBH_4$ aqueous solution and the mixture stirred at room temperature for 30 min, filtered, washed with DI water and dried at 60 °C to produce the Ag/TNW/RGO composite.

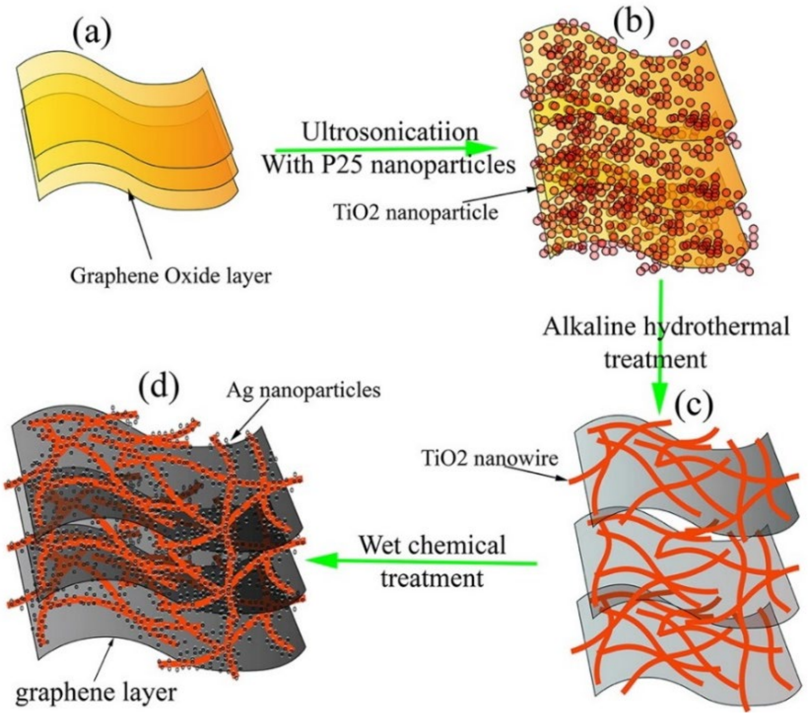

Figure 7. Schematic process showing the synthesis of the hierarchical 3-D Ag/TNW/RGO sandwich photocatalyst via a two-step facile route. Note: The photocatalyst was synthesized by homogeneously growing TNW on graphene surface via an alkaline hydrothermal process and this was followed by a hydrazine hydrate reduction and the deposition of Ag nanoparticles on the TNW. The GO sheets (a) were exfoliated and (b) homogeneously decorated with P25 nanoparticles, (c) next, P25 nanoparticles were grown as TNW on sheets and (d) finally most of the GO sheets were reduced to graphene sheets, with hydrazine hydrate reduction, and Ag nanoparticles were grown on TNW (Peng, 2018).

Characterization

The morphological characterization of the samples was examined using scanning electron microscopy (SEM) (JEOL, Japan) and transmission electron microscopy (TEM) (JEOL 3010, Japan. The X-ray diffraction (XRD) analysis was performed using an X-ray diffractometer (Rigaku, MI, United States) equipped with Cu K∂ radiation source. Raman analysis was conducted using an Alpha300 RA argon laser Raman spectrometer (WITec, Germany) with excitation at 532 nm. UV-Vis spectra analysis was performed using a Cary 300 UV-Vis (Agilent Technologies, Ontario, Canada). Nitrogen adsorption–desorption isotherms were recorded at 77 K with a Micromeritics ASAP 2020 Brunauer–Emmett–Teller (BET) analyzer (Georgia, USA).

Photocatalytic Degradation

The photodegradation ability of the composites was assessed using methylene blue (MB) as a model pollutant. The photocatalytic experiments were conducted in custom-manufactured reaction tubes (25 mm ID ×250 mm length) fabricated from GE-214 clear fused quartz silica (Technical Glass Products Inc., Painesville, OH, USA). The reaction tubes were sealed with Teflon® lined 20 mm septas and aluminum crimp caps (Cobert Associates, St. Louis, MO). The sealed photocatalytic reaction tubes were placed in a modified Rayonet RPR-100 UV photocatalytic chamber (Southern New England Ultraviolet Co., Branford, CT, USA). The chamber was equipped with sixteen lamps on the outer perimeter with a centrally located rotating inner carousel. The inner carousel was set at a constant rotational speed to minimize variation in irradiance between reaction tubes. Three fused quartz reaction tubes triplicates were placed on the inner rotating carousel and the contents were magnetically stirred to maintain the catalyst in suspension, minimize particle agglomeration and also minimize any mass transfer limitation. The average irradiance emitted from the lamps was 9 mW/cm^2 measured for 300 nm monochromatic UV light. The radiation intensity was measured using a calibrated UV-X radiometer equipped with a 300nm UV sensor (UV Process Supply, Chicago, IL). The constant reactor temperature was maintained by placing the UV reaction vessel in a temperature controlled chamber (Ray et al. 2009). All the photocatalytic experiments were performed at 37±2 ◦C (310 ± 2 K). The photocatalytic experiments with MB in ultrapure (Milli-Q) water were conducted without further pH adjustment.

RESULTS

Characterization Studies

Microscopic and Surface Area Analysis

Formation of the hierarchical 3-D Ag/TNW/RGO composite was demonstrated by high-resolution transmission electron microscopy (HRTEM) (Figure 2). The TNW interconnecting network was homogeneously grown on the surface of graphene sheets. Transmission electron microscopy (TEM) images for the Ag/TNW/RGO composite (Figure 2a) indicate that the TNW were attached to the graphene sheets surface. The TNW with an average diameter of approximately 7 nm and length greater than 100 nm (Figure 2a) were homogeneously decorated with Ag nanoparticles (shown as dark regions in Figure 2b). TNW with diameters of approximately 4-fold smaller than the P25 nanoparticles were useful in producing a Ag/TNW/RGO composite with an enhanced photoreactive specific surface area (SSA) (270 m^2/g) when compared to P25 with a SSA of 50 m^2/g (Table 1). Ag nanoparticles with an average diameter of 3 nm were grown on the TNW surface (Figure 2b). Ag^+ ions introduced after the formation of TNW/G composite were preferably adsorbed on the TiO_2 hydrophilic surface instead of on the hydrophobic graphene sheet surface. During reduction with $NaBH_4$, Ag nanoparticles were grown on the TNW. The TNW uniform attachment by Ag nanoparticles indicates that they were homogeneously grown on the graphene sheets in Ag/TNW/RGO.

Table 1. Specific surface area (SSA) for P25, TNW and composites

Sample	**SSA (m^2/g)**
P25	47 ± 4
TNW	253 ± 14
TNWs/RGO	301 ± 17
Ag/TNWs/RGO	272 ± 14

Note: SSA determined using the Brunauer-Emmett-Teller (BET) method.

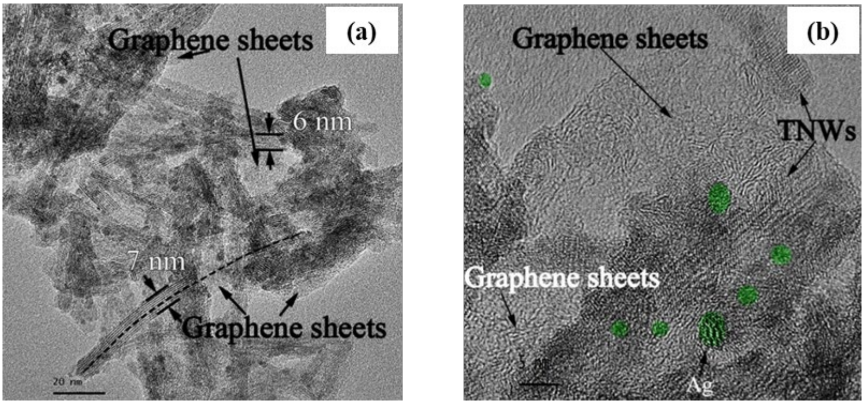

Figure 2. TEM images for different structures. (a) Ag/TNW/RGO TEM image. (b) Ag/TNW/RGO TEM image with Ag nanoparticles indicated in green.

XRD Analysis

The XRD peak for flake graphite at $2\theta = 26.5^{\circ}$ corresponds to the d_{002} basal spacing (Lim et al. 2011) of approximately 0.34 nm while in comparison, the XRD pattern for GO shows a characteristic peak at $2\theta = 10.1^{\circ}$ (Figure 3a). This characteristic peak, consistent with a GO d_{002} basal spacing, increase from 0.34 nm to 0.88 nm. The increase is due to the attachment of oxygen-containing functional groups generated by the oxidation process (Marcano et al., 2010, Hernandez et al. 2008). The GO sheets, which consist of a few GO layers or an individual layer with greater interlayer spacing, was uniformly dispersed in water by ultra-sonication (Marcano et al., 2010). This allowed the P25 nanoparticles to be uniformly decorated on and between the graphene layers. When the P25/GO mixture was treated hydrothermally, GO reduction to graphene caused weakening and upshifting of the (002) peak. In general, reduction of pure GO caused upshifting of the (002) peak to a higher value at $2\theta = 26.5^{\circ}$. According to Zhu et al. (2011), this upshifting is due to the agglomeration of graphene sheets and recession of the d_{002} basal spacing to approximately 0.335 nm. Agglomeration of graphene sheets is known to decrease the SSA (Zhu et al., 2011). However, the TNW-based composites (002) with a peak at $2\theta = \sim 15^{\circ}$ (a broad band in Figure 3a) indicates that the graphene sheets retained a larger interlayer spacing.

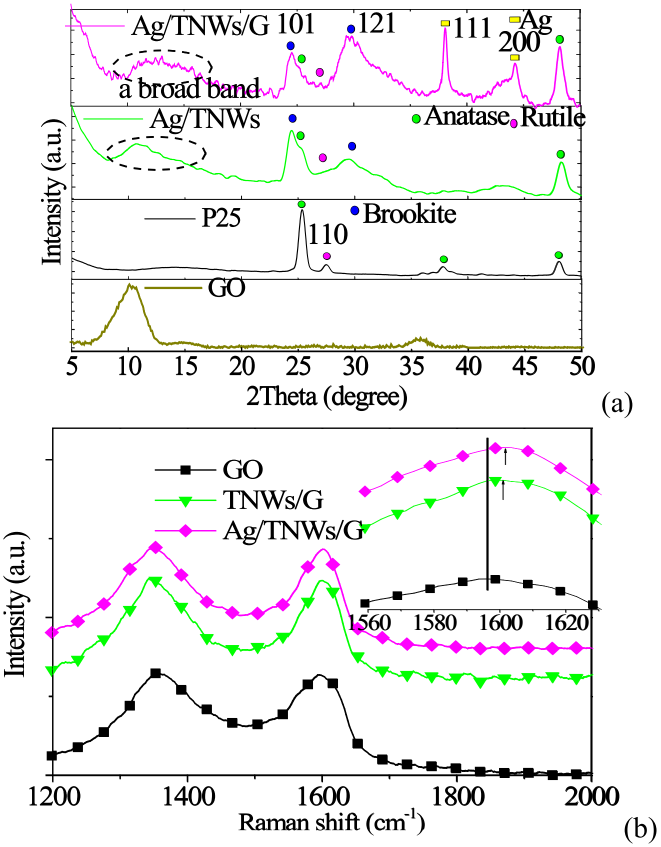

Figure 3. XRD and Ramam spectra. (a) XRD patterns for all samples. (b) Raman spectra for different samples. Characteristic of D and G bands for GO and the Graphene-based TiO_2 composites. Inset Raman spectra showing the blue shifts for G peaks and the blue shift for the E_g bands for the composites.

The larger spacing between the graphene sheets was maintained by the homogeneous growth of TNW between the layers. The TNWs serving as a bridge were able to inhibit the agglomeration of graphene layers. The larger interlayer spacing of the graphene sheets in Ag/TNW/RGO is essential in order to maintain a high SSA (Fan et al., 2010). Increasing the SSA caused increasing adsorption of MB molecules and reactive sites for degrading MB. The XRD patterns from 23° to 33° for TNW/RGO and Ag/TNW/RGO exhibited peaks at 25.4° (anatase (101)), 27.5° (rutile (110)) and two additional peaks at 24.5° (brookite (101)) and 29.6°

(brookite (121)) when compared with P25 (Figure 3a) (Iskandar et al. 2007). The XRD peaks for Ag/TNW/RGO and Ag/P25/G at 38.1° and 44.3° correspond to the 3C-Ag (111) and 3C-Ag (200) surfaces, respectively (Figure 3a), and the TEM results (Figure 2b).

Raman Analysis

Raman spectroscopy was employed to confirm changes in the chemical structure and phase transition of the GO and the graphene-based composites. The Raman spectra of the GO and the graphene-based composites (Figure 3b) show the D and G peaks at ~1347 cm^{-1} and ~1600 cm^{-1}, respectively. The D peak is a breathing mode of A_{1g} symmetry and is related to the occurrence of defects and structural disorder in graphene sheet (Ferrari and Robertson, 2000). The D mode is forbidden; however, it is allowed with the occurrence of defects (Ferrari and Robertson, 2000, Ferrari et al. 2006). The G mode with E_{2g} symmetry corresponds to bond stretching of all pairs of sp^2 atoms in both ring and chain carbon structures (Ferrari et al. 2006). The integrated intensity ratio of the D band to the G band reflects the order of defects in GO and graphene (Perera et al. 2012, Kudin et al. 2008). The calculated integrated I_D/I_G ratio for GO was 2.13, while for TNW/RGO and Ag/TNW/RGO, the I_D/I_G ratios were 1.37, and 1.19, respectively. The decreasing integrated I_D/I_G ratio suggests that GO was successfully reduced and the graphene content increased by removing or repairing defects in the carbon atom sheets during hydrothermal treatment and wet chemical treatment (Wang et al. 2011). Successful reduction of the defective GO is crucial in recovering the electrical properties of graphene because the reduced structure is responsible for facilitating charge separation (Perera et al. 2012). In addition, a blue shift in the G band was also observed in all the composites when compared to GO, graphene and graphite (~1580 cm^{-1}) (Ferrari et al. 2006). The blue shift was caused by the strong interaction or strain between graphene and TiO_2 (Wen et al. 2011, Shen et al. 2011). This enhanced interaction is able to facilitate the charge transfer between TiO_2 and graphene and extend the light absorption range (Wen et al. 2011, Pan et al. 2012).

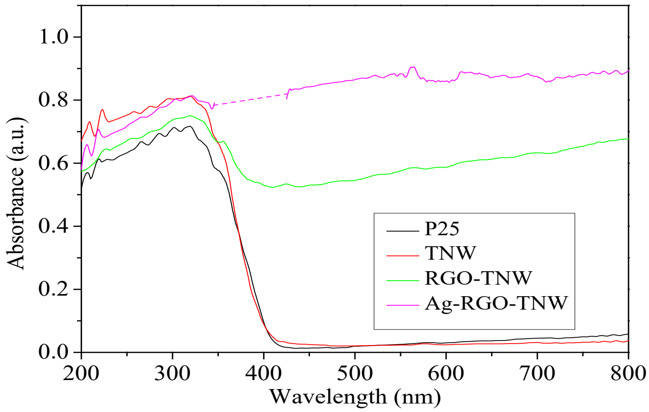

Figure 4. UV-vis absorption spectra for P25, TNW, TNWs/G and Ag/TNWs/G.

Diffuse Reflectance UV-Vis Spectroscopy (DRS)

Diffuse reflectance UV-Vis spectroscopy (DRS) (Figure 4) was used to further examine the optical response of the samples. When compared to P25, the slightly stronger TNW optical absorption band in the visible-light region (Figure 4) suggests TNW is a suitable substitute for P25. In all the graphene-based composites, adding graphene could likely induce increased light absorption intensity in the visible-light region. According to Zhang et al. (2010) and Fan et al. (2011), the absorption edge red P25 shift caused by adding graphene indicate that narrowing the P25 band gap is due to the interaction between TiO_2 and graphene. In this study, a red shift of the absorption edge was also observed after adding graphene to TNW. Moreover, when compared to TNW/RGO, the higher absorption band wavelengths from 400 to 800 nm for the hierarchical 3-D Ag/TNW/RGO composite is due to the localized SPR absorption of the Ag nanoparticles (Wen et al. 2011, Ohko et al. 2002). The broad absorption band for the hierarchical 3-D Ag/TNW/RGO composite indicates photocatalytic activity in the visible light region.

Photocatalytic Degradation Studies

Under visible light irradiation after 60 min, MB molecules were degraded by P25, TNW and the composites (Figure 5). However, notice the MB degradation rate for P25 was low while a higher degradation rate was observed for TNW. MB degradation was enhanced significantly by decorating TNW with graphene. This enhancement can be attributed to interaction between TNW and graphene (Chen et al, 2010a). The MB solution became colorless after 30 min in the presence of Ag/TNW/RGO. The MB degradation rate for Ag/TNW/RGO under visible light illumination for 30 min was approximately 6-fold that of P25 and 2.0-fold greater than the TNW/RGO composite. The rapid adsorption and high degradation rate of MB is evidence of the high performance of the Ag/TNW/RGO composite.

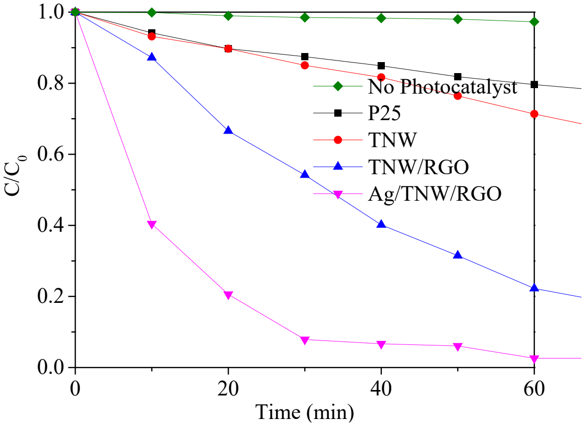

Figure 5. Plot of C/C_0 versus time for the photocatalytic degradation of MB. C_0 is the concentration of MB at time of 0 min after 1 h adsorption.

DISCUSSION

The gradual sequential assessment of the different nanoparticles and composites and the development of a hierarchical 3-D Ag/TNW/RGO, a highly active visible light photocatalyst, is attributed to several factors. MB degradation includes MB adsorption, absorption of visible light by the photocatalyst to generate electrons and holes, and finally charge transfer to reactive surface to create radical species such as $\bullet O_2$-/$\bullet OH$ and H_2O_2 to decompose MB (Perera et al. 2012, Chen et al, 2010b). A key factor in achieving a highly active photocatalyst is the unique hierarchical 3-D structure of the Ag/TNW/RGO composite.

The hierarchical 3-D Ag/TNW/RGO high adsorbability capacity is crucial for achieving higher photocatalytic degradation rates. The high adsorption of MB on the surface of the Ag/TNW/RGO composite significantly increased the concentration of the MB molecules near the catalytic surface thus, facilitating photocatalytic degradation. The higher MB adsorption on the Ag/TNW/RGO composite and subsequent degradation is due to both the graphene content and the unique 1-D structure of the TNW. Adding graphene is crucial for high adsorbability for Ag/TNW/RGO and other similar graphene-based composites (Mohan et al. 2018). MB adsorption is dependent on the graphene surface π-bonding characteristics. The strong π-π interaction between MB and the graphene aromatic structure enhanced MB adsorption (Perera et al. 2012). Also, the homogenous growth of 1-D TNW between the graphene sheets inhibited the agglomeration of graphene sheets and improved MB adsorption. The TEM morphology pattern (Figure 2) provided evidence of inhibiting agglomeration of graphene sheets and the XRD results show larger interlayer spacing between the graphene sheets (Figure 3a). The spacing between 1-D TNW served as a channel to facilitate MB transfer to the reactive surfaces. As a result, high adsorption of MB was achieved with the hierarchical 3-D Ag/TNW/RGO structure.

Enhancing visible light absorption is another reason for the increased reaction kinetics. In the unique hierarchical 3-D structure, both graphene and Ag nanoparticles could extend the absorption band edge of TiO_2 into the visible light region. Graphene was able to provide TiO_2 with an extended light absorption range and improve the visible light absorption intensity by narrowing the band gap (Lee et al. 2012). This was demonstrated by all the graphene-based composites with higher absorption in the visible light region when compared to P25 nanoparticles and TNW (Figure 4). Note that the Ag/TNW/RGO composite showed highest absorption in visible light because of the strong interaction between TNW and graphene as well as the localized SPR of the silver nanoparticles in the hierarchical 3-D Ag/TNW/RGO composite (Wen et al. 2011, Fan et al. 2011). SPR is defined as the resonant photon-induced collective oscillation of valence electrons which is produced when the photon frequency is equal to the natural frequency of surface electrons oscillating against the restoring force of positive nuclei (Linic et al. 2011). The SPR excited electrons can be transferred to the TNW conductance band and be subsequently trapped by adsorbed molecular oxygen on the large TNW surface to produce superoxide anion radicals ($\bullet O_2^-$). The SPR electrons was also likely to move from the TNW conductance band directly to the graphene sheets to produce $\bullet O_2^-$ (Wen et al. 2011). The highly efficient charge separation is another explanation for the enhanced performance of the hierarchical 3-D Ag/TNW/RGO composite. The efficient charge separation is attributed to both the unique 1-D structure of TNW and the strong interaction between TNW and graphene (Pan et al. 2012, Perera et al. 2012). The unique sandwich composite structure provided a direct path for excited electrons to travel from the Ag nanoparticles and from TNW to the graphene sheets. This has been reported to prevent carrier scattering between the nanoparticles, a common phenomenon in nanoparticle systems (Pan et al. 2012). Graphene, an efficient electron transporter, induces electron transfer from the TiO_2 conduction band to itself, while the hole trapped in the TNW had a longer lifetime (Wen et al. 2011, Perera et al. 2012). This was demonstrated by the fact that TNW and TNW composites have higher MB photodegradation rate than P25. (Figure 5) The electrons are eventually captured by adsorbed molecular oxygen on the graphene surface to produce $\bullet O_2^-$, while the holes accept electrons from H_2O or OH^- on the TiO_2 surface to produce hydroxyl radicals ($\bullet OH$). Subsequently, these highly reactive radicals oxidize organic molecules such as MB. The much higher TNW SSA (Table 1) provided more reactive sites for producing reactive species such as $\bullet OH$ when compared to P25. However, the efficiency of graphene as an electron scavenger is strongly dependent on the interfacial interaction between graphene and TiO_2. According to Xiang et al. (2012), a simple mechanical mixture of graphene and TiO_2 cannot enhance the photocatalytic activity of TiO_2 because the poor interfacial interaction is the principle cause for poor transfer of photoexcited electrons between graphene and TiO_2. In this work, the strong interaction between graphene and TNW in the Ag/TNW/RGO composite favored the transfer of photoexcited electrons from the TiO_2 conduction band to the graphene sheets ultimately facilitated the charge separation efficiency. The Raman spectra (Figure 3b) and the high photodegradation rate of MB (Figure 5) provided evidence of the strong interaction between TNW and RGO.

CONCLUSION

In summary, the hierarchical 3-D Ag/TNW/RGO photocatalyst was successfully synthesized and examined as an advanced photocatalyst. The photocatalyst was effective in degrading MB using visible light. The homogeneously growth of 1-D TNW between graphene sheets exposed more accessible surface of graphene sheets for significantly enhanced adsorption of pollutants. Both graphene sheets and SPR of Ag nanoparticles narrowed the band gap of TNW and therefore, significantly extended the light-response range to visible light. The unique 1-D structure of TNW and the strong interaction between TNW and graphene were responsible for the high efficient charge separation. As a result, the faster MB degrading rate in the presence of visible-light over a 30-minute period was approximately 6-fold greater than for P25 and approximately 2-fold greater than for TNW/RGO. Hence, this unique hierarchical 3-D Ag/TNW/RGO sandwich structure can be utilized efficiently to degrade organic pollutants in wastewater effluents and drinking water supplies.

ACKNOWLEDGEMENTS

Financial support for this work was provided by the Natural Sciences and Engineering Research Council (NSERC) of Canada (grant number 261797-2009), the Canada Research Chair (CRC) program (grant number 950-203725) and the University of Windsor (grant number 13320) and the MITACS grant (Application reference number IT05633).

REFERENCES

Asahi, R., Morikawa, T., Ohwaki, T., Aoki, K., and Taga, Y. (2001). Visible-Light Photocatalysis in Nitrogen-Doped Titanium Oxides. *Science*, 293, 269–271.

Chen, C., Cai, W., Long, M., Zhou, B., Wu, Y., Wu, D., and Feng, Y. (2010a). Synthesis of Visible-Light Responsive Graphene Oxide/TiO_2 Composites with P/N Heterojunction. *ACS Nano*, 4, 6425–6432

Chen, C., Ma, W., Zhao, J. (2010b). Semiconductor-Mediated Photodegradation of Pollutants under Visible-Light Irradiation. *Chemical Society Reviews*, 39, 4206–4214.

Du, J., Lai, X., Yang, N., Zhai, J., Kisailus, D., Su, F., Wang, D., and Jiang, L. (2011). Hierarchically Ordered Macro-Mesoporous TiO_2-Graphene Composite Films: Improved Mass Transfer, Reduced Charge Recombination, and Their Enhanced Photocatalytic Activities. *ACS Nano,* 5, 590–596.

Fakhouri, H., Pulpytel, J., Smith, W., Zolfaghari, A., Mortaheb, H. R., Meshkini, F., Jafari, R., Sutter, E., and Arefi-Khonsari, F. (2014). Control of the Visible and UV Light Water Splitting and Photocatalysis of Nitrogen Doped TiO_2 Thin Films Deposited by Reactive Magnetron Sputtering. *Applied Catalysis B, Environmental*, 144, 12–21.

Fan, Z., Yan, J., Zhi, L., Zhang, Q., Wei, T., Feng, J., Zhang, M., Qian, W., and Wei, F. A. (2010). Three-Dimensional Carbon

Nanotube/Graphene Sandwich and Its Application as Electrode in Supercapacitors. *Advanced Materials*, 22, 3723–3728.

Fan, W., Lai, Q., Zhang, Q., and Wang, Y. (2011). Nanocomposites of TiO_2 and Reduced Graphene Oxide as Efficient Photocatalysts for Hydrogen Evolution. *Journal of Physical Chemistry C*, 115, 10694–10701

Ferrari, A. C., and Robertson, J. (2000). Interpretation of Raman Spectra of Disordered and Amorphous Carbon. *Physical Review B: Condensed Matter and Materials*, 61, 14095–14107

Ferrari, A. C., Meyer, J. C., Scardaci, V., Casiraghi, C., Lazzeri, M., Mauri, F., Piscanec, S., Jiang, D., Novoselov, K. S., Roth, S., et al. (2006). Raman Spectrum of Graphene and Graphene Layers. *Physical Review Letters*, 97, 187401–187404.

Geim, A. K. (2009). Graphene: Status and Prospects. *Science*, 324, 1530–1534.

Hernandez, Y., Nicolosi, V., Lotya, M., Blighe, F. M., Sun, Z., De, S., McGovern, I. T., Holland, B., Byrne, M., and Gun'Ko, Y. K., et al. (2008). High-Yield Production of Graphene by Liquid-Phase Exfoliation of Graphite. *Nature Nanotechnology*, 3, 563–568.

Iskandar, F., Nandiyanto, A. B. D., Yun, K. M., Hogan, C. J., Okuyama, K., and Biswas, P. (2007). Enhanced Photocatalytic Performance of Brookite TiO_2 Macroporous Particles Prepared by Spray Drying with Colloidal Templating. *Advanced Materials*, 19, 1408–1412.

Kudin, K. N., Ozbas, B., Schniepp, H. C., Prud'homme, R. K., Aksay, I. A., and Car, R. (2008). Raman Spectra of Graphite Oxide and Functionalized Graphene Sheets. *Nano Letters*, 8, 36–41.

Liang, Y.-C., Wang, C.-C., Kei, C.-C., Hsueh, Y.-C., Cho, W.-H., and Perng, T.-P. (2011). Photocatalysis of Ag-Loaded TiO_2 Nanotube Arrays Formed by Atomic Layer Deposition. *Journal of Physical Chemistry C*, 115, 9498–9502.

Li, H., Lu, W., Tian, J., Luo, Y., Asiri, A. M., Youbi, Al, A. O., and Sun, X. (2012). Synthesis and Study of Plasmon-Induced Carrier Behavior at Ag/TiO_2 Nanowires. *Chemistry - A European Journal*, 18, 8508–8514.

Linic, S., Christopher, P., and Ingram, D. B. (2011). Plasmonic-Metal Nanostructures for Efficient Conversion of Solar to Chemical Energy. *Nature*, 10, 911–921.

Lim, H. N., Huang, N. M., Lim, S. S., Harrison, I., and Chia, C. H. (2011). Fabrication and Characterization of Graphene Hydrogel via Hydrothermal Approach as a Scaffold for Preliminary Study of Cell Growth. *International Journal of Nanomedicine*, 6, 1817.

Lee, J. S., You, K. H., and Park, C. B. (2012). Highly Photoactive, Low Bandgap TiO_2 Nanoparticles Wrapped by Graphene. *Advanced Materials*, 24, 1084–1088.

Marcano, D. C., Kosynkin, D. V., Berlin, J. M., Sinitskii, A., Sun, Z., Slesarev, A., Alemany, L. B., Lu, W., and Tour, J. M. (2010). Improved Synthesis of Graphene Oxide. *ACS Nano*, 4, 4806–4814.

Matsubara, K., and Tatsuma, T. (2007). Morphological Changes and Multicolor Photochromism of Ag Nanoparticles Deposited on Single-Crystalline TiO_2 Surfaces. *Advanced Materials*, 19, 2802–2806.

Mohan, V.B., Kin-tak, L., Hui, D., Bhattacharyya, D. (2018). Graphene-based materials and their composites: A review on production, applications and product limitations. *Composites Part B: Engineering*, 142, 200-220.

Novoselov, K. S., Ko, V. I. F., Colombo, L., Gellert, P. R., Schwab, M. G., and Kim, K. (2012). A Roadmap for Graphene. *Nature*, 490, 192–200.

Ohko, Y., Tatsuma, T., Fujii, T., Naoi, K., Niwa, C., Kubota, Y., and Fujishima, A. (2002). Multicolour Photochromism of TiO_2 Films Loaded with Silver Nanoparticles. *Nature Materials*, 2, 29–31.

Pan, X., Zhao, Y., Liu, S., Korzeniewski, C. L., Wang, S., and Fan, Z. (2012). Comparing Graphene-TiO2 Nanowire and Graphene-TiO_2 Nanoparticle Composite Photocatalysts. *ACS Applied Materials & Interfaces*, 4, 3944–3950.

Perera, S. D., Mariano, R. G., Vu, K., Nour, N., Seitz, O., Chabal, Y., and Balkus, K. J., Jr. (2012). Hydrothermal Synthesis of Graphene-TiO_2 Nanotube Composites with Enhanced Photocatalytic Activity. *ACS Catalysis*, 2, 949–956.

Ray, S., Lalman, J.A., and Biswas, N. (2009). Using the Box-Benkhen technique to statistically model phenol photocatalytic degradation by titanium dioxide nanoparticles. *Chemical Engineering Journal*, 150, 15–24

Shen, L., Zhang, X., Li, H., Yuan, C., and Cao, G. (2011). Design and Tailoring of a Three-Dimensional TiO2–Graphene–Carbon Nanotube Nanocomposite for Fast Lithium Storage. *Journal of Physical Chemistry Letters*, 2, 3096–3101.

Smith, W., Fakhouri, H., Pulpytel, J. M., and Arefi-Khonsari, F. (2012). Control of the Optical and Crystalline Properties of TiO_2 In Visible-Light Active TiO_2/TiN Bi-Layer Thin-Film Stacks. *Journal of Applied Physics*, 111, 024301–024311.

Peng, T. (2018). Synthesizing Efficient Quasi-one-dimension Titanium Dioxide Nanocatalyst for Enhanced Photocatalytic Degradation of Aqueous Organic Pollutants and Hydrogen Production. *University of Windsor, Electronic Theses and Dissertations*, 7557.

Tu, W., Zhou, Y., Liu, Q., Yan, S., Bao, S., Wang, X., Xiao, M., and Zou, Z. (2012). An in Situ Simultaneous Reduction-Hydrolysis Technique for Fabrication of TiO_2-Graphene 2D Sandwich-Like Hybrid Nanosheets: Graphene-Promoted Selectivity of Photocatalytic-Driven Hydrogenation and Coupling of CO_2 Into Methane and Ethane. *Advanced Functional Materials*, 23, 1743–1749.

Wang, P., Han, L., Zhu, C., Zhai, Y., and Dong, S (2011). Aqueous-Phase Synthesis of Ag-TiO_2-Reduced Graphene Oxide and Pt-TiO_2-Reduced Graphene Oxide Hybrid Nanostructures and Their Catalytic Properties. *Nano Research*, 4, 1153–1162.

Wen, Y., Ding, H., and Shan, Y. (2011). Preparation and Visible Light Photocatalytic Activity of Ag/TiO_2/Graphene Nanocomposite. *Nanoscale*, 3, 4411–4417.

Williams, G., Seger, B., and Kamat, P. V. (2008). TiO_2-Graphene Nanocomposites. UV-Assisted Photocatalytic Reduction of Graphene Oxide. *ACS Nano*, 2, 1487–1491.

Xiang, Q., Yu, J., and Jaroniec, M. (2012). Synergetic Effect of MoS_2 and Graphene as Co-catalysts for Enhanced Photocatalytic H_2 Production

Activity of TiO_2 Nanoparticles. *Journal of the American Chemical Society*, 134, 6575–6578

Xiang, Q., Cheng, B., and Yu, J. (2015). Graphene-Based Photocatalysts for Solar-Fuel Generation. *Angewandte Chemie*, 127, 11508–11524.

Yang, H. G., Sun, C. H., Qiao, S. Z., Zou, J., Liu, G., Smith, S. C., Cheng, H. M., and Lu, G. Q. (2008). Anatase TiO_2 Single Crystals with a Large Percentage of Reactive Facets. *Nature*, 453, 638–641.

Yang, Y., Wen, J., Wei, J., Xiong, R., Shi, J., and Pan, C. (2013). Polypyrrole-Decorated Ag-TiO_2 Nanofibers Exhibiting Enhanced Photocatalytic Activity Under Visible-Light Illumination. *ACS Applied Materials & Interfaces*, 5, 6201–6207.

Zhang, Y., Tang, Z.-R., Fu, X., and Xu, Y.-J. (2010). TiO_2−Graphene Nanocomposites for Gas-Phase Photocatalytic Degradation of Volatile Aromatic Pollutant: Is TiO_2−Graphene Truly Different From Other TiO_2−Carbon Composite Materials? *ACS Nano*, 4, 7303–7314.

Zhang, Z., Zhang, L., Hedhili, M. N., Zhang, H., and Wang, P. (2013). Plasmonic Gold Nanocrystals Coupled with Photonic Crystal Seamlessly on TiO_2 Nanotube Photoelectrodes for Efficient Visible Light Photoelectrochemical Water Splitting. *Nano Letters*, 13, 14–20.

Zhu, Y., Murali, S., Stoller, M. D., Ganesh, K. J., Cai, W., Ferreira, P. J., Pirkle, A., Wallace, R. M., Cychosz, K. A., and Thommes, M., et al. (2011). Carbon-Based Supercapacitors Produced by Activation of Graphene. *Science*, 332, 1537–1541.

In: Fundamentals of Photocatalysis
Editor: Orva Auger
ISBN: 978-1-68507-374-9

Chapter 6

VISIBLE LIGHT-MEDIATED DDQ PHOTOREDOX-CATALYZED C-N BOND FORMATION REACTIONS: A REVIEW

Palani Natarajan**, PhD
Department of Chemistry and Centre for Advanced Studies in Chemistry, Panjab University, Chandigarh, India

ABSTRACT

In recent years, photoredox catalysis employing 2,3-dichloro-5,6-dicyano-1,4-benzoquinone (DDQ) has come to the limelight in organic chemistry as an effective strategy for the activation of small molecules. In a general sense, these approaches rely on the capacity of dyes to transform visible light into chemical energy by engaging in single-electron transfer processes with organic substrates. This chapter provides an overview of recent achievements in C-N bond formation reactions trigger by visible light-induced DDQ-photoredox catalysis, which

---

* Corresponding Author's E-Mail: pnataraj@pu.ac.in.

mainly discusses proposed reactions mechanisms as well as substrate scope and limitations.

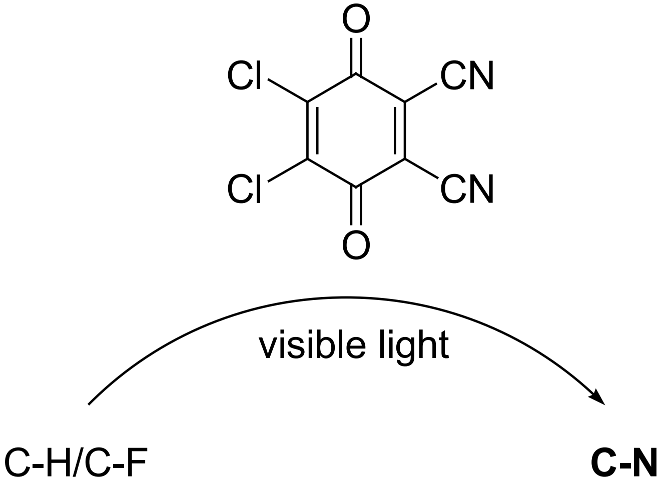

Keywords: DDQ, C-N bond formation, visible-light, C-H amination, photoredox catalysis

INTRODUCTION

The visible-light-mediated photoredox catalysis [1] has developed into a widely used method in synthetic organic chemistry for a series of new C-C and C-X (N, O, F, P, S, Cl, or Br) bond forming reactions over the previous decade [1]. For the most part, Ru- and Ir-based coordination complexes have been utilized as catalysts [2]. Parallel to the transition-metal complexes, efforts have been made to create metal-free visible-light photoredox catalysis using organic dyes include cyanoarenes, xanthenes, and acridiniums for synthetic transformations [3]. Comprehensive reviews on several photoredox catalysis are available [4-5], but to the best of our knowledge there is no review focusing on C-N bond formation initiated by visible-light-excited DDQ.

2,3-Dichloro-5,6-dicyano-1,4-benzoquinone (DDQ, Scheme 1) is commercially available, easy to handle, possesses good solvent solubility, often generates the corresponding reduced compound such as 2,3-dichloro-5,6-dicyano-1,4-hydroquinone ($DDQH_2$) as a byproduct and it can be readily recovered from $DDQH_2$ by treating with suitable oxidants [6]. The oxidation potential of ground state DDQ is 0.51 V vs. SCE and the compound is widely used in organic synthesis. Nevertheless, the one-electron oxidizing capacity of DDQ improves significantly by visible-light excitation from 0.51 V vs. SCE to 3.18 V vs. SCE [7] by triplet-excitation (^{3}DDQ*) or 3.8 V vs. SCE [8] by singlet-excitation (^{1}DDQ*). The exited-state DDQ has been utilized for the generation of a series of new C-N bond for synthesis of organic compounds and natural products.

DDQ-INITIATED C-N BOND FORMATION UNDER VISIBLE-LIGHT IRRADIATION

In 2017, Song and coworkers [9] reported a DDQ-photocatalyzed methodology for the direct C_2-H amination of thiophene (10) by azoles (11) under visible-light irradiation (Scheme 2). This protocol has been found applicable to a series of thiophenes containing either an electron-donating group (such as alkyl, trimethylsilyl or dioxolan) or an electron-withdrawing group (including chloride or bromide), and selectively transformed into their corresponding amination products (12) in good yield.

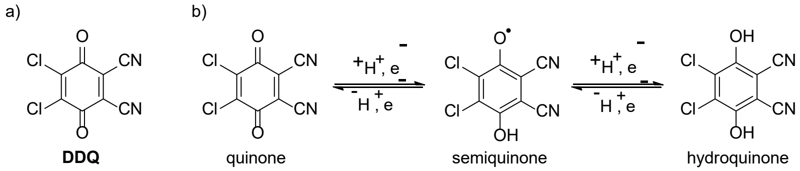

Scheme 1. The chemical structure of DDQ (a) and its three readily accessible oxidation states (b).

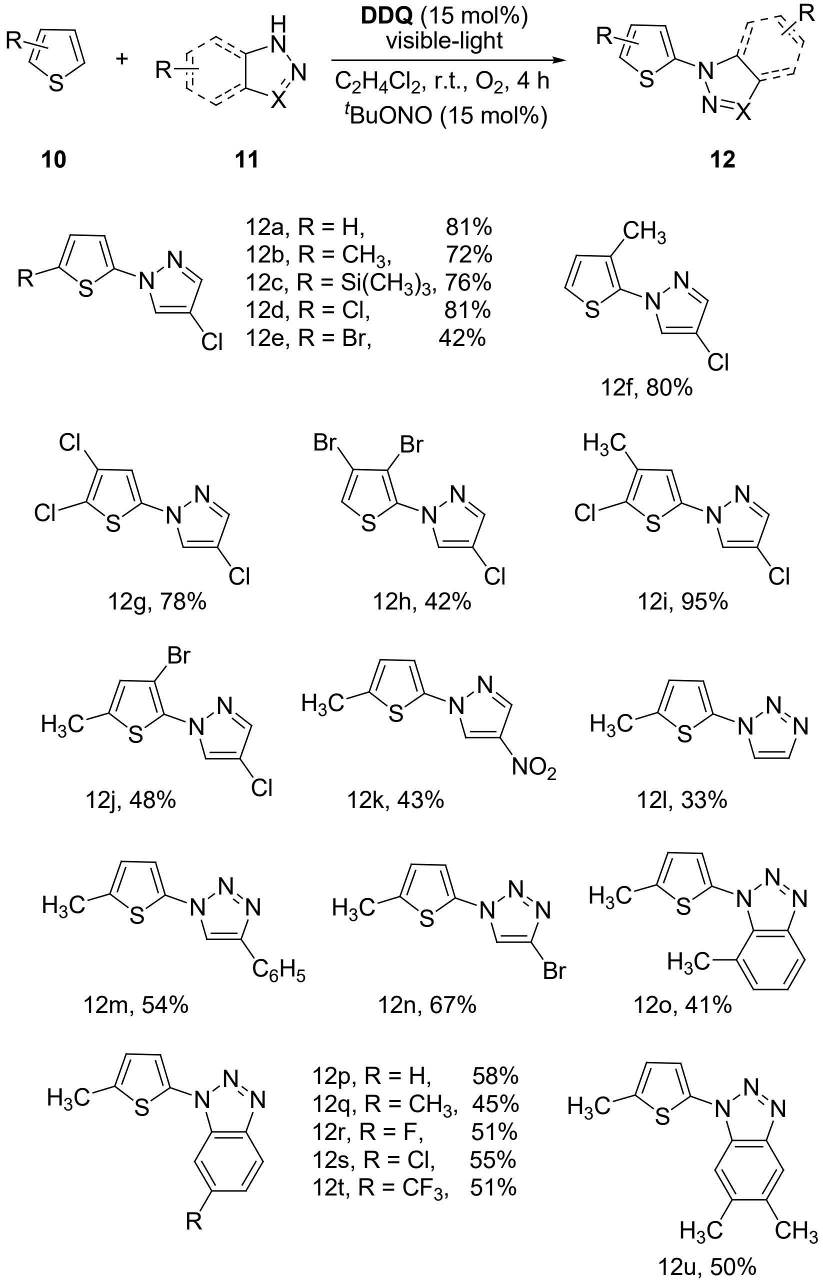

Scheme 2. The substrate scope for DDQ-photocatalyzed direct C_2-H amination of thiophene under visible-light irradiation.

Moreover, various nitrogen sources like pyrazole, triazole, benzotriazole and their derivatives have shown to be tolerated and afforded the expected product in moderate to good yields (Scheme 2). The authors found no desired product formed without light or DDQ.

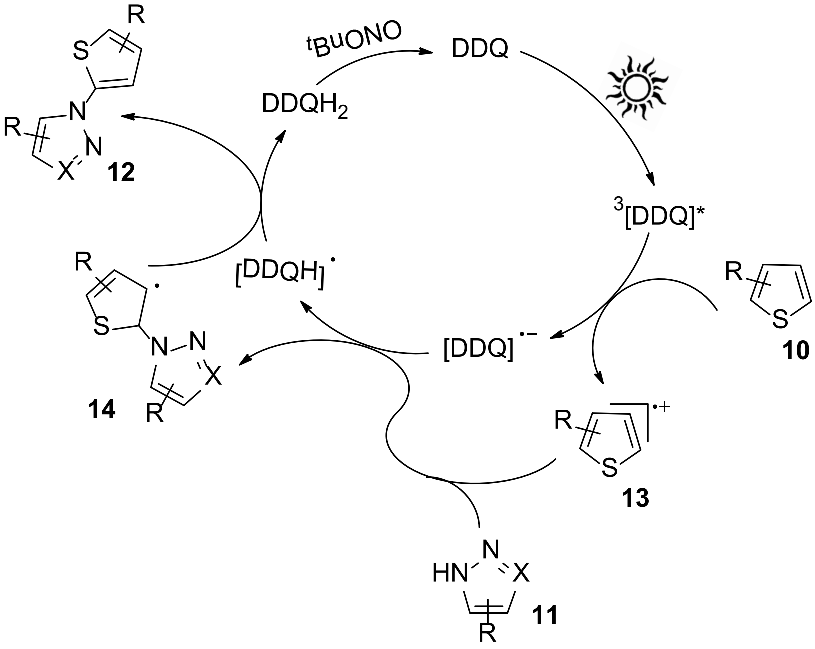

Scheme 3. A plausible mechanism for the DDQ-photocatalyzed direct C_2-H amination of thiophene under visible-light irradiation.

However, they detected only a small quantity of product in the absence of *tert*-butyl nitrite as the photocatalyst is not recycled.

The mechanism for DDQ-photocatalyzed direct C_2-H amination of thiophene by an azole under visible-light irradiation is depicted in Scheme 3 [9]. Upon irradiation by visible-light, DDQ has been excited into its triplet state (i.e., ^{3}DDQ*). The ^{3}DDQ*-assisted one-electron oxidation of thiophenes (10) afforded the corresponding radical cation intermediate (13). A reaction between 13 and a nucleophilic amine gave a new intermediate (14), which afforded the desired product (12) after the loss of an electron and a proton (Scheme 3). During these processes, DDQ is reduced to DDQH$_2$ and was oxidized by the reaction with *tert*-butyl nitrite and molecular oxygen via intermediate NO$_2$ to generate DDQ [9].

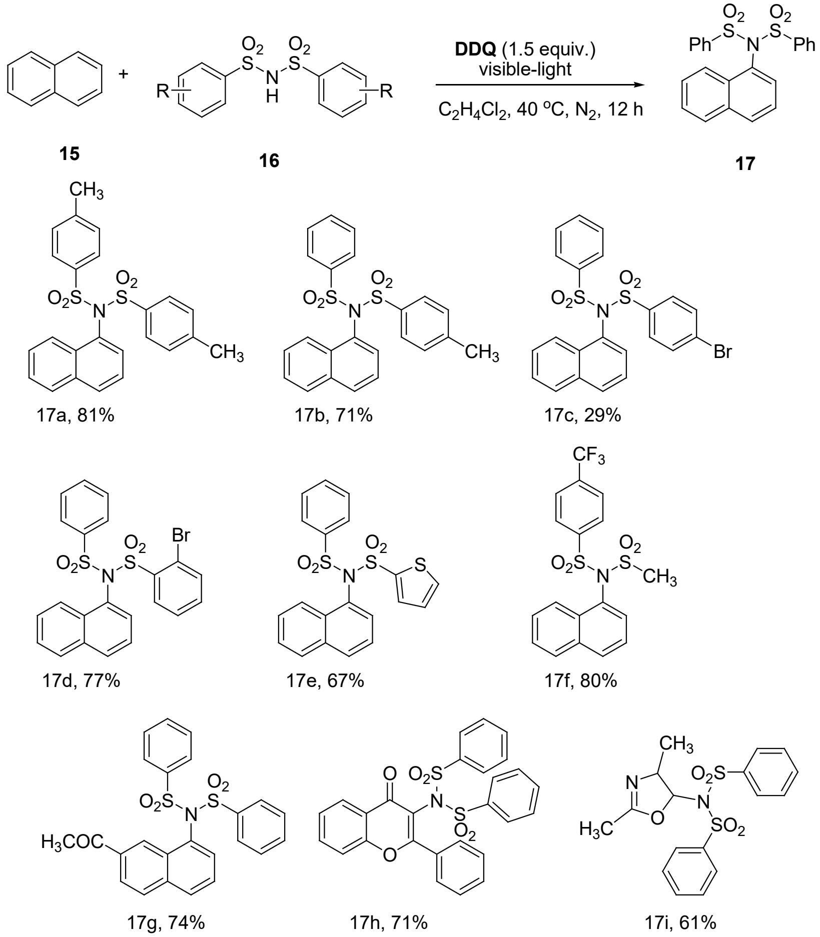

Scheme 4. The substrate scope for DDQ-assisted C-H amination of naphthalenes by sulfonimides under visible-light irradiation.

In 2017, Sakakibara and coworkers [10] reported a DDQ-assisted method for the direct C-H amination of naphthalenes (15) by sulfonimides (16) under visible-light irradiation (Scheme 4).

DDQ has been found essential for this transformation to proceed, because other quinone-based oxidants, such as *p*-benzoquinone, duroquinone, 1,4-naphthoquinone, anthraquinone, *p*-chloranil, *o*-chloranil, and 2,5-dichlorobenzoquinone were ineffective for the reaction. Likewise, control experiments without either a light source or DDQ did not give any conversion to the product. For the substrate scope, naphthalene (15), 2-acetylnaphthalene, 2,4-dimethyloxazole and flavone were effectively imidated in moderate to good yields (Scheme 4).

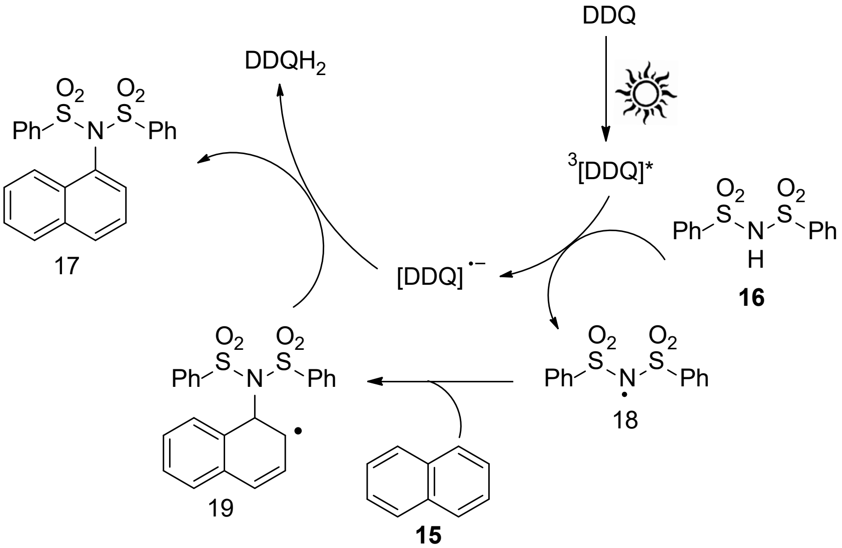

Scheme 5. A plausible mechanism for DDQ-assisted direct C-H amination of naphthalenes by sulfonimides under visible-light irradiation.

In addition, diarylsulfonimides with alkyl, bromo, and trifluoromethyl group are tolerated under the reaction conditions and afforded the corresponding coupling products in significant yield (Scheme 4).

Scheme 5 shows a possible mechanism for DDQ-assisted direct C-H amination of naphthalenes (15) by sulfonimides (16) under visible-light irradiation [10]. Upon irradiation by visible-light, DDQ is excited into its triplet state (i.e., ^{3}DDQ*). The ^{3}DDQ*-assisted one-electron oxidation of diarylsulfonimides (16) afforded the corresponding imidyl radical intermediate (18). A reaction between the imidyl radical (18) and naphthalene gave a new radical intermediate (19), which afforded the desired product after loss of an electron and a proton (Scheme 5). During these processes, DDQ was to $DDQH_2$.

In 2017, we described a protocol for DDQ-photocatalyzed direct C-H amination of both electron-deficient arenes (Scheme 6) and electron-rich arenes (Scheme 7) with a series of amines under visible-light irradiation at ambient conditions [11]. The reaction outcome can be well predicted for different substrates.

Electron neutral and electron-deficient arenes like benzene, chlorobenzene, dichlorobenzene, etc., do not form a charge-transfer complex with DDQ and react with all amine nucleophiles such as Boc-amine, amides, pyrazole, triazole, sulfonamide or urea that do not spontaneously react with DDQ in the ground-state. Nevertheless, electron-rich arenes such as naphthalene, phenanthrene, anisole, xylenes, 2-methylfuran, etc., which form a charge-transfer complex with DDQ react only with more nucleophilic amines, such as pyrazole and triazoles, but not with amides (Scheme 7).

Amines that are more nucleophilic than pyrazoles and triazoles (e.g., imidazole and indole) react spontaneously with DDQ in its ground-state. The different reactivity of electron-deficient and electron-rich arenes towards amines is explained by the different electrophilicity of the aromatic radical cation. Accordingly, the radical cation generated from benzene or chlorobenzene reacted with all amine nucleophiles, while the radical cation of anisole was less reactive and afforded products only with better nucleophiles [11].

Scheme 8 shows two possible mechanistic pathways for DDQ-photocatalyzed direct C-H amination of arenes under visible-light irradiation [11]. The first mechanistic proposal (mechanism I in Scheme 8) is based on $^3DDQ^*$-assisted one-electron oxidation of arenes. Upon irradiation by visible-light, DDQ is excited into its triplet state (i.e., $^3DDQ^*$). Afterwards, $^3DDQ^*$ converts all arenes (20) to their corresponding radical cations (26). A nucleophilic reaction between the arene radical cation (26) and amines (21) followed by oxidation of the resulting species (27) yielded the desired product (22, Scheme 8).

The second mechanistic proposal (mechanism II in Scheme 8) is based on the formation of a charge-transfer complex between amines and DDQ in the ground state.

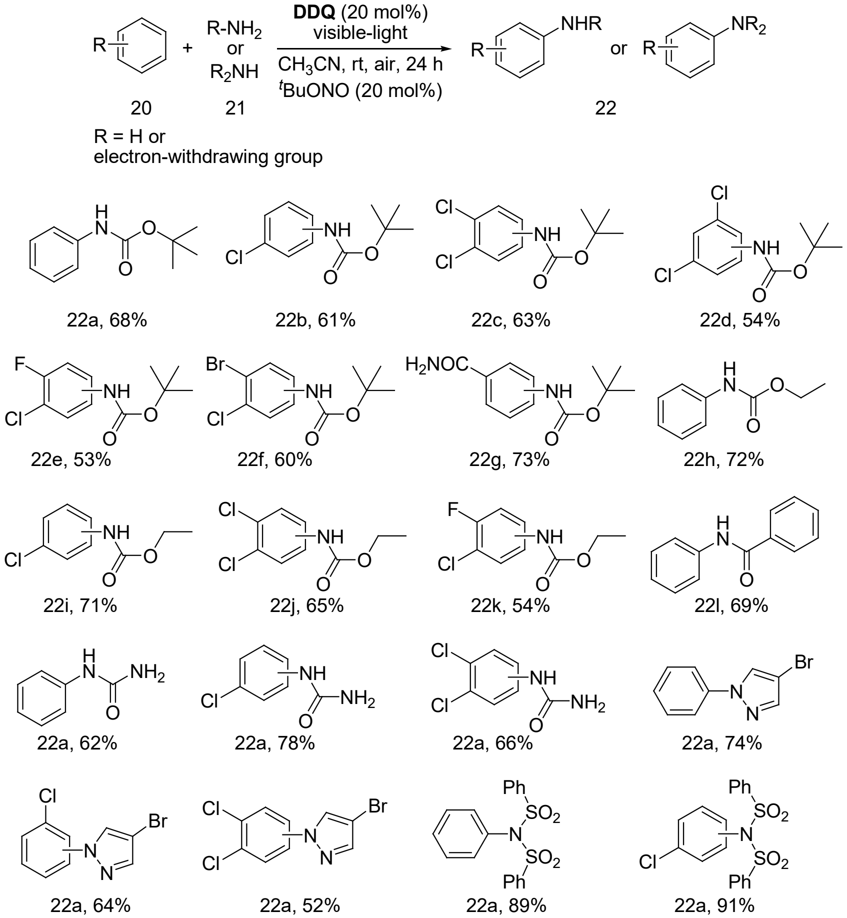

Scheme 6. The substrates scopes for DDQ-photocatalyzed direct C-H amination of electron-deficient arenes under visible-light irradiation.

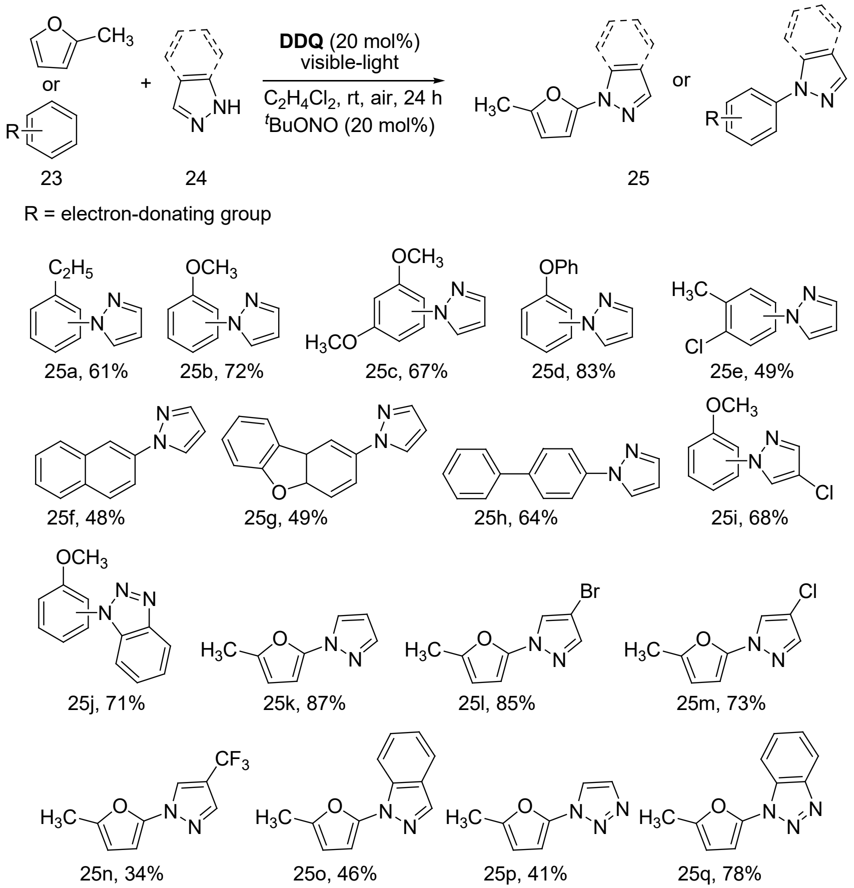

Scheme 7. The substrates scopes for DDQ-photocatalyzed direct C-H amination of electron-rich arenes under visible-light irradiation.

Excitation by visible-light, [DDQ-amine] charge-transfer complex (28) initiated hydrogen atom transfer occurs generating an amine radical (30) and a [DDQH] radical.

The amine radical reacts with an arene (20) to radical intermediate (27), which affords the desired product after loss of an electron and a proton (Scheme 8). In both mechanistic proposals, DDQ is reduced to $DDQH_2$ and reoxidized by reaction with *tert*-butyl nitrite and molecular oxygen. Experimental observations favor mechanism I as the DDQ charge-transfer band spans from 450nm to almost 600nm, but green light excitation afforded significantly less product and electron-deficient arenes with very high oxidation potentials (e.g., ethyl benzoate, benzonitrile) were beyond the substrate scope [11]. However, only a detailed time resolved spectroscopic study is necessary to fully elucidate the mechanism of the reaction.

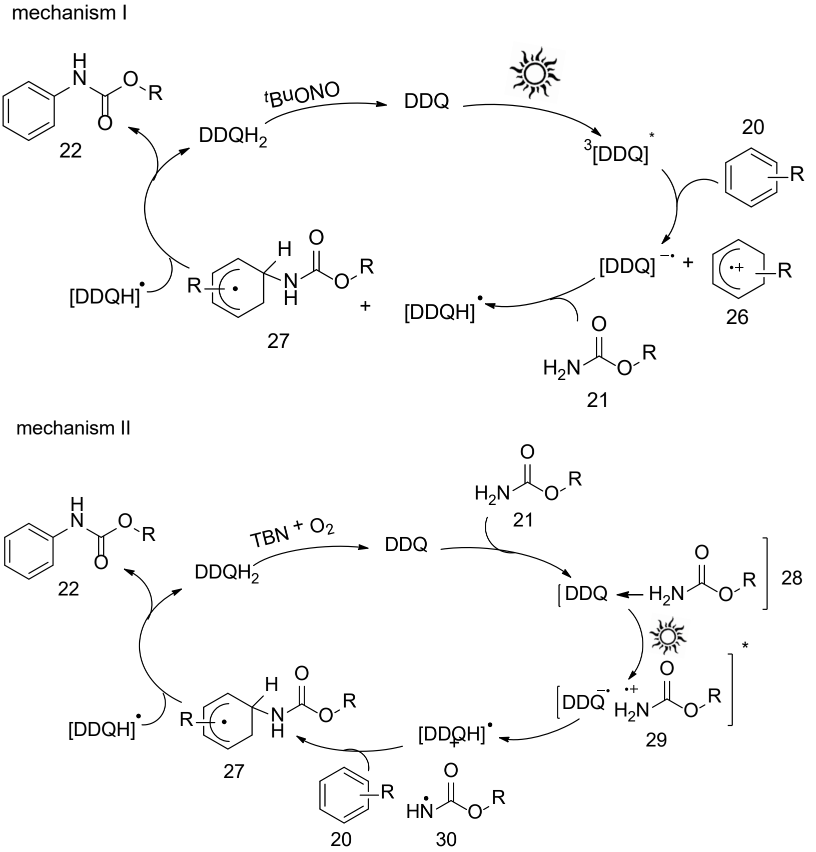

Scheme 8. A plausible mechanism for the DDQ-photocatalyzed direct C-H amination of arenes under visible-light irradiation.

In 2018, Zhang and coworkers [12] reported a DDQ-photocatalyzed method for the direct C-H amination of enol ethers (31) under visible-light irradiation (Scheme 9).

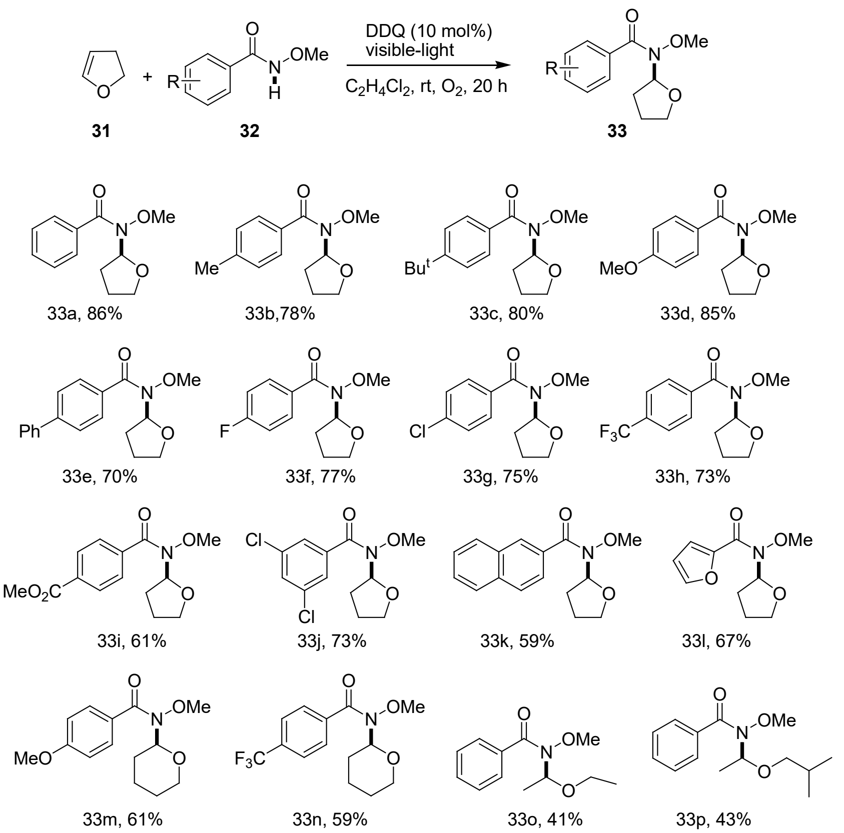

Scheme 9. The substrates scope for DDQ-photocatalyzed direct C-H amination of enol ethers under visible-light irradiation.

Different vinyl ethers such as ethyl vinyl ether, propyl vinyl ether, ethyl propenyl ether, n-butyl vinyl ether or *iso*-butyl vinyl ether, as well as cyclic vinyl ethers like 3,4-dihydro-2H-pyran are selectively transformed into their corresponding amination products in moderate to good yields. N-methoxyamides as amine coupling partners with electron-donating and weakly electron-withdrawing substituents (methyl, ethyl, *tert*-butyl, methoxy, ethoxy, phenyl, fluoro, chloro, and bromo) at the *para*-positions of the phenyl rings underwent the transformation smoothly and afforded the desired products in good yield (Scheme 9).

In contrast, N-methoxyamides with a strong electron-withdrawing group like CF_3O, CF_3, CN and $COOCH_3$ at the *para*-position of the aromatic ring gave only a moderate yield of the desired product.

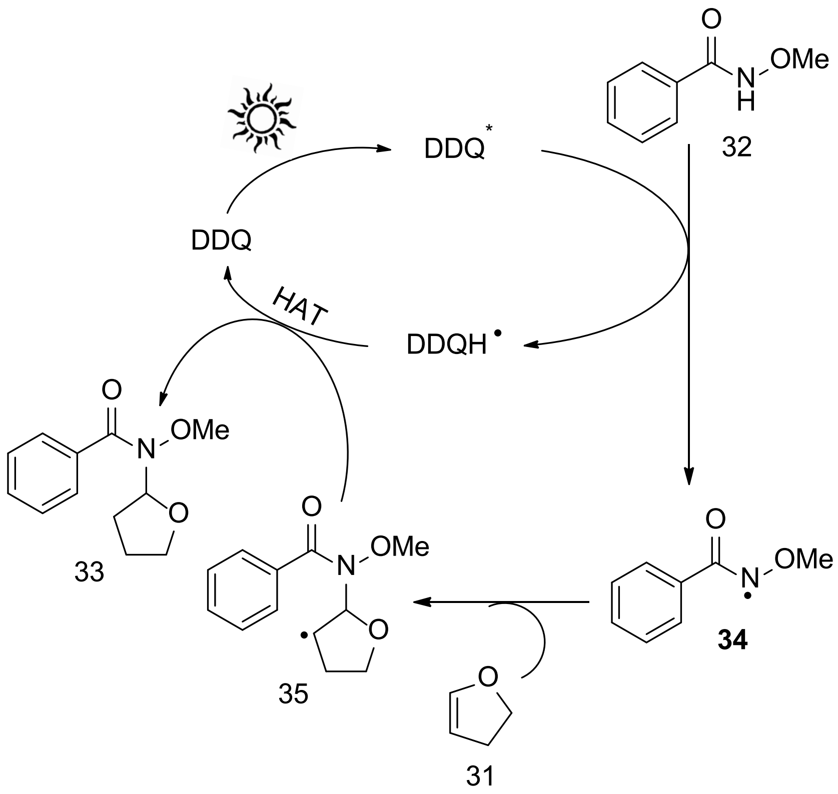

Scheme 10. A plausible mechanism for the DDQ-photocatalyzed direct C-H amination of enol ethers under visible-light irradiation.

In control experiments, the authors found no expected product without light or DDQ. DDQ is essential for the reaction; typical other photocatalysts including $[Ru(phen)_3]^{2+}$, $[Ru(bpy)_3]^{2+}$, eosin Y and rose bengal failed to catalyze the reaction under the irradiation of visible-light [12].

Scheme 10 shows a plausible mechanism for the direct C-H amination of enol ethers (31) by N-methoxyamides (32) under visible-light irradiation [12]. Upon irradiation by visible-light, DDQ is excited to its triplet state (i.e., ^{3}DDQ*). The ^{3}DDQ*-assisted oxidation of N-methoxybenzamide (32) through a single electron transfer process affords the N-centred radical intermediate 34 and a [DDQH]$^\bullet$ radical.

An addition reaction between 34 and the α-carbon of the olefinic bond in enol ethers (31) provides a new carbon-centred radical intermediate 35. Subsequently, 35 abstracts the hydrogen atom from the [DDQH]• radical and gave the desired product. By this processes, DDQ was regenerated (Scheme 10).

In 2019, Zhang and coworkers [13] reported a DDQ-assisted strategy for the direct C-H amination of ethers (36) by N-alkoxyamides (37) under visible-light irradiation (Scheme 11).

This protocol requires DDQ and visible-light for product formation. A variety of N-methoxyamides (37) bearing electron-donating groups (methyl, *tert*-butyl and methoxy) and electron-withdrawing groups (trifluoromethyl, fluoro, chloro and bromo) on the aryl ring smoothly reacted with ethers (tetrahydrofuran and tetrahydropyran) and afforded the desired products in good yield.

However, under the optimized reaction conditions, acyclic alkyl (thio)ethers, such as diethyl ether and tetrahydrothiophene gave not the desired products.

Thus, a series of N-methoxyamides were readily cross-coupled with tetrahydrofuran or tetrahydropyran using DDQ and visible-light (Scheme 11).

A possible mechanism for DDQ-assisted C-H amination of ethers under visible-light irradiation is shown in Scheme 12 [13]. Upon visible-light irradiation, DDQ is excited to its triplet state. The ^{3}DDQ* has been found capable to oxidize both N-methoxyamides (37) and ethers (36) via a single electron transfer process. Accordingly, ^{3}DDQ* reacted with N-methoxyamides and ethers and afforded the aminyl radical intermediates 39 and ether radical intermediates 40, respectively. Radical-radical combination is proposed to yield the reaction products (38, Scheme 12).

In 2020, Huang and coworkers [14] published an electrophotochemical approach for the C-F amination of fluoroarenes (41) by azoles (42) using DDQ as a catalyst under visible-light irradiation (Scheme 13).

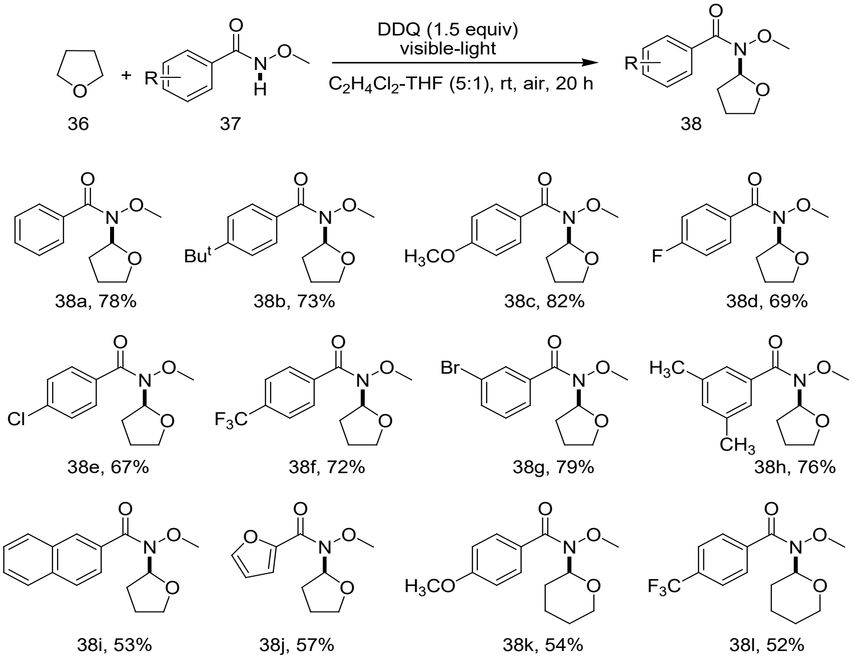

Scheme 11. The substrates scopes for DDQ-assisted direct C-H amination of ethers under visible-light irradiation.

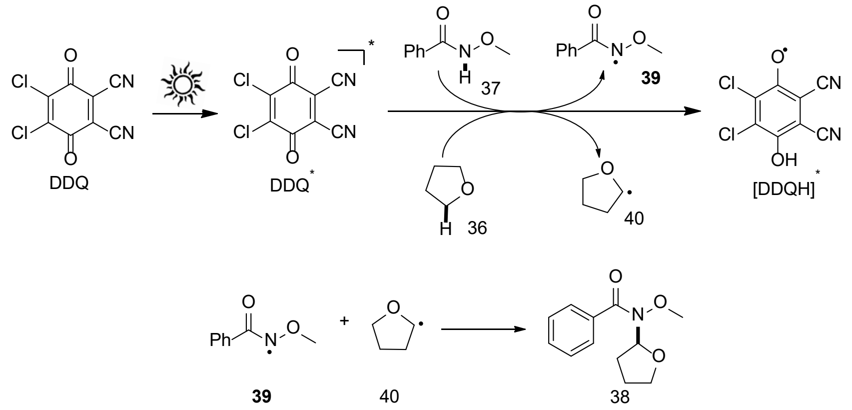

Scheme 12. A plausible mechanism for the DDQ-assisted direct C-H amination of enol ethers under visible-light irradiation.

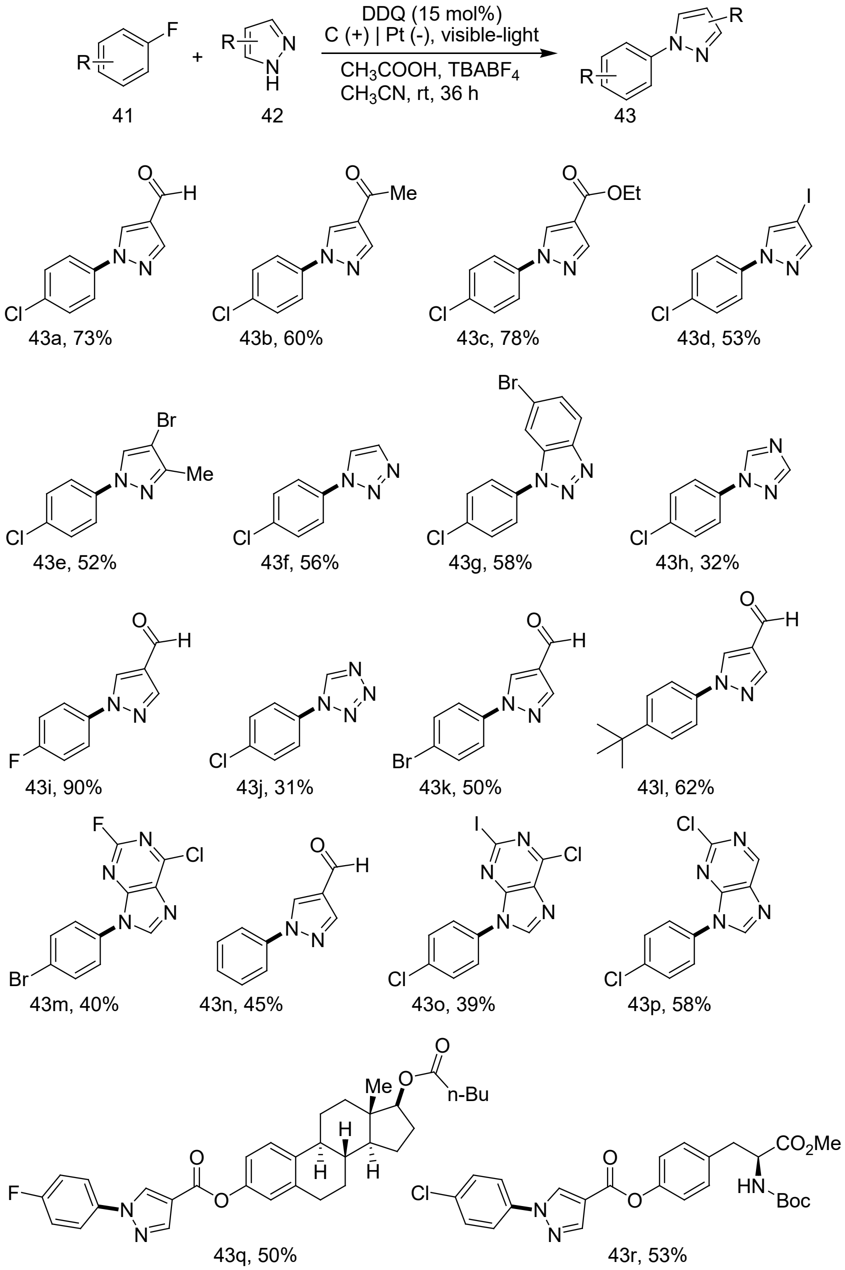

Scheme 13. The substrate scope for DDQ photoelectro-catalyzed direct C-F amination of fluoroarenes by azoles.

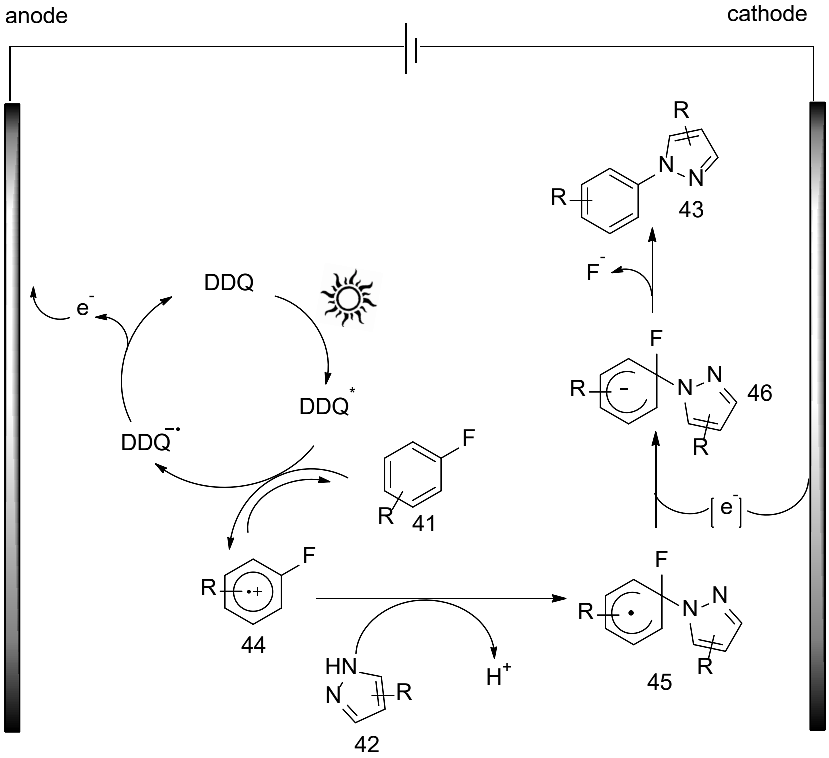

Scheme 14. A plausible mechanism for the DDQ-photocatalyzed direct C-F amination of fluoroarenes by azoles via electrophotochemical approach.

The protocol uses an excess of the fluoroarene substrates and a stoichiometric amount of the heteroarene nucleophiles as limiting reagent. A series of fluoroarenes with chloro, bromo and cyano substituents on the phenyl ring were selectively transformed into their corresponding amination products (43a-43r) in moderate to good yields. Likewise, azole coupling partners, pyrazole, triazole, imidazole, purine and their derivatives react smoothly and afford the desired products in moderate yield. The authors mention that ester moieties of products are labile under the strongly basic conditions of a classic SN_{Ar} reaction, but are tolerated (43q-43r) in this methodology [14]. Moreover, DDQ is recycled electrochemically (Scheme 13).

The mechanism for DDQ photoelectro-catalyzed direct C-F amination of fluoroarenes is depicted in Scheme 14 [14]. Upon irradiation by visible-light, DDQ is excited to its triplet state. The ^{3}DDQ*-assisted one-electron oxidation of the fluoroarene (41) affords the corresponding radical cation intermediate (44). A reaction between 44 and a nucleophilic azole (42) gives a new carbon-centered radical intermediate (45). The intermediate 45 is reduced electrochemically yielding anion 46 responsible for formation of product (43) after loss of the fluoride anion. DDQ, which was reduced to DDQ$^{\bullet-}$ was oxidized electrochemically to close the catalytic cycle (Scheme 14) [14].

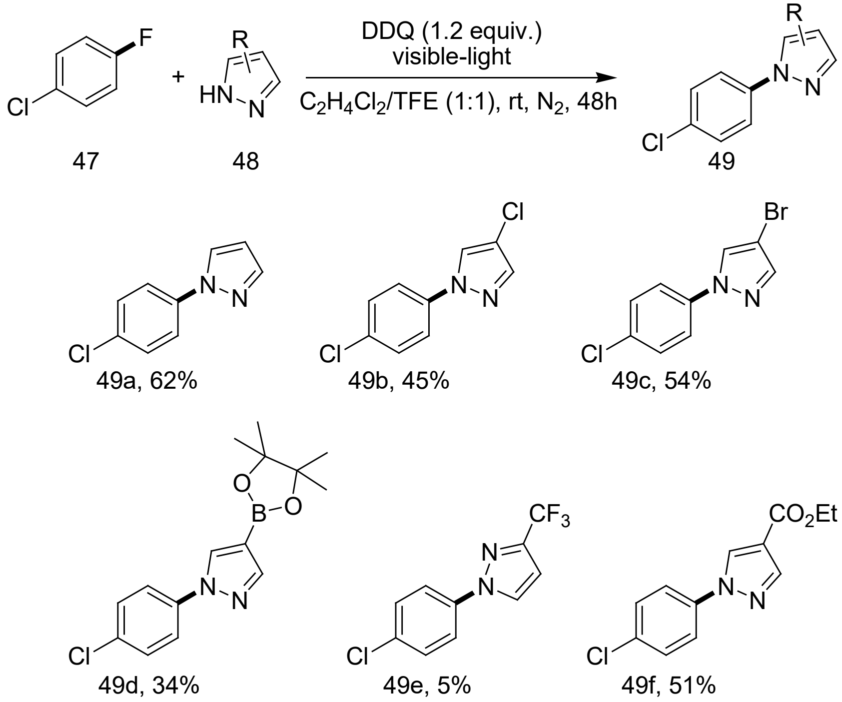

Scheme 15. The substrates scope for DDQ-assisted direct C-F amination of chlorofluoroarenes by pyrazoles under visible-light irradiation.

In 2020, Sheridan and coworkers [15] also reported a protocol used DDQ for the C-F amination of fluoroarenes (47) with pyrazoles (48) under visible-light irradiation (Scheme 15). In this method, authors used either trifluoroethanol (TFE) or 1:1 mixture of dichloroethane (DCE) and trifluoroethanol (TFE) as reaction medium due to its property of stabilization of the radical cation intermediate of substrate. Moreover, to avoid the direct reaction of pyrazole with DDQ, authors added azole slowly over the course of reaction. Using these conditions, a series of chlorofluoroarenes and a small set of functionalized pyrazoles reacted well and were selectively transformed into their corresponding amination products (49a-49f) in low yield [15]. A reaction mechanism was not proposed. However, it is likely that the ^{3}DDQ*-assisted one-electron oxidation of fluoroarene to the corresponding radical cation intermediate followed by nucleophilic pyrazole attack and rearrangement gave the reaction products.

CONCLUSION AND OUTLOOK

The C-N bond formation reactions examined in this articule illustrate that a skillful utilization of DDQ under visible-light may replace conventional and metal-assisted cross-dehydrogenative coupling reactions by a more sustainable and facile route. DDQ and $DDQH_2$ can be stored for longer periods under ambient conditions, are commercially available and can be handled without any special precautions. Despite some progress in the field, the uses of aliphatic compounds as starting substrates as well as stereo-selective functionalization are future challenges in DDQ catalysis.

REFERENCES

[1] Nicewicz, D. A., MacMillan, D. W. C. *Science*, 2008, 322, 77-80.

[2] Juris, A., Balzani, V., Barigelletti, F., Campagna, S., Belser, P., von Zelewsky, A. *Coord. Chem. Rev.*, 1988, 84, 85-277.

[3] Narayanam, J. M. R., Stephenson, C. R. J. *Chem. Soc. Rev.*, 2011, 40,102- 113.

[4] For selected reviews on organic photoredox catalysis, see: a) Fagnoni, M., Dondi, D., Ravelli, D., Albini, A. *Chem. Rev.*, 2007, 107, 2725-2756; b) Ravelli, D., Fagnoni, M. *Chem. Cat. Chem.*, 2012, 4, 169-171; c) Marin, M. L., Santos-Juanes, L., Arques, A., Amat, A. M., Miranda, M. A. *Chem. Rev.*, 2012, 112, 1710-1750; d) Ravelli, D., Fagnoni, M., Albini, A. *Chem. Soc. Rev.*, 2013, 42, 97-113; e) Nicewicz, D. A., Nguyen, T. M. *ACS Catal.,* 2014, 4, 355-360; f) Qin, Y., Zhu, L., Luo, S. *Chem. Rev.*, 2017, 117, 9433-9520.

[5] For selected reviews on metal-based photoredox catalysis, see: a) Koike, T., Akita,M. *Inorg. Chem. Front.*, 2014,1, 562-576; b) Pirtsch, M., Paria, S., Matsuno, T., Isobe, H., Reiser, O. *Chem. – Eur. J.,*2012, 18, 7336-7340; c) Fukuzumi, S., Lee, Y.-M., Nam, W. *Chem. Sus. Chem.*, 2019, 12, 3931-3939.

[6] Walker, D., Hiebert, J. D. *Chem. Rev.,* 1967, 67, 153-195.

[7] Fukuzumi, S., Ohkubo, K. *Chem. Sci.*,2013, 4, 561-574.

[8] Ohkubo, K., Hirose, K., Fukuzumi, S. *Chem.–Eur. J.*, 2015, 21, 2855-2861.

[9] Song, C., Yi, H., Dou, B., Li, Y., Singha, A. K., Lei, A. *Chem. Commun.,* 2017, 53, 3689.

[10] Sakakibara, Y., Ito, E., Kawakami, T., Yamada, S., Murakami, K., Itami, K. *Chem. Lett.,* 2017, 46, 1014.

[11] Das, S., Natarajan, P., König, B. *Chem. Eur. J.,* 2017, 23, 18161.

[12] Zhang, Y., Chen, W., Wang, L., Li, P. *Org. Chem. Front.*, 2018, 5, 3562.

[13] Zhang, Y., Wang, L., Wang, Z., Chen, W. *Tetrahedron,* 2019, 75, 130516.

[14] Huang, H., Lambert, T. H. *Angew. Chem. Int. Ed.,* 2020, 59, 658.

[15] Sheridan, T., Yayla, H. G., Lian, Y., Genovino, J., Monck, N., Burton, J. W. *Eur. J. Org. Chem.*, 2020, 2766.

INDEX

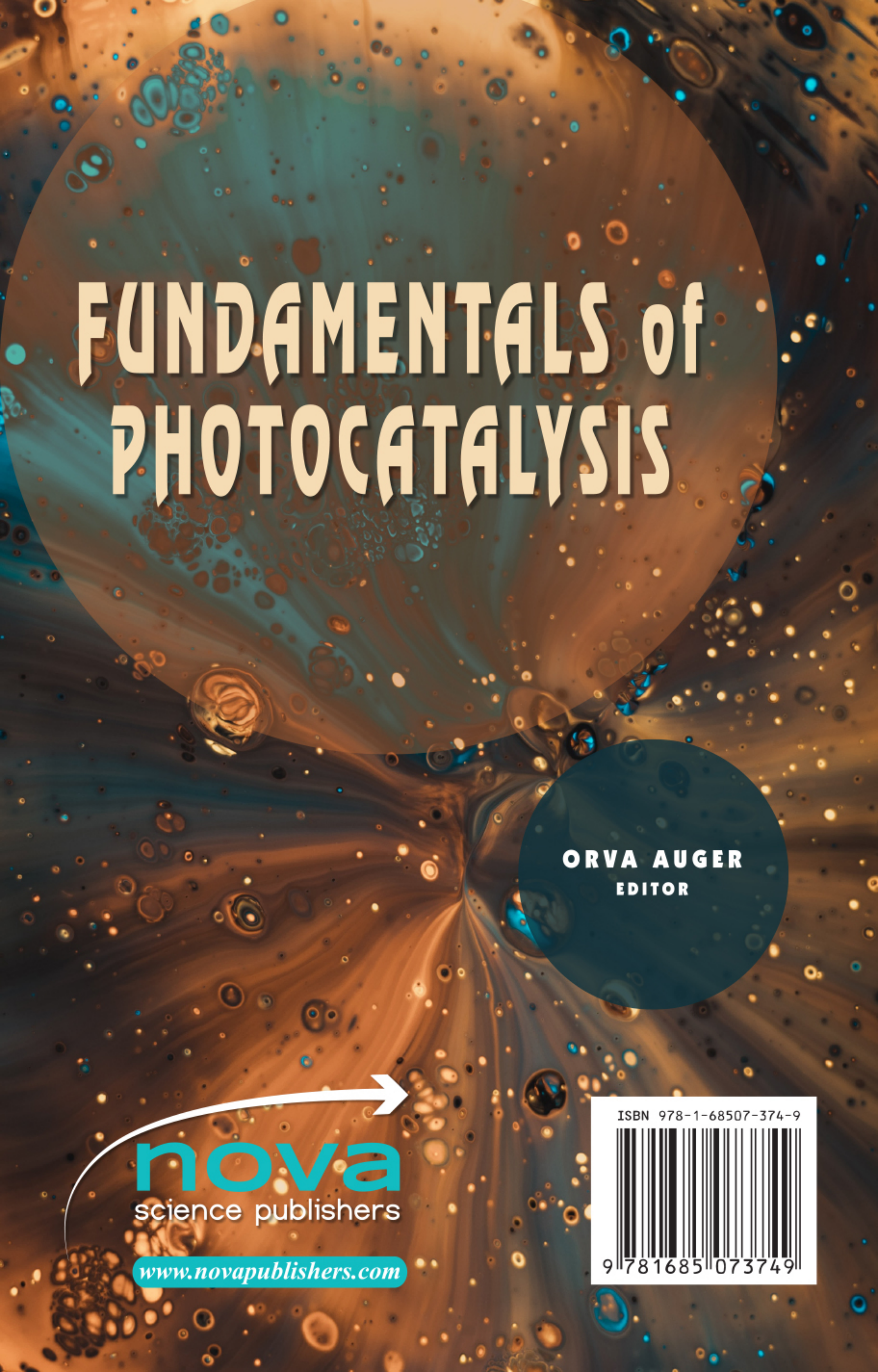

FUNDAMENTALS of PHOTOCATALYSIS

ORVA AUGER
EDITOR

nova
science publishers
www.novapublishers.com

ISBN 978-1-68507-374-9
9 781685 073749